Adaptive methods for processing and interpretation of an underground blowout

by

Hung Nho Dinh

A thesis submitted in partial fulfillment of the requirements for the degree of

Doctor of Philosophy

in

Geophysics

Department of Physics
University of Alberta

Abstract

In reservoir management, seismic surveillance is crucial to maximize the value of the field. It is not only useful in revealing the current reservoir situation, but also in managing future risks. In a typical seismic monitoring project, repeated data acquisition and processing are required for later quantitative analyses. With legacy data, time-lapse (4D) examination is more complex because the data acquisition is designed without the 4D application in mind.

This thesis focuses on methods for processing and interpretation of a 1989 underground blowout development in the North Sea area where gas has charged into two main shallow sand layers. Efforts to study gas migration extent and changes in pressure and saturation in the two recipients were made. However, due to legacy data repeatability problems (differences in seismic acquisition and processing), a long-term blowout development investigation faced limitations in resolving 4D signals and addressing in-situ condition changes. The objectives of this study are to find a sensible strategy to process the time-lapse data, and to analyze the blowout development using 4D attenuation attribute.

To increase legacy data repeatability, different seismic processing techniques are tested and compared. The following objectives are met: compensate for the acquisition feathering effects by regularization and rebinning; remove multiples by combining the predictive deconvolution and the surface related multiple elimination techniques; and correct for residual signal differences by matching the waveform and time arrivals. I also aim to preserve the seismic amplitude spectrum to evaluate attenuation changes better. The proposed strategy has created much higher quality 4D images and interpretable attributes.

I then establish a complete inversion workflow to solve for changes in pore

pressure and gas saturation. I find that a combination of the random patchy saturation model and the pore space stiffness model is suitable to forward model 4D attributes. I also show that a grid-search inversion scheme is successful to obtain reservoir condition changes from real time-lapse measurements. The grid-search method is also an effective approach for quality control and visual uncertainty analysis.

My results provide new details about the sand conditions at different times as well as the effects of different geological structures on light gas movement. Based on the inverted pressure, I find out that gas was spreading slowly in both sand layers and that the blowout source may have stopped early. These findings are valuable to understand the blowout development and are helpful for further reservoir management.

Preface

This dissertation is submitted for the degree of Doctor of Philosophy in Geophysics at the University of Alberta. The research described herein is original, and neither this nor any substantially similar dissertation was or is being submitted for any other degree or other qualification at any other university.

A version of chapter 3 has been published as Dinh et al. (2017b). I was responsible for code development, data analysis, figure preparation and manuscript writing.

A manuscript of chapter 4 has been submitted to Geophysics as Dinh and Van der Baan, 2018, A grid-search approach for 4D pressure-saturation discrimination and is undergoing a minor revision request. A version of the Appendix has been presented at the SEG annual international meeting in 2016 as Dinh et al. (2016). I am responsible for code development, data analysis, figure preparation, and manuscript writing.

A version of chapter 5 is presented at the SEG annual international meeting in 2017 as Dinh et al. (2017a). I am responsible for code development, data analysis, figure preparation, and manuscript writing.

To my beloved father, Dinh Nho Hoang

Acknowledgements

This thesis is the most challenging and sophisticated achievement I have completed so far, thanks to the encouragement of many people.

First of all, I would like to express my great appreciation to Dr. Mirko Van der Baan for his supervision through my research. Since I started in 2012, he saw something in me and has patiently guided me through this academic adventure. Within the last six years, he was the one who had inspired me with his experience and knowledge when I got stuck on technical writing or buried by silly ideas. It was not only what I have learned during the research, but also the valuable skills I have learned from him. He was also the person who has given me wholehearted support through many conferences and an internship from which I have gained valuable academic and industrial experience.

I would like to recognize Thomas D. Blanchard for his conversations on attenuation, the core object of my research. I would like to thank Martin Landrø, who was so kind for giving me a wonderful visit to NTNU to better understand the datasets. Not only that, his constructive criticism and feedback through my research have made this thesis much stronger. During the program, I also had a chance to work with Brian H. Russell, a brilliant guy, who was so enthusiastic about helping me develop the rock physics theory.

I also want to recognize the supervisory committee members — Dr. David Potter, Doug Schmitt (who was unfortunately absent from my defense) — and the examiners — Dr. Julia Leung, Bern Milkereit (who has travelled from the University of Toronto to attend my defense) and Jeffrey Kavanaugh — for their time reading and giving detailed constructive comments on this thesis. The questions and suggestions they proposed during my defense would definitely

refine this work more completely.

I would like to thank the Natural Sciences and Engineering Research Council of Canada (NSERC) for providing funding and the LOng-term SEismic Monitoring (LOSEM) project partners for providing the datasets to work on. I would also like to acknowledge MathWorks, CGG and Vietnam Petroleum Institute for giving me access to Matlab, Hampson-Russell and ProMAX to process these datasets.

When looking back to this journey, I would like to give great gratitude to Minh Q. Dam, Minh Q. Ta who have inspired me to nourish my fascination with geophysics and Thai H. Ho who has also followed this campaign from the first days. Special thanks to Sarah Derr, Edward Marcum and Amna Feroz for listening and helping me get over the problems I had as an international student. Thanks to Amna Feroz and Yoones Vaezi (my two adorable office mates), Hung T. Nguyen, Toan H. To, Zhenhua Li and Himanshu Barthwal for being my friends when I was in Edmonton.

During my Ph.D., I was extremely lucky to have Si T. Le and An H. N. Nguyen for trusting, supporting, and standing by me at all good and bad times, even in my most lonely, darkest days. This thesis would not be completed without the two of them. Finally, I would like to thank my parents for their unconditional love. Their encouragement in following my passion has always been the biggest motivation for all success in my life.

Contents

List of Tables

List of Figures

List of Abbreviations

1D	One-dimensional
2D	Two-dimensional
3D	Three-dimensional
4D	Four-dimensional
AVO	Amplitude versus offset
mRKB	Meter below the rotary kelly bushing
NRMSE	Normalized root mean squared errors
PSS	Pore space stiffness
RPS	Random patchy saturation
SRME	Surface related multiple elimination
SWD	Shallow water demultiple
$\tau - p$	Tau-p domain

Chapter 1

Introduction

1.1 Background of time-lapse analysis

1.1.1 Definitions and Ideas behind time-lapse analysis

Time-lapse (or 4D) analysis is a recent technique that helps to observe and interpret changes of objects over time. In the energy industry, 4D is used to monitor hydrocarbon reservoirs during production or CO_2 storage in long-term sequestration projects (Jack, 1998; Johnston, 2013; Kasahara and Hasada, 2017). It helps us to see what is going on in the reservoir, for example, changes in fluid movement, pressure or temperature. This knowledge is especially important in reservoir management where production efficiency is the main goal. Understanding the changes within the reservoir is the key factor to optimize the production plan, prevent potential risks and maximize the profit (Barkved, 2012).

The idea behind 4D analysis is simple. It detects the changes in the target at several times, not much different from a kid's puzzle of spotting differences between two similar pictures (Figure 1.1). Technically, one may subtract an input picture from the other to highlight their differences. The reason why it works is straightforward: If there are no changes in the scene, each object reflects the identical light amount to the camera sensor where the converted signals are processed and producing the same photo pixel. During subtraction,

these identical pixels are differenced away. If an object moves or changes its properties (for example, changes color due to wearing off over time), its reflected light is different and the changes will show up after subtraction.

Figure 1.1: 4D example from children game: the difference between 2 pictures (right) are calculated by subtracting one from the other (left and middle).

This analogy can be applied to seismic surveillance for reservoir delivery. The production activity causes variations in fluid saturation, formation pressure and reservoir temperature which lead to changes in elastic properties of the surrounding rock, for example in density and P-wave velocity (Calvert, 2005; Johnston, 2013). These property changes are all reflected in the seismic response. As a result, when acquiring new seismic data in the same field, we obtain detectable differences in the seismic signals where the changes occur. On the other hand, where there is no production activity, all elastic parameters are unchanged and produce identical seismic signals that are canceled out during subtraction. An advantage about 4D images is that only the differences are preserved, while all other geological features are whitened out (Figure 1.2). This is useful when the interpreter just needs to investigate the production effects rather than looking for hydrocarbon indicators.

In a 4D project, various information is used to achieve the goal: finding changes in reservoir conditions. During production, the main conditions that we are changing are fluid saturation, pressure, and temperature (Jack, 1998; Johnston, 2013). Their changes need to be inverted from time-lapse attributes which are estimated from different repeated seismic surveys. In order to do this task efficiently, we need data with good repeatability and suitable inversion techniques. In the next sections, I summarize the main requirements in terms

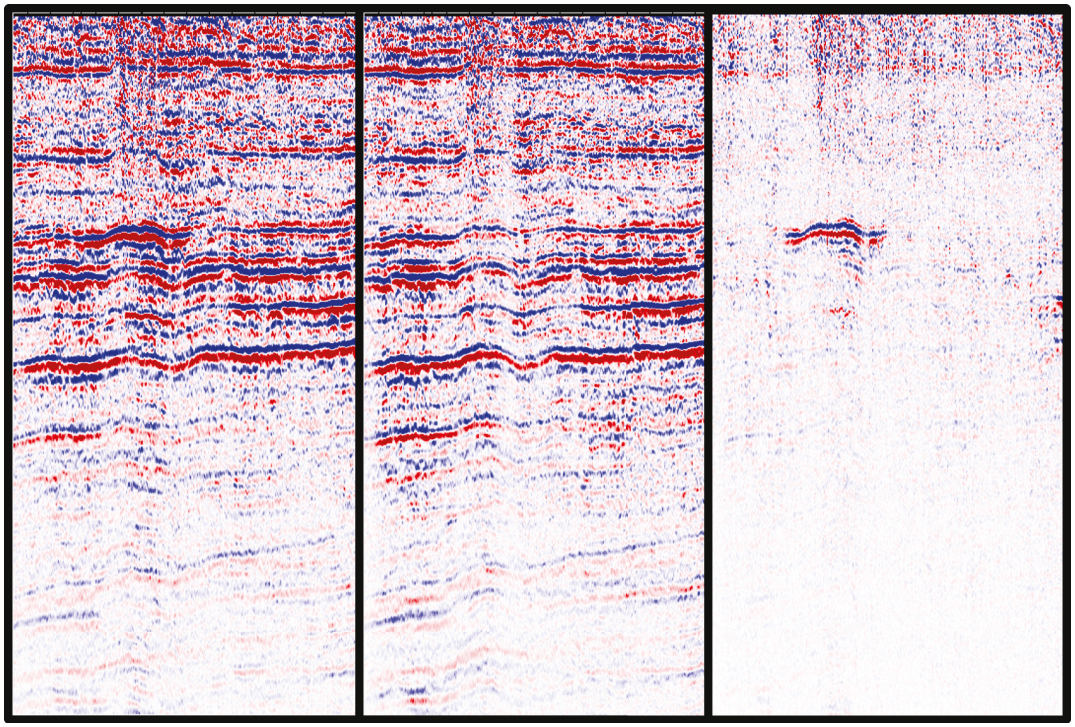

Figure 1.2: 4D example from real seismic data: when subtracting the monitor (middle) from the base (left) surveys, we obtain the changes between them (right). Edited from Dinh et al. (2017b).

of 4D data quality and common techniques from rock physics forward modeling to attribute inversion.

1.1.2 4D repeatability

In order to obtain time-lapse signals which show only the changes induced by production activities, all non-production areas should ideally display the same seismic responses. In real seismic acquisition, this requirement however is not always met because of the environment or the equipment (Barkved, 2012). Real seismic surveys are normally not identical but very similar. Repeatability indicates the similarity between seismic vintages. Between the base and monitor traces (*Base* and *Monitor*, respectively), their repeatability and predictability can be quantified by the root mean square (RMS) and correlation functions (Kragh and Christie, 2002):

$$NRMS = \frac{2RMS(Monitor - Base)}{RMS(Monitor) + RMS(Base)}, \tag{1.1}$$

where function $RMS(x) = \sqrt{\frac{\sum(x_i^2)}{N}}$ for the number of samples N in the time window x,

$$PRED = \frac{\sum Xcor^2(Base, Monitor)}{\sum(Acor(Base) \times Acor(Monitor))}, \tag{1.2}$$

where functions $Xcor$ and $Acor$ are the cross correlation and autocorrelation defined over a similar time window in Equation 1.1 and the sum is over time lags.

Regarding NRMS and PRED interpretation, Johnston (2013) has summarized their values as shown below in Table 1.1. NRMS is sensitive to time shifts, phase and amplitude distortion and noise. It is a measure of nonrepeatability. PRED has a similar sensitivity dependence except for time shifts. It can be useful in quality control of 4D processing, suggesting distortion and time shifts (when PRED is high) or noise removal (when PRED is low). In a best practice, both of these information should be calculated before and after processing to compare improvement (Dinh et al., 2017b).

Term	Value	Interpretation
NRMS	0	identical inputs
NRMS	2	anti-correlated inputs
NRMS	$\sqrt{2}$	inputs contain random noise
PRED	1	perfectly correlated/anti-correlated inputs
PRED	0	uncorrelated inputs

Table 1.1: Interpretation of NRMS and PRED.

There are two prerequisites for 4D repeatability: repeatability in acquisition and processing (Calvert, 2005; Johnston, 2013) which are both important. Repeated acquisition is essential to get similar seismic responses. Repeated processing is required to get similar seismic images. If seismic acquisition is too different, no advanced processing techniques can increase repeatability. On the other hand, even with highly repeated surveys, poor repeated processing will produce unusable images.

Acquisition

4D projects are split into three categories: legacy, re-shoot and 4D-designed (Lumley et al., 2003). Legacy is a product of matching several datasets acquired without the 4D application in mind. Re-shoot is when the monitor survey is designed to match the previous survey. 4D-designed is when the base survey is acquired with the objective to optimize a future 4D-monitoring program. In any of these projects, repeated acquisition is crucial as pointed out by Calvert (2005), Barkved (2012) and Johnston (2013). For acquisition repeatability, the survey geometry matching is most important to assure the recorded signals are similar outside the production area. Differences in source and receiver positions introduce different raypaths through the subsurface media and produce different images, even when representing the same reflection point.

Marine acquisitions easily reach NRMS of 0.6 if not designed for repeatability purposes (Barkved, 2012). Eiken et al. (2003) in their experiment have shown that shifting a marine seismic survey one bin laterally reduces NRMS to 0.4. A similar study done by Landrø (1999) has showed an NRMS of 0.08 for two VSP shots separated by less than 5 m. This is a high degree of repeatability for just two shots, especially when typical acceptable NRMS values are between 0.1–0.3 (Johnston, 2013).

As the earth environments vary continuously, marine geometry is essentially nonrepeatable. However different techniques and strategies have been introduced and applied to optimize it. Barkved (2012) has summarized the main acquisition factors that need to be addressed in 4D projects:

- orientation, shooting direction

- source and receiver: position, interval and configuration

- fold coverage, azimuth ranges and recording parameters (sample rate and filter settings)

In marine data, the most challenging issues are feathering, tidal currents and ocean waves which can be fixed by steerable streamers, survey planning or using wide swaths of streamers (Calvert, 2005). In a deep water area, brine temperature, density, and salinity gradient may also have significant effects on raypath repeatability (Johnston, 2013). On the other hand, onshore geometry repeatability is much easier to accomplish. However, it is prone to more noise

(ground roll and refractions) and lateral variations of near surface conditions.

Processing

In time-lapse analysis, geological structure resolution is not the main goal, but the changes in the reservoir. Calvert (2005) showed that two independent well-processed 3D images do not always guarantee decent 4D signals. Therefore, purposes of 4D processing are different from those of 3D processing. Nevertheless, 3D image controls are also important because 4D responses cannot be highlighted without good imaging (Johnston, 2013).

Time-lapse processing is expected to first maximize repeatability. It is also supposed to create similar (not necessarily the best repeated) images by removing non-repeated and repeated noises, correcting for velocity changes and matching the wavelet features. Last but not least, its goals are to preserve true relative amplitude and arrival times for quantitative time-lapse analysis (Johnston, 2013). 4D processing on repeated surveys should be conducted simultaneously with the same routines and parameters in order to create comparable outputs.

There are four main approaches for 4D processing (Lumley et al., 2003; Barkved, 2012), including: post-stack cross-equalization, pre-stack parallel processing, simultaneous pre-stack processing and fast-track processing. The first method uses cross-equalization processing to enhance repeatability of independent processed surveys, and is normally used for legacy data. Parallel processing is an approach to maximize repeatability by processing multiple seismic data using identical processing flows. Simultaneous processing merges the data vintages before applying processing operators. Fast-track processing is a technique that keeps the base survey and quickly applies the same processing sequences to the monitor survey with minimal cross-matching.

In marine data, most of the acquisition issues can be fixed, including geometry and feathering (by binning and regularization), source wavelet differences (by bandwidth and phase matching) and receiver motion and water-column statics (by directly compensating the differences of them between surveys which are logged in each survey). The non-repeated multiples sometimes pose very big repeatability problems, even more than the acquisition geometry because

the differences are accumulated at each bounce. A proven demultiple technique is surface related multiple elimination or SRME (Verschuur, 2006) combined with other processes (Johnston, 2013).

The overburden layer can also vary and reduce repeatability between vintages. In marine data, the changes in density, temperature and salinity can be corrected by measuring two-way water time changes (Calvert, 2005). With onshore data, high variation in near-surface velocity is the main challenge. Fortunately, most marine processing principles can be applied on land. In case of very complex lateral variations, surveys with wide-azimuth design or permanent buried receivers are required (Johnston, 2013).

1.1.3 4D Interpretation

When looking at seismic signals (including 4D signals), we are looking at their amplitude and frequency contents. The amplitude content is determined by rock velocity and density, and the frequency content is more governed by rock attenuation (Barton, 2007). Therefore, the goal of seeing reservoir development can be achieved by analyzing the variations of these rock properties, which are mainly caused by pressure and saturation changes (Jack, 1998; Calvert, 2005). In 4D attribute analysis, the most common attributes are time shifts, changes in amplitude, impedances, and attenuation.

According to Johnston (2013), a simple qualitative 4D interpretation involves examining time-lapse attributes to manage water or gas sweep, revise reserves estimations and to optimize well completions. Recent qualitative interpretation uses a combined template of Vp/Vs ratio and impedance to find the general trends of saturation and pressure variations (Andersen et al., 2009). On the other hand, the more preferred quantitative 4D interpretation finds measurable changes of saturation and pressure. It requires a rock physics model to link these changes with the observed time-lapse attributes. The model can be obtained from the literature or a statistical field calibration or a combination of the two (Johnston, 2013). Practically, a typical workflow for a quantitative 4D inversion (i.e., pressure vs. saturation discrimination) consists of 3 main stages:

- Step 1: The rock physics template to formulate reservoir properties from rock properties

- Step 2: Proper time-lapse seismic attributes, which can be calculated by the rock physics model in step 1, to feed the inversion problem

- Step 3: A method to solve the inverse problem with the time-lapse attribute input setup in step 2

Rock physics model

The rock physics model indicates how changes in pressure and saturation lead to changes in seismic responses. This knowledge is needed to model time-lapse seismic attributes and to convert them back to the changes in reservoir conditions.

Information about fluid saturation is clearly important for controlling well rates and well planning. However, its effects on seismic response can take years to observe in real oil and gas fields. Pressure changes, which travel through a field more quickly than fluids do (Calvert, 2005), are also very important. Unfortunately, pressure effects on seismic are less understood than saturation effects. The reason is due to the inability of lab conditions to mimic the effects of millions of years of burial.

Most of the seismic attributes are related to the wave propagation velocities, which are normally calculated by (Mavko et al., 2009):

$$\begin{aligned} Vp &= \sqrt{\frac{K + 4\mu/3}{\rho}}, \\ Vs &= \sqrt{\frac{\mu}{\rho}}, \end{aligned} \tag{1.3}$$

where K and μ are bulk and shear moduli, and ρ is the density of the saturated rock. In this equation, the effective density (ρ) is estimated using a conventional averaging method (Mavko et al., 2009). The elastic moduli (K and μ) can be effectively predicted using a combination of the Batzle and Wang (1992), Reuss (1929) and Gassmann (1951) equations as follows: Batzle and Wang firstly provided empirical relationships of density and bulk modulus of each fluid phase (i.e., brine, gas and oil) on pressure. Then, the effective mixed fluid proper-

ties which depend on fluid saturation can be averaged using Reuss's equation. Finally, the theoretical Gassmann equation predicts the saturated rock moduli which can then be used to calculate propagation velocities in Equation 1.3.

Besides fluid properties, dry rock properties are also pressure dependent. For this relationship, there are currently two approaches. Some studies (Landrø, 2001; Trani et al., 2011; Witsker et al., 2014) use the Hertz-Mindlin rock physics model (Mindlin, 1949). This model also stands behind a variety of other approaches that use petroelastic models (Andersen et al., 2009; Blanchard and Thore, 2013). The Hertz-Mindlin model's challenges are heavy parameterization and unrealistic assumptions (such as perfectly round matrix grain). The second, more popular way to link pressure with rock moduli is using direct empirical relationships from core samples. This approach is proven to be decent, with careful calibration in each case study (Tura and Lumley, 1999; Cole et al., 2002; Floricich et al., 2005; Floricich et al., 2006; Blanchard et al., 2010b; Blanchard, 2011).

Time-lapse seismic attributes

From the forward modeling in step 1, various seismic responses are predicted with respect to changes in pressure and saturation. These responses make up the expected time-lapse measurements, or time-lapse attributes, which are used as the input for the inversion process.

Historically, the basic attributes are time shifts and amplitude differences, but they are mainly for qualitative interpretation. AVO responses are later used (Calvert, 2005; Barkved, 2012) as illustrated by Landrø (2001), Trani et al. (2011) and Blanchard and Thore (2013). However, they are interconnected because both depend on velocity changes. This potentially violates the inversion requirement stating that the input parameters should ideally be independent.

For a stable inversion result, Calvert (2005) pointed out that at least two measurements are needed. Moreover, given that a 4D response is dominated by fluid changes, full-stack data do not represent a true zero-offset seismic response (Johnston, 2013). Therefore, other approaches use AVO derived attributes (Barkved, 2012; Johnston, 2013), for example: P-wave and S-wave velocity,

impedance and the ratios between them (Tura and Lumley, 1999; Cole et al., 2002; Floricich et al., 2005; Floricich et al., 2006; Andersen et al., 2009; Witsker et al., 2014).

Unfortunately, because AVO-derived attributes are heavily dependent on amplitude information (even time shifts are related to amplitude differences by velocity), an inversion using them as the input may be ill-conditioned. Plus, prestack seismic is not always available for estimating these attributes, especially in legacy projects. Therefore, besides the traditional attributes mentioned above, Calvert (2005) suggested that other independent attributes should be used to separate pressure and saturation effects. Some studies have used time-lapse attenuation as an independent attribute like ones by Blanchard et al. (2010b) and Blanchard (2011).

4D inversion techniques

4D inversion involves converting the measured time-lapse attributes to changes in reservoir conditions. This process starts from the link $\mathbf{F}$ between them:

$$\mathbf{y} = \mathbf{F}(\mathbf{x}), \tag{1.4}$$

where $\mathbf{y}$ are the measured 4D attributes (observables) and $\mathbf{x}$ represents the model of changes in reservoir conditions (i.e., pressure and fluid saturation).

In order to solve for $\mathbf{x}$ from $\mathbf{y}$ in Equation 1.4, there are several approaches. What is estimated ($\mathbf{y}$) in each method depends on the relationship $\mathbf{F}$. Seismic amplitude is normally related to elastic properties from the Smith and Gidlow (1987) approximation to the Zoeppritz equation. 4D signals are extended from this approximation to link to pressure and saturation changes by the rock physics template like the Hertz-Mindlin model mentioned in the previous section.

The simplest qualitative 4D inversion is cross-plotting. Changes in pressure and fluid changes are modeled to approximate P-wave and S-wave impedance (Tura and Lumley, 1999; Cole et al., 2002) or acoustic impedance ratio and Vp/Vs ratio (Andersen et al., 2009). These pairs of elastic properties are cross-plotted in 2D space to estimate relative changes of pressure and saturation.

A more analytical solution for Equation 1.4 can be quantitatively found by either solving a polynomial approximation or using the least squares approach. For example, Landrø (2001) used a quadratic polynomial approximation to estimate changes of AVO intercept (ΔR_0) and gradient (ΔG) in terms of changes in pressure (ΔP) and water saturation (ΔS) as follows,

$$\begin{aligned} \Delta R_0 &\approx 1/2\Big((k_\alpha + k_\rho)\Delta S + l_\alpha \Delta P + m_\alpha \Delta P^2\Big), \\ \Delta G &\approx 1/2\Big(k_\alpha \Delta S + l_\alpha \Delta P + m_\alpha \Delta P^2\Big) - 4\beta^2/\alpha^2\Big(l_\beta \Delta P + m_\beta \Delta P^2\Big), \end{aligned} \tag{1.5}$$

where k, l, m are coefficients determined from rock calibration and α, β, ρ refer to the P-wave velocity, S-wave velocity and density. The input of this method consists of AVO intercept and gradient changes. In his original study, Landrø (2001) considered Equation 1.5 as a quadratic equation (i.e., $y = ax^2 + bx + c$) with respect to ΔP and solved for the traditional solution (i.e., $x = \frac{-b-\sqrt{b^2-4ac}}{2a}$). Trani et al. (2011) improved the performance of this method by taking time shifts into account. In a similar approximation, Blanchard and Thore (2013) inverted time-lapse P-impedance, S-impedance and density to estimate reservoir variations.

As an example of using the full least squares approach, Blanchard (2011) linearized Equation 1.4 in the form of

$$\mathbf{y} = \mathbf{A}\mathbf{x}, \tag{1.6}$$

where matrix $\mathbf{A}$ is the linear form of $\mathbf{F}$ and used the generalized solution form

$$\mathbf{x} = (\mathbf{A^T A})^{-1}\mathbf{A^T y}. \tag{1.7}$$

He used this approach to invert for reservoir conditions from changes in attenuation, velocity and AVO intercept. Similar work was conducted by Witsker et al. (2014) taking time shifts as the only input. For these rock physics model based methods, the fact that most models are normally non-linear may introduce uncertainties during linearization transforms or quadratic approximations.

Besides the two analytical approaches mentioned above, instead of using a

defined rock physics model, the link $\mathbf{F}$ can be derived from empirical statistic relationship between reservoir conditions and elastic properties. As a result, a modified statistic inversion approach can be used. In this approach, each time-lapse attribute ΔA can be statistically approximated as a polynomial function of changes in pressure and saturation. For example, Floricich et al. (2006) extended previous works by MacBeth et al. (2004) and Floricich et al. (2005) and proposed:

$$\Delta A \approx a\Big(exp^{b(1-S)} - 1\Big) + c\Delta S + d\Delta P^2 + f\Delta P, \tag{1.8}$$

where b, c, d and f are constants determined from engineering data. As a best practice, several 4D attributes normally undergo principal component analysis to give the most suitable set for inversion. Then, a statistic model is created using the variance of the input data. Finally, a Bayesian-based inversion is applied to estimate the probability maps as the posterior distribution for pressure and saturation. Analytically, this method is an extension of Equation 1.7 with added uncertainties:

$$\mathbf{x} = \mathbf{x_{prior}} + (\mathbf{A^T C_y^{-1} A} + \mathbf{C_x^{-1}})^{-1} \mathbf{A^T C_y^{-1}} (\mathbf{y} - \mathbf{A x_{prior}}), \tag{1.9}$$

where $\mathbf{x_{prior}}$ is the priori hypothesis on the model, $\mathbf{C_x}$ and $\mathbf{C_y}$ are covariance matrices on the model $\mathbf{x}$ and the data $\mathbf{y}$, all come from the statistic model created from the input data.

Theory indicates that all quantitative approaches mentioned above are computationally expensive, especially with high dimensional models. With the same forward model $\mathbf{F}$ (from reservoir conditions to elastic properties), a simple yet effective solver is grid search. This method predicts time-lapse attributes from a predefined solution space of pressure, saturation (and maybe porosity). The prediction can be performed on the whole grid (Cole et al., 2002, input attributes are changes in P- and S-impedance) or randomly via Monte Carlo simulation (Blanchard et al., 2010b, input attributes are changes in attenuation and P-velocity). The inversion solution is found by matching the modeled attributes with the observed time-lapse measurements.

1.2 Motivation and contribution

4D technology started to become very popular in the 90's when time-lapse projects drew more attention from companies. The earliest successful projects were found in the North Sea area, for example: the Draugen, Gullfaks, Ekofisk, Valhall and Halfdan fields (Barkved, 2012). This area soon then turned into the site of extensive 4D activities with novel applications and updated technologies.

The case study in my thesis is known as one of the first 4D projects in the North sea area (Landrø, 2011). It involves the monitoring of an underground blowout well drilled by Saga in 1989, where gas has leaked into two shallow sandstone layers at different depths (Remen, 1991; Lie and Larsen, 1991). The incident also created potential safety and environment challenges (Selmer, 1991; Bysveen, 1991).

In order to address these issues, Saga started a seismic campaign to investigate gas migration in shallow sandstone formations with many seismic surveys, including 2D and 3D, through a long monitoring period of almost 20 years (Landrø, 2011). Initial studies have successfully detected gas leakage in the early stages of the blowout (1991). Project Long-term Seismic Monitoring (LOSEM), led by Dr. Martin Landrø at NTNU, continued the investigation and published significant findings from 2011 to 2014.

Nevertheless, because the legacy data were not fully acquired and processed properly for 4D analysis (Landrø, 2011; Dinh et al., 2017b), most of the recent time-lapse studies have unanswered observations. For example, Landrø (2011) noticed several 4D amplitude signals that may be residuals of multiples. Langseth and Landrø (2012) faced difficulties in explaining some particular differenced amplitude anomalies. Besides the data quality problems, monitoring the blowout is not updated by either reentering existing wells nor drilling new ones. Only old data makes it more challenging to address changes in in-situ conditions. For instance, pressure and gas saturation estimations from time-lapse attributes (Bhakta and Landrø, 2014) are only inverted at the shallow upper sandstone in the early stage (1988–1990).

These available seismic data from 1988–2005 are therefore good subjects for additional works focusing on enhancing 4D signals and improving 4D inversion results on pressure and gas saturation. These are the main goals in this the-

sis. My aim is first to establish a processing strategy to increase legacy data repeatability. I then develop a new method to invert for the final changes of pressure and saturation at different times in the two recipient sandstones. In the end, how gas migrated over time in the two recipient sandstone layers is better understood.

The first contribution of this thesis is a strategy for processing and estimating 4D attributes from these legacy data. Next, I establish a new rock physics model to link changes in pressure and saturation with measured time-lapse attenuation and time shifts. I also introduce a grid-search-based inversion method to solve for the changes in pressure and saturation within the target layers. Finally, I extend the work to estimate the gas migration rates to gain insight in possible migration rates for CO_2 sequestration.

1.3 Thesis structure

I have begun this thesis with an overview of my research area and the motivation of my research. In the next chapter, I introduce more details about the blowout case study of my research and summarize what has been done on this project. Then, the actual data available for the thesis and reasons why this is a challenging case study are presented.

I then describe how to process and calculate time-lapse attributes from these data in **Chapter 3**. I present different approaches to remove the multiples and to increase repeatability between the datasets. The main focused techniques, i.e., predictive deconvolution and surface related multiple elimination (SRME), and their parameterizations are discussed. The process of estimating time shifts and time-lapse attenuation are also described in detail with proper quality control.

In **Chapter 4** presents the theory of inversion, including forward modeling and actual inversion. Particularly I first start by summarizing the Random patchy saturation rock model. I then introduce my new pressure-dependent rock physics template based on the pore space stiffness model. A complete forward model is formed by combining these rock properties with the fluid properties from Batzle-Wang and Reuss equations. I then propose a simple yet

robust grid-search-based inversion scheme to utilize the estimated time-lapse attributes for pressure and gas saturation inversion. I also introduce my interpretation from the inversion results. I first compare my findings with previous works. Then a full combination is performed to get a better understanding about gas migration in this blowout.

I then extend my results to a practical application in **Chapter 5**. From the inverted pressure at different times, I attempt to estimate gas migration rates over these periods. The Darcy theory of fluid penetration through permeable porous media is described. I present how I adapt this model to this case study and all the parameters required to run the model. It is shown that a simple migration velocity at different times even contributes more insight to the blowout development.

In **Chapter 6**, I integrate my results with previous studies to answer some uncertainty questions raised by those authors. This helps to clarify and evaluate the blowout development more quantitatively.

Finally, in **Chapter 7** I summarize my findings and suggest potential research studies for future research.

Chapter 2

Case study

2.1 Introduction

In this thesis I focus on shallow gas migration after an internal blowout in block 2/4, North Sea area in 1989 (Figure 2.1, Mjelde and Bakøy, 1991). The 2/4-14 well was drilled by Saga Petroleum in October 1988, and kicked when hitting the Upper Jurassic target at 4,709 m below the rotary kelly bushing (mRKB) on January 20, 1989, wellhead pressure reached 69 MPa. Initial effort to control the underground blowout failed and the well was shut on January 21, 1989. The blowout preventer was then closed and the drillpipe cut. When re-entering on May 1, 1989, the pressure was observed to have dropped to 19.2 MPa.

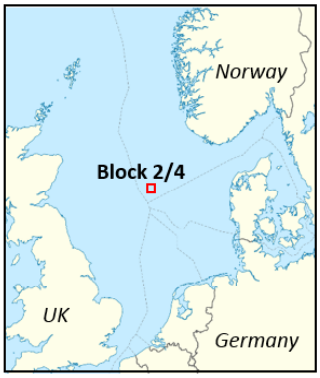

Figure 2.1: Basemap of the case study: block 2/4, North Sea area, edited from Dinh and van der Baan (2017).

In December 1989, a relief well 2/4-15S was drilled at 1,184 m to the south of well 2/4-14 and completely killed the flow (Figure 2.2). After investigating the incident, a control well 2/4-16 was planned to the Northeast of well 2/4-15. Its objectives were to test the Upper Jurassic reservoir and to potentially serve as a future production well (Bakken, 1991).

In order to monitor the hydrocarbon distribution, besides the 2D base site-survey (in July/August 1988), several 2D site surveys were repeatedly acquired by Saga Petroleum on a monthly basis within 1 year after May 1989 and in 1993 in a rectangular pattern around the well (Lie and Larsen, 1991; Landrø, 2011). 20 years later in 2009, five of these lines were acquired again by Statoil, with similar source characteristics (Figure 2.3, left). Although they are known as the first dedicated 4D seismic acquisition offshore Norway, repeatability was not emphasized when acquiring the first repeated lines in 1989 and 1990 (Landrø, 2011). Among the five lines, line 602 has different sail line positions, but three of them are very close to each other and are used for time-lapse analysis (Figure 2.3, right, Landrø, 2011). Between 1989 and 2009, two 3D seismic surveys were acquired in the same area in 1991 and 2005 (by Saga Petroleum and CGGVeritas, Figure 2.4). These 3D surveys are significantly different, in terms of both acquisition and processing (Langseth and Landrø, 2012; Dinh et al., 2017b).

Since the early stage of the blowout, Saga Petroleum has conducted various studies to investigate its development. Flow characteristics were first determined from the recorded well logs (Slungaard, 1991; Remen, 1991). Shallow gas leakage and migration were then studied from 2D seismic amplitude (Lie and Larsen, 1991). Most of these findings were presented at the Experience transfer seminar early 1991. A new project LOSEM has been launched later at NTNU and led by Martin Landrø's group to conduct time-lapse analyses for the incident. In the next section, I summarize the studies done in this area, performed by Saga Petroleum in 1991 and by Landrø's group since 2011.

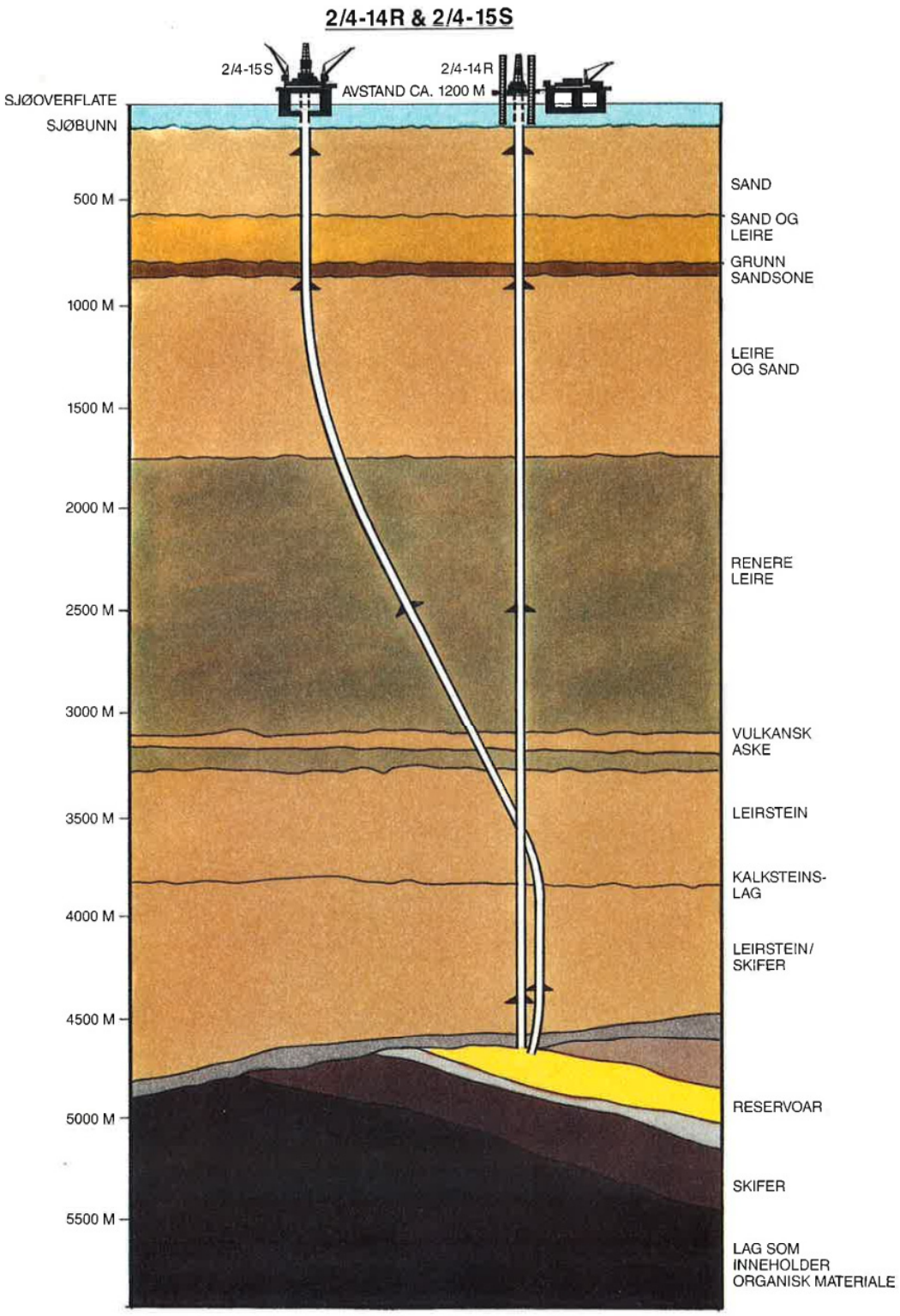

Figure 2.2: Scheme of the blowout (2/4-14) and relief well (2/4-15) approximately 1 km south from well 2/4-14, taken from Slungaard (1991).

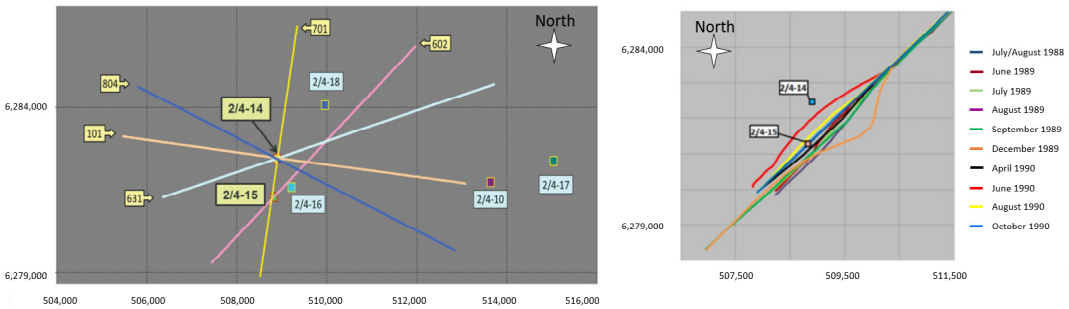

Figure 2.3: Star shaped 2D lines (left) and different sail directions of line 602 (right), edited from Landrø (2011).

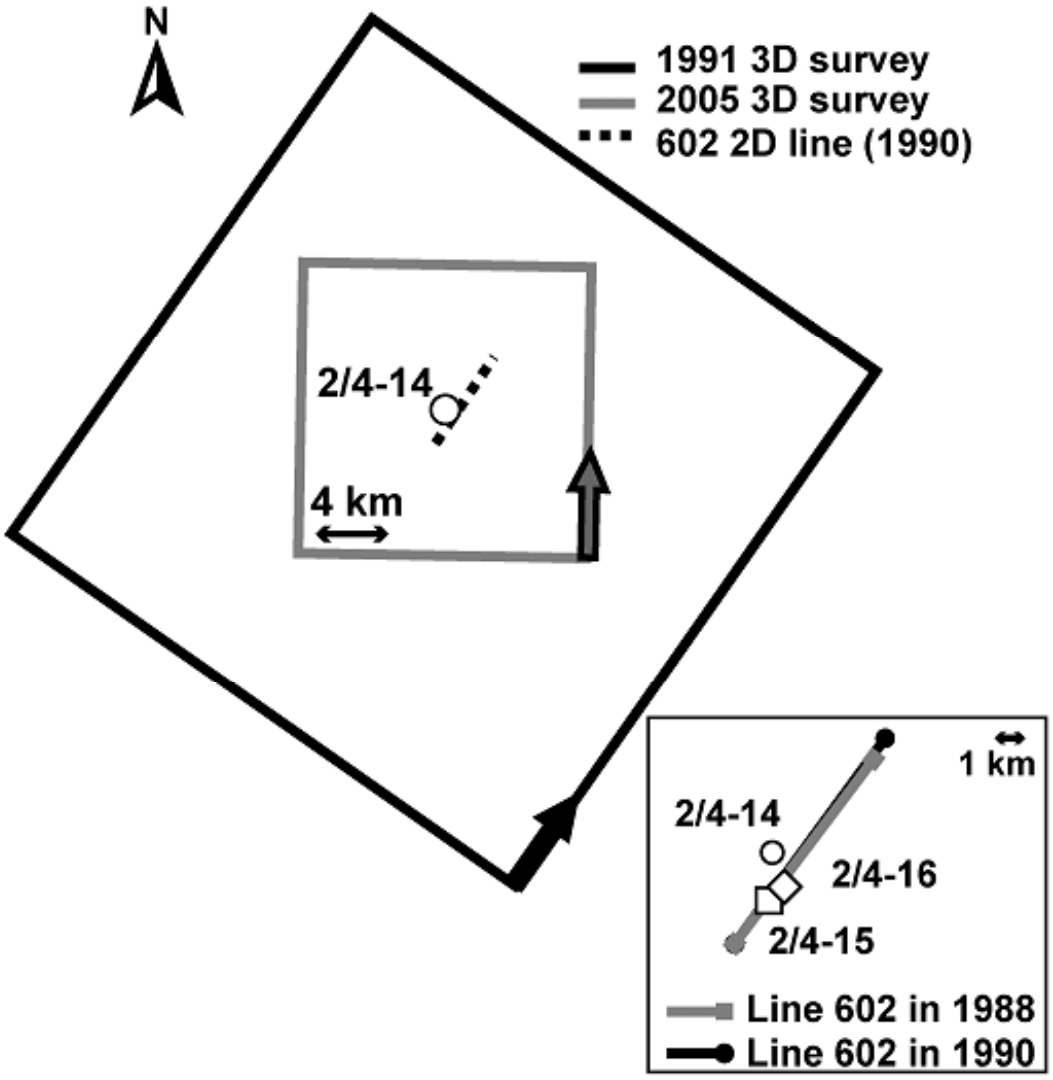

Figure 2.4: Geometry of two 3D surveys in 1991 and 2005. The 2D line 602 is also represented on these maps, taken from Dinh et al. (2017b).

2.2 Previous works

2.2.1 Flow path and characteristics, 1991

In order to handle well control problems, blowout flow characteristics were studied from log measurements when re-entering well 2/4-14 in May 1989 (Slungaard, 1991). The following information was determined: flow path, flow rate, temperature profile, pressure profile and mechanical status.

The blowout nature was determined by different techniques, namely injection of seawater and matching pressure gradient to fluid characteristics. In this case study, the blowout flow path has changed at different times because of damaged drillpipe (steel tube that turns and conducts force to the drill bit) and casing (outmost durable tube that lines and stabilizes the wellbore, normally by cementation). It was determined by various measurements from temperature, pulsed neutron and noise logs. The logs indicated a considerable underground blowout taking place between 4,700 to 900 m inside the blowout well.

Slungaard (1991) confirmed a hole in the innermost 9 5/8" casing at 1,370 m and another hole that the flow exited the well at 900 m (Figure 2.5, left and middle). Slungaard also stated that no indication of flow below 1370 m level was detected. Based on observations from fishing (operations that remove objects stuck in the borehole and have negative impact on well operations), Remen (1991) concluded that the flow path was initially up through a leaking overshot (a fishing operation tool), then down the drillpipe through the 1,370 m hole in the 9 5/8" casing. Gas continued flowing in the 13 3/8" casing and exited the well behind the 20" casing shoe (the bottom of a casing) at 900 m hole, similar to what Slungaard (1991) has concluded (Figure 2.5, left). After the hole in the overshot was closed on June 30, the flow path changed through another hole at 4,100 m, which was confirmed by photos taken in the well (Figure 2.5, middle). 4 months later, gas was detected from temperature log to flow through the broken 9 5/8" case at 850 m (Figure 2.5, right).

Slungaard (1991) estimated flow rate (from temperature logging) and pressure gradients (measurements from the surface and downhole and the determined flow path before closing the hole in the overshot). The flow rate was

found in agreement with measurements at the spinner and on the surface. The pressure gradient was found to match the fluid analysis and friction simulations.

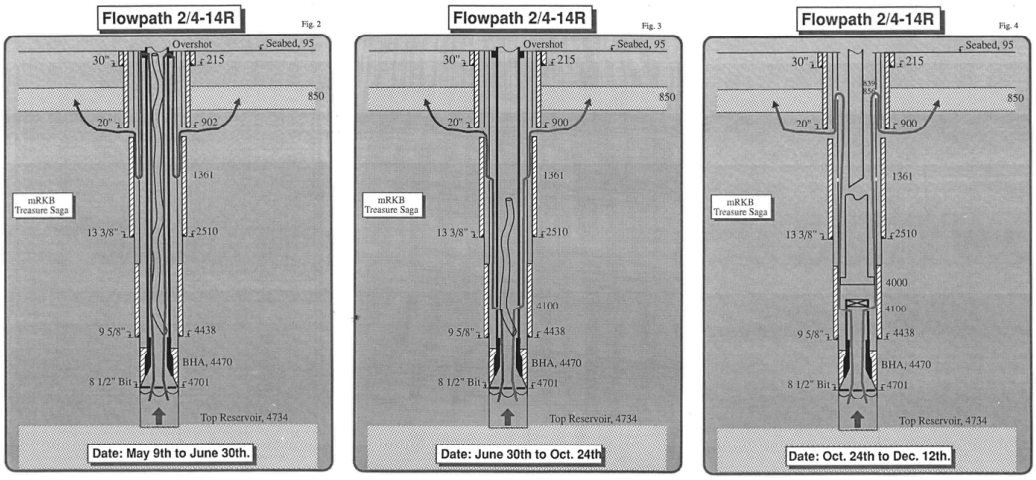

Figure 2.5: Flow path at different times in well 2/4-14, taken from Remen (1991). Gas leaked into the main recipient sandstone through the exit at 900 m depth.

2.2.2 2D seismic analysis, 1991

2D seismic amplitudes coupled with well correlation and log interpretation indicated that the gas has leaked and charged into several shallow sandstone layers (Lie and Larsen, 1991; Remen, 1991). Although the number of logs and velocity information for depth conversion were limited at these shallow depths, the results were correlated with neighbouring wells. Several seismic analyses were done including seismic modeling (confirming seismic amplitude increases with gas charging into the sandstone), AVO analysis and seismic interpretation. Table 2.1 summarizes the areal spread of shallow gas estimated from seismic amplitude anomalies in different sandstone layers. Among them, the main recipient is closest to the leaking point of the well at 828 mRKB. The other significant one is shallower at 495 mRKB.

The 828 mRKB (hereafter referred to as "828 m") sandstone is a South-west dipping 87 m thick formation (Figure 2.6, lower sandstone). Lie and Larsen (1991) observed that in later surveys, seismic amplitude at this sandstone dropped because of the dimming effect when gas charged into shallower

sandstone recipients. The mapping of observed amplitude anomalies at this deeper sandstone (Figure 2.7) indicated that gas had moved toward the Northeast, confirming the expected distribution relative to the dip of the sandstone body. 10 months after reentry, the lateral extent of the anomaly in this sandstone was in the order of 15 km^2. Seismic modeling results from Lie and Larsen (1991) suggested that gas has filled the uppermost 2 meters instead of the whole sandstone thickness. However, Remen (1991) raised some uncertainty regarding the thickness of gas anomaly that can be seen on seismic. He believed that the entire 828 m sandstone was charged thanks to new fracture flowpaths caused in early September 1989 by the local built up pressure and fluid and well operations.

The other important recipient formation at 495 mRKB (hereafter referred to as "495 m") is a 10 m thick flat sandstone layer (Figure 2.6, upper sandstone). It is detected by a strong seismic event observed since the fourth survey in September 1989 (Table 2.1), four months after re-entry, coincident with the reduction in lateral expansion rate of the 828 m sandstone at surveys 3 and 4. If vertical migration of gas from the 828 m sandstone into this 495 m sandstone and possible shallower sandstone layers occurred, it would have happenned between these surveys. From samples of reservoir gas, combined with the local build up of pressure, Remen (1991) suggested a vertical flow path through the cement and/or formations near the blowout well. However, the real vertical migration path is still unknown. The seismic anomaly at the 495 m sandstone is roughly similar in all directions (Figure 2.7). By 1990, anomalies in this sandstone are about 3 km^2.

In Table 2.1, gas accumulation in other sandstone layers are also investigated, for example, at 605 m, 562 m and 523 m. Among them, gas was believed to be present in the 605 m sandstone prior to the blowout because it was detected from the 1988 seismic data and confirmed when drilling well 2/4-14 (Lie and Larsen, 1991). The other two sandstone layers started receiving gas since the fifth seismic survey. Unfortunately, gas spreading after this time was not able to be mapped because seismic observations at these layers were masked by gas effects in the shallower 495 m recipient (Remen, 1991). Lie and Larsen (1991) believed gas continued to charge into even another shallower sandstone

layer at 445 m because of the observed pull-down effect observed at the 495 m sandstone around the well location. However, only minor changes in seismic response at this sandstone are observed in later surveys (in October and December 1990). Lie and Larsen (1991) concluded that lateral and vertical migration seem to stop after the seventh survey (May 1990).

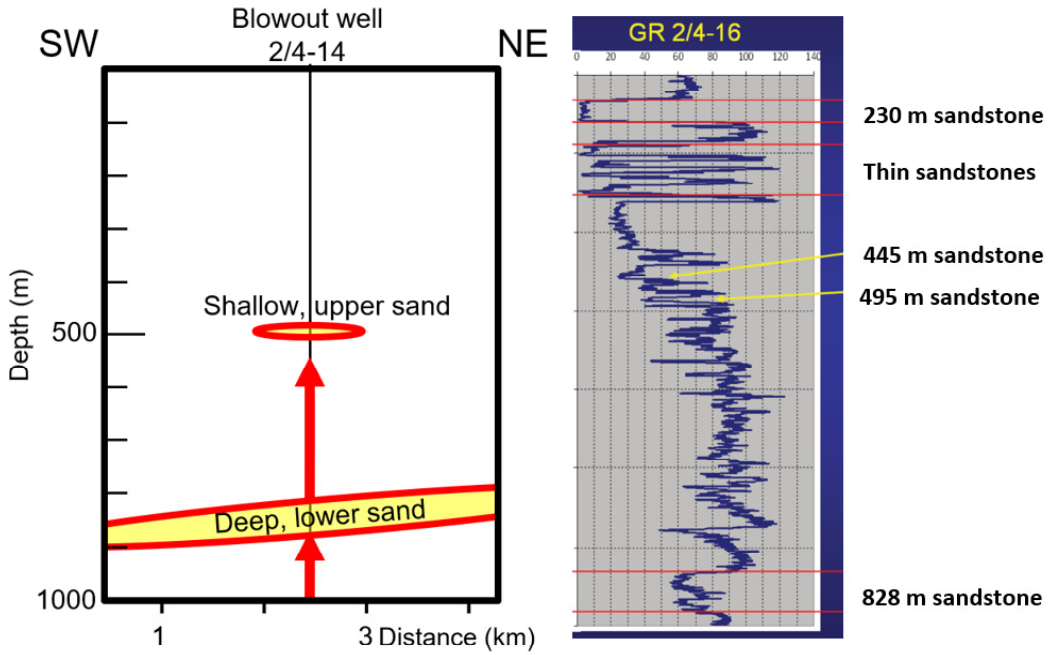

Figure 2.6: Left: the two main shallow recipient sandstone layers including (1) the 87 m thick deep sandstone is South-West dipping at 828 mRKB and (2) the 10 m thick shallow sandstone is flat at 495 mRKB, edited from Dinh and van der Baan (2017). Right: GR log showing the 828 m, 495 m and other sandstone layers observed from well 2/4-16, taken from Landrø (2011).

Survey	Time collected	828 m	605 m	562 m	523 m	495 m
1	Jun 11–13, 1989	2.0				0
2	Jul 3–8, 1989	5.2				0
3	Aug 6–19, 1989	8.0				0
4	Sep 21–29, 1989	9.7				0.5
5	Nov 24–Dec 2, 1989	14.8	1.8	0.7	0.6	1.8
6	Feb 15–Mar 14, 1990	16.9	*	*	*	3.9
7	May 16–27, 1990	*	*	*	*	4.2

Table 2.1: Lateral gas spread (km^2) from seismic anomaly of different sandstone layers, * Not able to interpret due to masking by gas expansion in the sandstone at 495 mRKB or masking by other seismic signals, taken from Remen (1991).

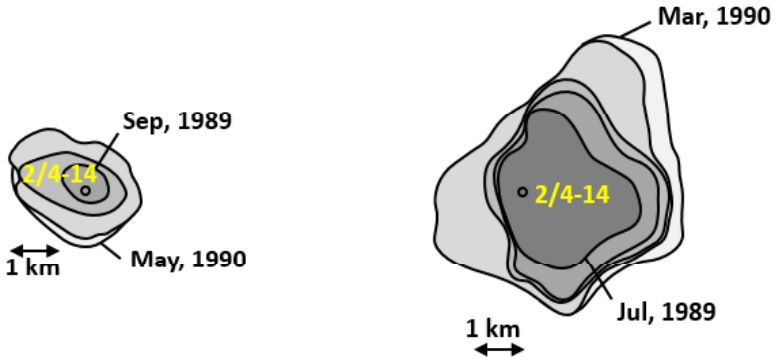

Figure 2.7: Gas migration 12 months after the blowout, from 2D seismic amplitude anomalies (edited from Lie and Larsen, 1991). Gas movement in the deep sandstone (right) is elongated towards the Northeast. However gas spread more uniformly in the shallow sandstone (left). Both agree with the geological structure of the area.

2.2.3 Reservoir simulation, 1991

An initial 2D reservoir simulation was also conducted to estimate pressure distribution and simulate fluid flow in the 828 m sandstone by Remen (1991). He estimated flow volume from the spinner rate measurement and suggested that the 828 m sandstone was fully charged before May 1989. The model used bottom hole pressure as the boundary condition and assumed the sandstone was 0.5 degree dipping toward the West. The simulation results suggested an insignificant overpressure of 0.3–0.4 MPa in this sandstone by the end of 1990 (Figure 2.8), and that gas has laterally extended in a similar distance with the observed seismic anomalies (Lie and Larsen, 1991) but elongated to the modeled updip East direction (Figure 2.9). From this simulation, Remen (1991) concluded that vertical flow was limited and stopped around April 1990.

2.2.4 Time-lapse analysis, 2011

Landrø (2011) summarized the blowout development and performed his analysis on the time shifts and amplitude differences of the raw stacked 2D seismic data acquired in 1988, 1989, 1990, and 2009. He observed strong amplitude anomalies which are related to gas accumulation in several shallow sandstone

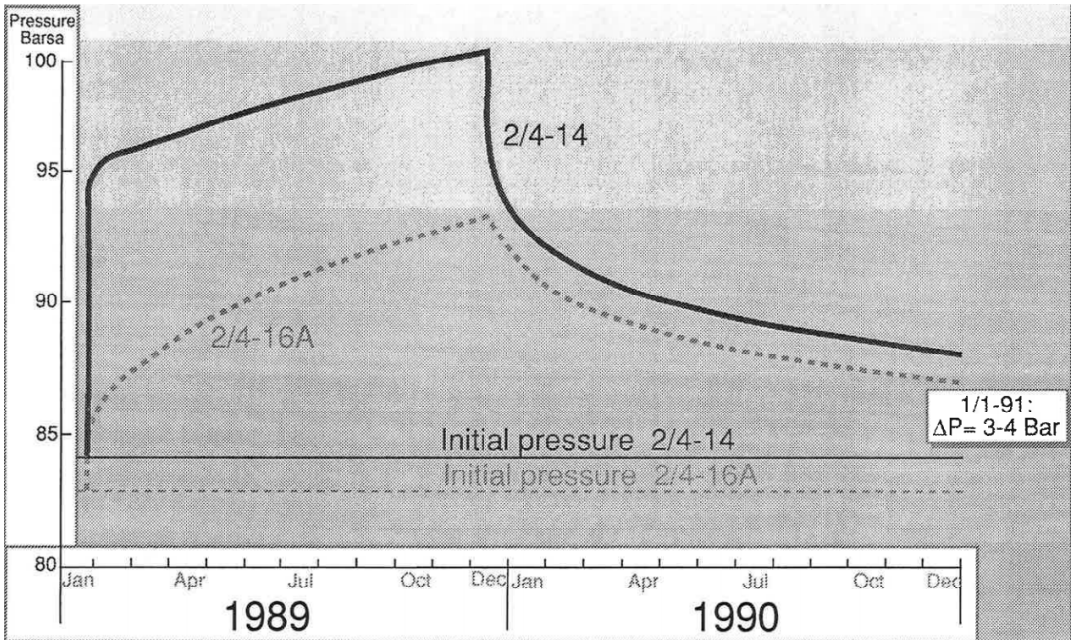

Figure 2.8: Simulated pressure over time within the 828 m sandstone (taken from Remen, 1991). The overpressure state started to reduce after drilling the relief well (December 1989).

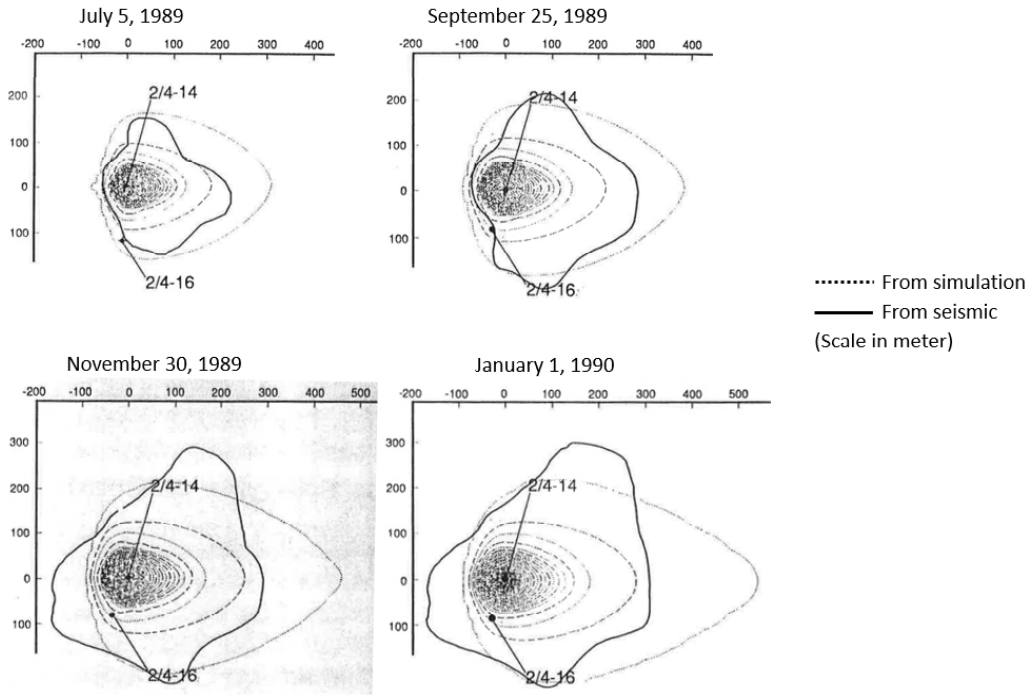

Figure 2.9: Reservoir simulation in the two sandstone layers within a year after the blowout (taken from Remen, 1991). The simulated gas spread is in relatively good agreement with the seismic anomaly in early stages.

layers (including the 495 m sandstone). However, some of them might be related to multiples as the data were simply raw stacks without multiple removal and migration.

The amplitude differences between 2009 and 1990 indicated gas accumulation in the shallow sandstone and showed very slow lateral migration (Figure 2.10). The time-shift observations in the same time frame suggested lateral extension of gas in the shallow sandstone. Figure 2.10a also indicates significant amplitude changes close to the relief well at 650 ms. This could be a representation of gas in the 605 m sandstone. However, because the anomaly does not agree with the dipping structure of the sandstone, Landrø (2011) interpreted this event to be caused by the horizontal gas migration in the 495 m sandstone (at 520 ms). 4D amplitude differences from other 2D lines also showed various uncertain anomalies that cannot be explained, especially the shallow anomalies observed between 300–450 ms (Figure 2.10b).

Landrø (2011) suggested a stronger lateral migration than vertical migration around the well. From time-shift analysis, he also believed that (1) most of the gas migration after 1990 has occurred in the depth interval between the two sandstone layers (450–800 m) with no leakage above 420 m and that (2) the gas that has accumulated within the 828 m sandstone in 1990 is still there by 2009. The study noted the difficulties estimating gas saturation changes, even qualitative, because the effective seismic signal caused by 20% and 80% gas are similar.

2.2.5 Time-lapse analysis and reservoir simulation, 2011–2012

Eli Langseth in her thesis (Langseth, 2011) and a later publication with Martin Landrø (Langseth and Landrø, 2012) performed a detailed time-lapse analysis (on 2D seismic data and 3D seismic surveys) and a 2D reservoir simulation, in both sandstone layers.

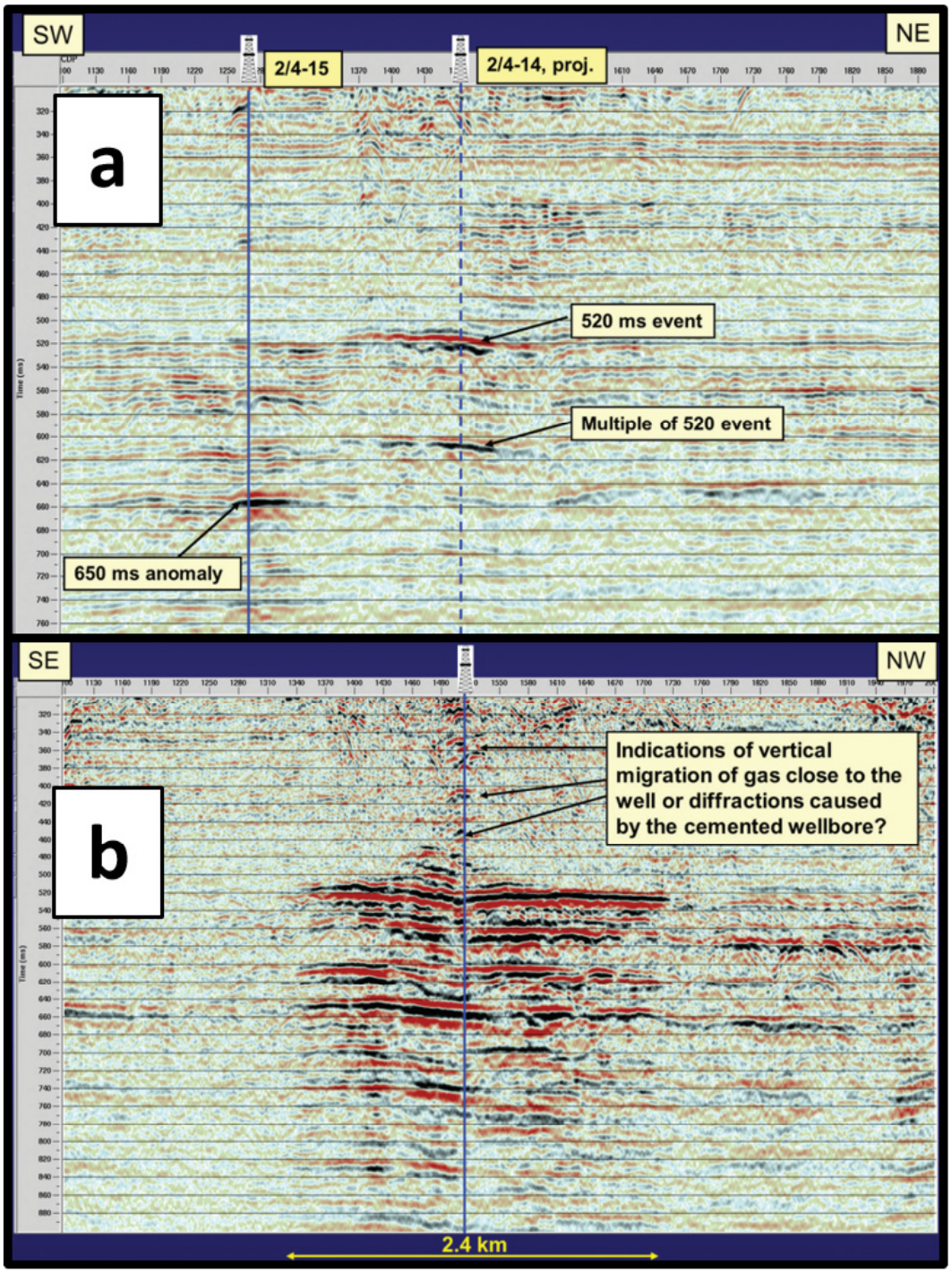

Figure 2.10: a) Amplitude differences between 1990 and 2009 of line 602 showed an increase at the 495 m sandstone (520 ms) and its potential multiple (610 ms). The challenging anomaly at 650 ms can be interpreted by either gas charging into the 605 m sandstone or by time-shift shadow of gas charging into the 495 m sandstone. b) Amplitude differences between 1988 and 1990 of the perpendicular line 804 showed anomalies around the well. Taken from Landrø, 2011.

Time-lapse analysis from 2D data

Using the same 2D lines as in Landrø (2011), these studies noticed an amplitude increase at the 828 m sandstone after the blowout in August–September 1989 and significant amplitude drop in the August–October 1990 survey (Figure 2.11, top row). However, the amplitude responses were not very clear with large variation, both positive and negative and were inconsistent with the observed time shifts (Figure 2.11, top and middle row). On the other hand, a noticeable increase of amplitude and time shifts were observed in the 495 m sandstone (Figure 2.11, bottom row) in the later survey (August–October 1990).

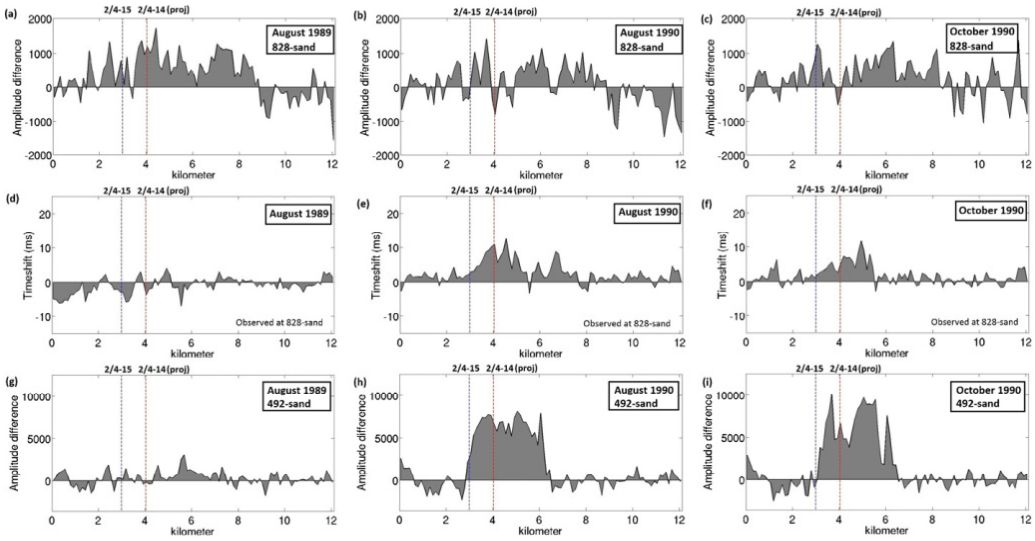

Figure 2.11: Time-lapse observations in the two shallow sandstones at different times: August 1989 (left), August 1990 (middle) and October 1990 (right). Top and middle: amplitude differences and time shifts at the 828 m sandstone. Bottom: amplitude differences at the 495 m sandstone. Although time-lapse signals are clear in the 495 m sandstone, amplitude differences and time shifts at the 828 m sandstone are not fully consistent. Taken from Langseth, 2011.

Time-lapse analysis from 3D data

From the separated 3D survey in 1991, time structure and amplitude maps of the two sandstone layers were picked by Langseth (2011). Very weak amplitudes were observed for the deep sandstone. However, at the shallow sandstone a strong circular anomaly with nearly zero value around the well was

found (Figure 2.12). These observations at the shallow sandstone agreed with previous findings of Landrø (2011) but questioned the termination of vertical gas migration by Lie and Larsen (1991) because lower gas concentration due to vertical gas movement seemed to be a good explanation for the dim amplitude close to the well. As the 3D 1991 shallow anomaly dimension was found to be similar with gas extent in 1990 mapped by Lie and Larsen (1991), Langseth suggested no lateral expansion of gas in the 495 m sandstone.

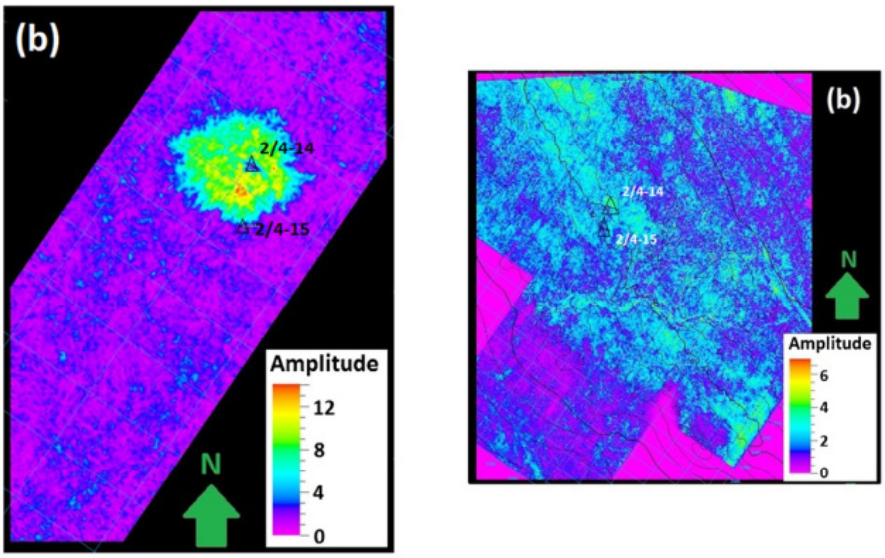

Figure 2.12: Clear amplitude anomalies of the shallow (left) and dim signals at the deep (right) sandstone layers from the 1991 3D seismic survey. Taken from Langseth (2011).

2D fluid simulation

The main differences between the 2012 simplified 2D reservoir simulation by Langseth (2011) and the older one by Remen (1991) are that the more recent model (1) assumed flat sandstone layers and (2) used bottom hole pressure as the injection pressure condition. Langseth also reran the simulation in different scenarios with varying parameters, namely permeability, perforation interval, injection pressure and shallow gas leak, and at different times in 1989, 1990 and 1996. Her modeled pressure was found to be much higher than that estimated by Remen (1991) but can be reduced by adjusting the model parameters.

The simulation results from all scenarios showed that in 1989, the deep sandstone layer was entirely overpressured and charged by gas with highest accumulation at the blowout well (Figure 2.13, bottom row). The modeled pressure and gas saturation have reduced over time. By October 1996, the pressure profile is almost close to hydrostatic pressure except slightly underpressurized at the well location (Figure 2.13, lower left). Gas saturation around the well is lower than in 1989 with more reduction at the well location. At distances more than 2 km away from the well, more gas is accumulated in the deep sandstone.

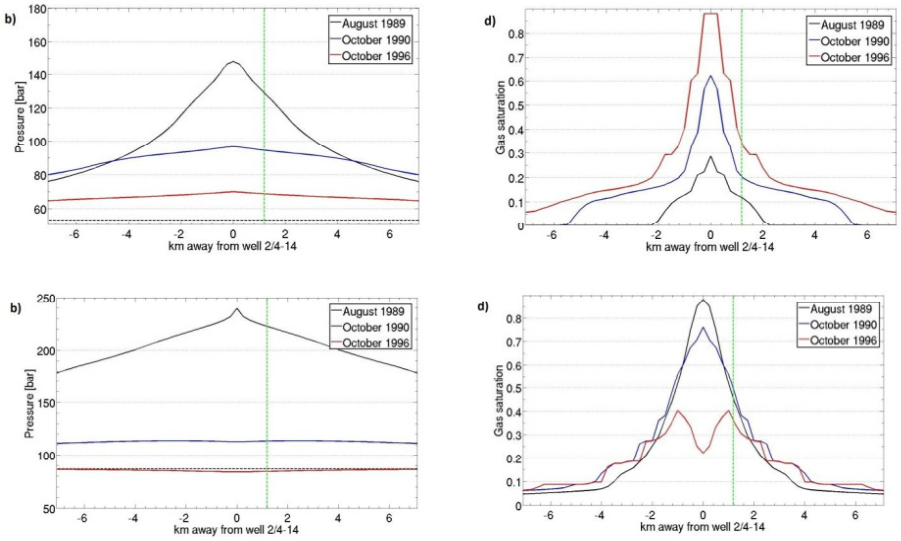

Figure 2.13: Reservoir simulation of pore pressure (left) and gas saturation (right) of the shallow 495 m (top) and deep 828 m (bottom) sandstone layers in 1989, 1990, 1996. Pressure reduction is observed at both sandstone layers, with modeled underpressure in 1996 in the deep sandstone. Gas saturation appears to reduce over time in the deep sandstone but keeps increasing in the shallow sandstone. Taken from Langseth, 2011.

At the shallow sandstone, similar pressure situation is estimated in 1989 (Figure 2.13, top row). Pressure has reduced slowly and this entire sandstone layer is still overpressured by 1996. Langseth observed that pressure propagation in this 495 m sandstone was slower than that in the deeper 828 m sandstone. On the other hand, the simulation showed an increase in gas saturation and gas extension, indicating gas was still charging into the sandstone from 1989 to 1996.

When comparing the simulation results with time-lapse analysis, Langseth (2011) found that in the shallow sandstone, (1) the observed time-lapse effects were caused by gas saturation with similar extension of the gas plume, and (2) that modeled pressure changes were not reflected by any corresponding signals on the measured time shifts. At the deep sand, the author mentioned the interpretation challenges because of the damped amplitude changes and insignificant time shifts, which do not fully agree with the simulated pressure and gas saturation.

2.2.6 Pressure-saturation inversion, 2014

The study by Bhakta and Landrø (2014) is the first one that used seismic data to perform 4D inversion in this area. The inversion was done on the two 2D seismic surveys acquired in 1988 and 1990 as used by Landrø (2011), Langseth (2011) and Langseth and Landrø (2012) with simple bandpass filtering and amplitude scaling. The inversion methodology was modified from the original AVO method proposed by Landrø (2001). The input attributes were changes in AVO intercept and gradient. Detailed parameterization was done to calibrate the forward rock physics model.

This study inverted for changes in pressure and gas saturation in the shallow sandstone between 1988 and 1990. The results (Figure 2.14) showed an increase of both gas saturation and pressure around the blowout well, which indicated new gas charging into this sandstone in this time interval. Nevertheless, the exact quantitative changes of pressure and gas extent are much less than that simulated by Langseth (2011) (Figure 2.13, top row, black curves).

2.2.7 Summary

This blowout was an unfortunate incident and efforts were made to investigate its development. Different studies have agreed on the two main shallow recipient sandstones at 828 m and 495 m. Gas charging into these sandstones were detectable from seismic data. At the shallow 495 m sandstone, evidence from reservoir simulations, time-lapse amplitude analyses and 4D seismic inversion have proven pressure and fluid build up around the well.

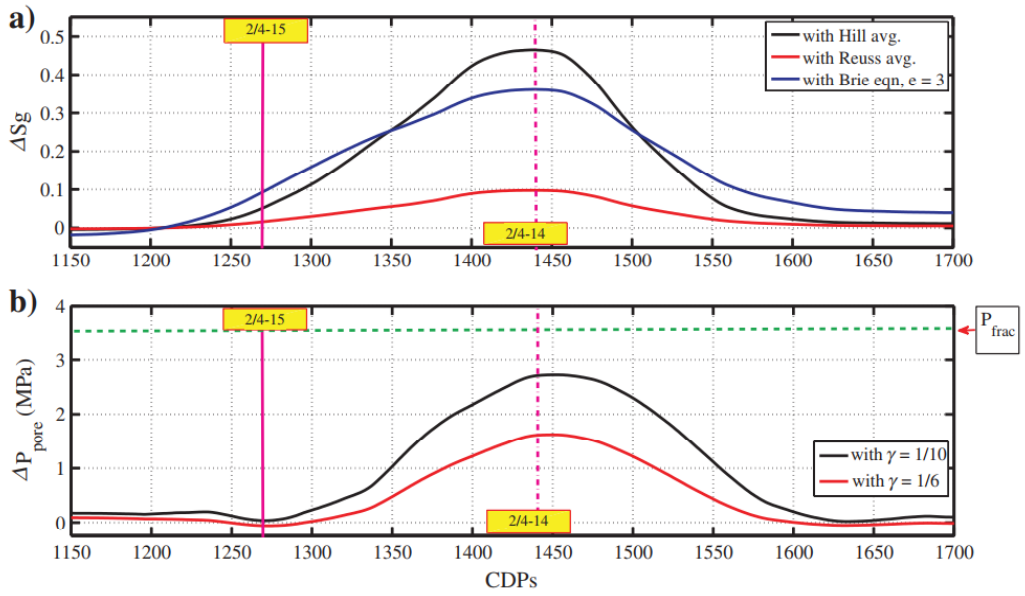

Figure 2.14: Gas saturation (top) and Pore pressure (bottom) inversion results. Curves represent different results corresponding to different parameterizations for the rock physics calibration: different fluid averaging methods (top) and different Hertz-Mindlin exponent (bottom). The final inverted pressure is selected with exponent of 1/10 (red curve, bottom). Gas is believed to charge and keep spreading from the well location into the sand layer. New gas accumulation also increased pore pressure in the sandstone body with maximum pressure around the well. Both pressure and gas saturation increase appear to stop by the relief well 2/4-15. Taken from Bhakta and Landrø (2014).

At the deeper 828 m sandstone, the poor repeated data quality allows understanding only at the early time (all studies). Poor quality also prevents clear and consistent indications between attributes at this sandstone as mentioned by Landrø (2011), Langseth and Landrø (2012) and Langseth and Landrø (2012). Long-term investigations in later time periods (after 1991) are limited at fluid simulations without supporting 4D seismic signal confirmation (Remen, 1991 and Langseth, 2011).

Besides these, there are other findings in this project that raise disagreement between researchers or critical questions that have remained unanswered:

- After the blowout, is there continuous influx that comes from a deep down source?

- Is there vertical communication between shallow sandstone layers? What explains the uncertainties in 4D images observed at the shallow portion (Landrø,

2011)? Is the 4D anomaly at 650 ms (Figure 2.10) caused simply by gas charged in the 605 m sandstone as detected on seismic also by Lie and Larsen (1991) or by the time-shift shadow of gas charged into the 495 m sandstone (Landrø, 2011)?

- If there is vertical gas migration: What is the flow path? Is it still going on by 1991 (Langseth and Landrø, 2012) or did it stop? If it stopped, did that happened in April 1990 (Remen, 1991) or later in October 1990 (Lie and Larsen, 1991)?

- About lateral gas migration: Did it stop in the 495 m sandstone by October 1990 as suggested by Lie and Larsen (1991) and agreed by Langseth and Landrø (2012)? In the 828 m sandstone, did it also stop in October 1990 (Lie and Larsen, 1991)?

- At the deep 828 m sandstone, where all studies are limited: Did gas charge the entire thickness (Remen, 1991) or just the top 2 m (Lie and Larsen, 1991)? How reliable are the predicted pressure results of Remen (Figure 2.8) and Langseth (Figure 2.13): What are the better pressure estimations at the well location in August 1989 and October 1990, did it reduce respectively from 9.87 to 8.88 MPa (Remen, 1991) or from 15.5 to 11.25 MPa (Langseth, 2011)? In the long term monitoring, would the pressure in the sandstone layer move from overpressured to equilibrium (Remen, 1991) or to underpressure (Langseth, 2011)?

2.3 Challenges

I have briefly introduced the case study and previous works that have been done in this project. The early development of the blowout was successfully detected and monitored from logs and seismic data (Slungaard, 1991; Lie and Larsen, 1991; Remen, 1991). However, because most direct well measurements were recorded around the blowout time, long-term monitoring must rely on time-lapse seismic surveys. Unfortunately, the seismic data were not fully acquired and processed for 4D purposes. Therefore, most time-lapse studies on gas migration are partly limited. There is room for quality improvement in time-lapse image processing to produce better time-lapse attributes (such as for

Landrø, 2011; Langseth, 2011). Low seismic signal observed at the 828 m sandstone also prevents deeper understanding of hydrocarbon conditions in the main recipient sandstone, and only the shallow 495 m sandstone conditions are quantitatively inverted from seismic data (Bhakta and Landrø, 2014). Last but not least, since the gas bearing shallow sandstones are not commercial reservoirs, the lack of direct field measurements after 1991 makes it difficult to verify long-term simulations like one by Langseth (2011), and the inversion by Bhakta and Landrø (2014) was done using the 1988–1990 seismic data.

In this thesis, I present a thorough work flow for these legacy data to address better the limitations and questions mentioned above. First I find a method to reprocess the data and increase repeatability. With new time-lapse attributes calculated from the reprocessed data, I then introduce a method to invert them for changes of pressure and saturation in the two main sandstone recipients. At the end, I provide a simple time-lapse application of estimating the gas migration rate from the blowout.

Chapter 3

Processing and attribute calculation [1]

Many vintage reflection seismic surveys exist that have non-repeated acquisition geometries or final-stacked/migrated sections that are obtained using different or non-consistent processing flows. This may lead to derived time-lapse attributes that are not internally consistent or even conflicting. For instance, I have focused on a subsurface gas blowout that occurred in 1989 in the Norwegian sector of the North Sea. The 2D site survey data were acquired in 1988 and 1990, and the 3D data were acquired in 1991 and 2005. The various sets of legacy data are plagued by poor repeatability among data acquisitions, application of different processing strategies, missing prestack data, and the presence of multiples. All of these factors severely complicate even qualitative interpretation of the gas migration associated with the underground blowout. Careful time-lapse processing may provide useful information even from such challenging legacy data by first computing numerous attributes including instantaneous amplitude differences, time shifts, time-lapse attenuation, and impedance inversions. Then, judicious quality control, invoked by comparing the various attributes, is used to check for internally consistent results.

[1] A version of this chapter has been published as Dinh. N. H., van der Baan, M. and Landrø, M., 2017, Processing and quality-control strategies for consistent time-lapse seismic attributes: A case history on an internal blowout using vintage data, Geophysics, 82(4), B135–B146, doi: 10.1190/GEO2016-0448.1

3.1 Introduction

Time-lapse images are traditionally analyzed by computing differences in amplitudes, impedances and/or two-way time shifts since these all indicate changes of petrophysical properties within the reservoir due to temporal variations in velocity and/or density (Calvert, 2005; Landrø, 2010; Barkved, 2012). Such temporal differences show how the seismic response changes during hydrocarbon production. The various difference sections are often easier to interpret in terms of temporal changes than the individual vintage sections because of their ability to suppress strong geological features.

Amplitude differences can both be measured on the migrated sections or on the prestack seismic data. The first approach computes changes in instantaneous amplitudes (or equivalently impedances) to variations in density and P-wave velocity (Calvert, 2005; Barkved, 2012). The advantage of computing time-lapse amplitude-variations with offset (AVO) is that this approach highlights temporal changes in the Poisson's ratio which is very sensitive to fluid effects (Landrø, 2010; Barkved, 2012), even if solely P-wave data are acquired.

A less common, but still promising, approach is to compute time-lapse changes in attenuation (Blanchard et al., 2010a; Blanchard, 2011) since attenuation depends both on pressure and fluid saturation (Winkler and Nur, 1979; Murphy, 1982; Klimentos and McCann, 1990; Koesoemadinata and McMechan, 2001), which are both important parameters in reservoir production and simulations (Calvert, 2005; Landrø, 2001). Attenuation is however often regarded as a very challenging parameter to estimate (Reine et al., 2012b; Reine et al., 2012a).

Irrespective of the desired interpretational attributes, two conditions must be met to achieve the best interpretation. First, it is essential that all acquisition geometries have high repeatability (Landrø, 1999; Kragh and Christie, 2002); second, implemented processing steps should emphasize true geologic time-lapse differences instead of introducing 4D artefacts (Calvert, 2005; Barkved, 2012). High repeatability is achieved by systematically repeating the acquisition geometries and strategies. The purpose of 4D processing is to correct vintages for both coherent and random noise, for instance by processing all vintages with identical routines and parameters. Even good repeatability time-

lapse data can lead to poor time-lapse results if they are processed differently. Yet, high-quality processing will also seek to remove differences in seismic vintages introduced by non-repeated acquisition geometries.

The objective of our study is to analyze the spatial and temporal evolution of an underground blowout that happened in 1989 in the Norwegian sector of the North Sea (Mjelde and Bakøy, 1991; Landrø, 2011). Efforts to stop the blowout at well 2/4-14 were made both from the well head and by drilling a relief well 2/4-15 (Bakken, 1991). The blowout was killed by injection of heavy material through the relief well. Several seismic surveys were acquired over time, all using significantly different acquisition and processing strategies, producing multiple 2D and 3D legacy datasets with for instance different shot and receiver intervals. This led to considerable repeatability issues which severely complicate accurate interpretation of the evolution of the gas leakage both spatially and over time (Landrø, 2011).

This thesis focuses on our processing strategies to handle the various challenges imposed by the highly varying acquisition geometries across all vintages. I first describe the various 2D and 3D datasets including processing and quality-control strategies to obtain high-quality time-lapse attributes. I then compute a variety of time-lapse attributes, including poststack differences in instantaneous amplitudes, attenuation and two-way travel time shifts, as well as prestack attributes such as AVO characteristics and impedances. I emphasize both our criteria for choosing specific processing parameters as well as identify areas which may be dominated by processing artefacts, thus to be avoided in later interpretations.

3.2 Data sets

3.2.1 2D data

Various 2D seismic lines were acquired between 1989 and 1990 after the subsurface blowout, as well as one in 1988 prior to the blowout (Lie and Larsen, 1991). Here, I use the first and last 2D data sets, namely, sail lines 602 crossing the relief well 2/4-15, acquired, respectively, in July/August 1988 and October

1990 because they have the best repeatability (Landrø, 2011). I refer to them as the 1988 and 1990 2D data sets in this thesis. Indeed, at the time of acquisition, time-lapse monitoring was in its infancy, and repeatability was not yet in focus. As a consequence, there are deviations in the sailing coordinates (Figure 3.1) due to feathering as well as differences and irregularities in shot intervals between both 2D data sets. Nonetheless, both acquisition configurations are largely similar with identical sources and 75% of common depth point (CDP) coordinates are within 30 m.

Figure 3.2 shows the nearest offset traces from two vintages. Leaked gas from the internal blowout is believed to have escaped into two shallow sandstone layers at 495 and 828 m, respectively (Remen, 1991). The shallow gas sandstone at 495 m is expressed by a strong, horizontal negative event (negative reflection coefficient) at 520 ms, whereas the deep sandstone at 828 m is a dimmer, dipping negative event found at 880 ms at the well location. Both events have significantly higher amplitudes on the 1990 section (Figure 3.2b).

Strong multiples are also visible in Figure 3.2 (black arrows). The 90 ms seabed reflection has its first- and second-order multiples at 180 and 270 ms, respectively. They have alternating polarities, yet mimic the topography of the seabed reflection. The shallow gas sandstone at 520 ms has a corresponding multiple at 610 ms. The time separation of 90 ms between these primaries and their multiples indicates a one-time reverberation within the water layer. Similarly, the arrival at 740 ms is recognized as a multiple of the 650 ms event. All these multiples introduce unwanted signal in the difference sections, likely biasing their interpretation. Fortunately, the original shot gathers are available for the 2D data for reprocessing.

3.2.2 3D data

I also used two 3D data sets acquired in 1991 and 2005, respectively (Landrø, 2011; Langseth and Landrø, 2012), both covering the 2D lines. Unfortunately, only the final migrated, demultipled data sets are available but not the original shot gathers. In addition, each data set has different acquisition geometry (Figure 3.1) and was acquired by different contractors. The sail lines of the

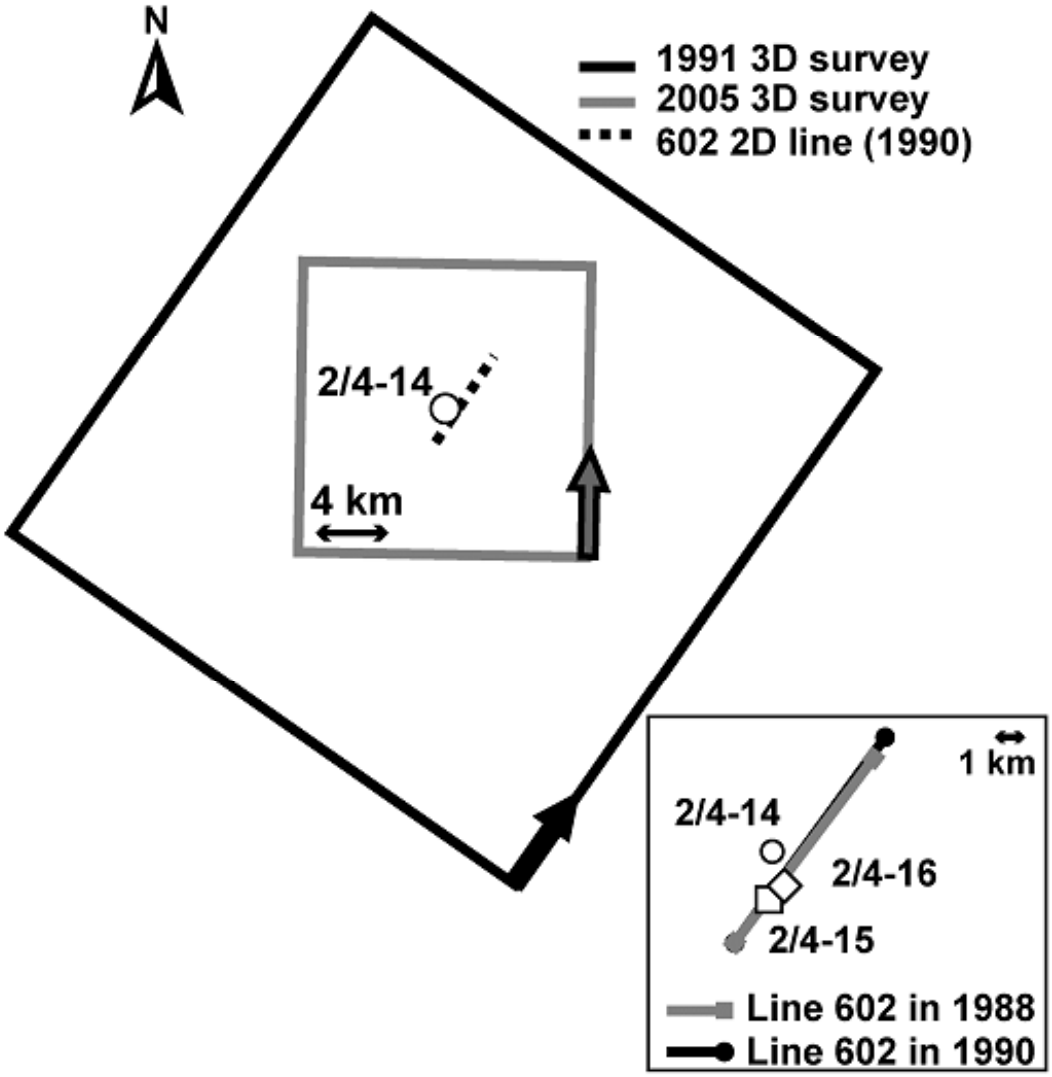

Figure 3.1: Top left: Base map of 3D surveys in 1991 (black square), 2005 (gray square), relative to the 2D lines (dashed line) and the location of blowout well 2/4-14 (white circle). Severe differences in 3D acquisition geometry exist including different sail directions (arrows). Lower right inset: Magnification of the 2D lines and well locations: Surface position of line 602 acquired in 1988 (gray) and 1990 (black) and locations of the blowout well 2/4-14 (circle), relief well 2/4-15 (square), and control well 2/4-16 (diamond). Both lines overlap except for the feathering effect at the northeast end.

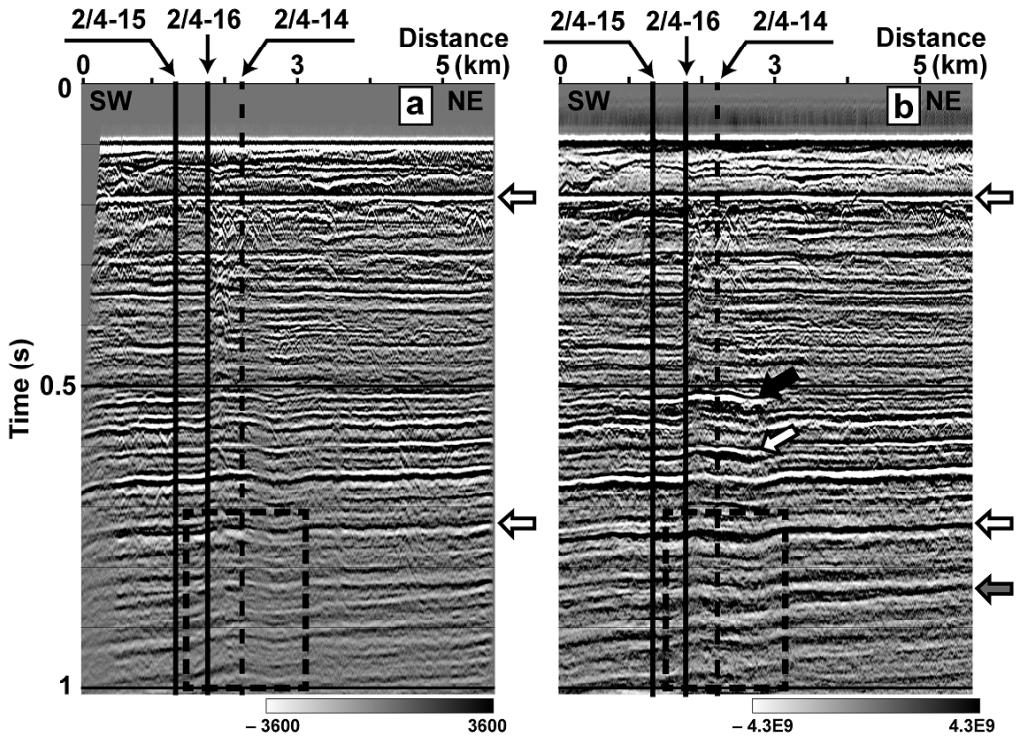

Figure 3.2: Near-offset traces of the (a) 1988, (b) 1990 2D data and projections of well locations (wells 2/4-15, 2/4-16 are marked by vertical solid lines and projection of well 2/4-14 is marked by the vertical dashed line). Sandstone layers at 495 (black arrow) and 828 m (gray arrow) are at 520 and 880 ms, respectively. Note the presence of multiples (white arrows) of the seabed and the two sandstone layers. The dashed square indicates the push-down effect. Data are displayed in reverse SEG polarity standard.

1991 data set are oriented from the northeast to the southwest, and this data set covers an area of 1,082 km^2. This base vintage was recorded with a two-source, eight-streamer configuration. Each streamer used 480 channels with 12.5 m group interval. On the other hand, the sail lines for the 2005 monitor data set are in the north-south directions. This data set covers a smaller area of 237 km^2. Data were acquired using two streamers, each containing 727 channels at a 12.5 m separation. Information on the actual source configurations for these surveys is not available, but they are likely to be different as well.

As a further complication, these 3D data sets were processed differently, and the original shot gathers were not available for reprocessing for this work. In 1991, data set multiples were removed using f–k dip filtering. The 1991 data were migrated by a poststack, onepass, finite-difference migration scheme. Conversely, the 2005 data set was migrated using a prestack Kirchhoff algorithm and multiples were removed using a Radon-based technique applied before and after migration. Furthermore, spectral balancing was applied to the 1991 data set, and inverse Q-compensation was used for the 2005 data set. Finally, a mistie of approximately 16–17 ms is observed between the data sets, suggesting that different static corrections were used. The two target sandstone layers are observed slightly later on the original 2005 data set than on the 2D data, respectively, at 540 and 900 ms at the blowout well location.

The vastly different acquisition and processing strategies for each 3D data set render them far from ideal for time-lapse monitoring. Further complications arise because the original shot gathers were not available. Unfortunately, these are not unusual challenges given that most vintage data were acquired before the importance of high repeatability and synchronized processing was realized for reliable time-lapse interpretation (Calvert, 2005; Barkved, 2012). This thesis focuses on our implemented strategies to overcome the encountered processing challenges for these 2D and 3D vintage data.

3.3 Methodology

3.3.1 2D

Repeatability and multiple removal

Our first objective is to reduce the influence of acquisition differences between the 1988 and 1990 2D datasets and increase their repeatability. Processing must also balance preserving the amplitude spectrum versus reduction of noise. The 1990 data are used as a reference since the internal blowout is clearly visible here. The prestack data are first processed through a basic routine of geometry editing, trace editing and muting (that is, removal of dead channels), application of shot and receiver statics, application of a top mute to remove arrivals prior to the seabed arrival, reversible amplitude corrections to counter geometric spreading, swell noise attenuation using algorithms similar to Elboth et al. (2008) and Bekara and van der Baan (2010), velocity analysis, shot noise removal, and multiple elimination. Identical processing steps and parameters are then applied to the 1988 base vintage to guarantee repeatability. The process is then followed by coordinate regularization and re-binning on two datasets to counter feathering. Finally I perform velocity picking in preparation for stacking and AVO analysis. Only the most precarious processing steps are described in detail in the following.

Demultiple. — Given the very shallow seafloor (68 m) and the fact that the multiples blanket various 4D signatures (Figure 3.2), multiple elimination is a crucial step for both 2D datasets. Four methods were tested, namely predictive t–x deconvolution, τ–p deconvolution as described by Yilmaz (2001), surface-related multiple elimination (SRME) by Verschuur (2006), and a workflow that combines SRME and predictive deconvolution. The first two methods are widely used in case of easily recognizable multiple periodicity and clear separation between primaries and multiples. However, in this shallow water data, in addition to missing near-offset channels, multiples overlap considerably with primaries of interest. Due to these problems, demultiple performance in the t–x and τ–p domains is reduced. In addition, Radon-based demultiple filtering is not tested because velocity discrimination between reflectors is small in shal-

low sediments. SRME is tested because it does not depend on 1D subsurface assumptions nor simple multiple periodicities contrary to previous methods. This method uses wavefield extrapolation to predict multiples and adaptive subtraction to eliminate them. SRME is found to be effective in 4D deep water data (Johnston, 2013). In our case, the unmigrated shallow water dataset is also favorable for SRME because of the gentle seabed with relative small nearest offsets (79 m) and regular shot/receiver spacing. Challenges due to missing near-offset traces are solved by extrapolation in Radon domain, a regular procedure for SRME implementation (Verschuur, 2006). To cope with multiple residuals, I test a combination of SRME and predictive deconvolution. In this method, the last predictive deconvolution is applied after SRME.

Coordinate regularization. — Since the two vintages are different due to significant cable feathering, their geometrical coordinates are not identical. I amend this issue by simple trace reassignment. In particular, I performed coordinate regularization and re-binning using a carefully chosen spatial grid.

Time-lapse amplitude analysis

Traditional processing has been applied to ensure similarity between seismic vintages. However, because of variations in velocity caused by the blowout gas, seismic events at the shallow gas sandstone and below are not repeatable in terms of signal characteristics including arrival times. Therefore, further corrections must be done prior to calculating amplitude differences and subsequent time-lapse analysis. A standard processing workflow is used including amplitude calibration, phase shape, spectral shape matching and time-variant shifting (Johnston, 2013). Among them, the last step is crucial because it eliminates time shifts due to thickness and/or velocity changes in the overburden (Calvert, 2005). Other calibrations are also required to correct for non-repeatable noises created by amplitude, frequency and waveform changes between vintages (Ross et al., 1996). To quantitatively evaluate repeatability improvement, I calculate NRMS values (Kragh and Christie, 2002) between the two datasets before and after time-lapse processing. Both the local time shifts as well as the difference sections hold important information on in situ changes in material properties, e.g., due to gas movement.

Time-lapse attenuation

Time-lapse attenuation is also helpful to detect hydrocarbon activities. Changes in gas saturation and pore pressure affect not only density and velocity (Gassmann, 1951; Batzle and Wang, 1992) but also attenuation (Winkler and Nur, 1979; Klimentos and McCann, 1990; Koesoemadinata and McMechan, 2001). In other words, time-lapse changes in attenuation hold relevant information on in-situ changes in pore pressure and gas saturation. The approach I used in this thesis is based on the direct attenuation difference method introduced by Blanchard et al. (2010a) and Blanchard (2011), yet applied to poststack data for simplicity for the 2D and 3D datasets as done by Blanchard (2014).

Analytically, the frequency-dependent ratio of amplitude spectra S between two seismic datasets can be expressed as a function of attenuation differences:

$$\ln\left[\frac{S'(f)}{S(f)}\right] = -t\pi f\left(\frac{1}{Q'} - \frac{1}{Q}\right) + \ln\frac{R'}{R}, \tag{3.1}$$

where t is arrival time of the reflector, f is frequency; and Q, R are the quality factor and geometric spreading parameters in the base data. Symbols with a prime identify those for the monitor dataset.

A simple fixed-window Fourier transform is used to calculate spectra of the base and monitor data. Attenuation changes (ΔQ^{-1}) can then be derived by linear regression with respect to frequency using Equation 3.1.

Depending on the source wavelet characteristics and Q variation between seismic vintages, regression inversion is stable within a certain range of frequencies. Therefore, the operating time gate must be chosen carefully not only to cover the lowest frequency limit but also to guarantee temporal resolution properly (Reine et al., 2012b). I select this range by comparing behavior of amplitude spectra between vintages. Window length is then chosen to be sufficiently large to recover the lowest frequencies of interest.

Prestack attributes

Prestack amplitude analyses are useful for investigating fluid changes in a reservoir. Since the available well logs are recorded at well 2-4/16 after the blowout, the prestack 1990 seismic data are chosen as input to compute these attributes.

AVO and impedance inversion analysis are performed using widely accepted workflows proposed by Russell (2014) and Hampson et al. (2005), respectively. In our case, the missing S-wave log is calculated using Castagna's equation (Castagna et al., 1985) and the velocity profile is taken from our previous processing stages. Our chosen prestack output attributes include scaled vertical contrast in Poisson's ratios (defined as the sum of AVO intercept and gradient — Castagna and Smith, 1994), P-wave impedance and density. Simultaneous inversion results reduce uncertainties for interpreting geological structure that have similar impedance behavior, yielding more confidence in parameters such as obtained changes in Poisson's ratios, indicative of fluid effects.

3.3.2 3D

Repeatability and coordinate regularization

For the 3D data only the migrated volumes are available. Significant repeatability issues exist due to considerable differences in acquisition geometries and processing routines. CDP re-binning is done to reduce dissimilarities to obtain two datasets with identical geometry, in terms of direction, number of inlines and crosslines and CDP numbering. In addition, the time range and sample rate is equalized and a bulk time shift is applied to eliminate a mis-tie. The two seismic vintages are demultipled, therefore there is no need to perform this processing step again.

Time-lapse processing and analysis

No prestack attributes are computed for this dataset as only poststack volumes are available. Likewise, repeatability issues prevent the analysis of time-lapse instantaneous amplitude differences. In fact, only time shifts and time-lapse attenuation are used to investigate gas migration between both 3D vintages.

In order to assess attribute variability, I picked the two sandstones at 520 and 900 ms and three other horizons between these two. These additional horizons are used to investigate attribute changes with depth and along stratigraphic layers. Due to data quality, the shallow sandstone is interpreted only for a small area of 13.5 km^2 around the well location.

I estimate preliminary time-shifts using cross-correlation between the two seismic datasets similarly as in the 2D case. This attribute is then compared with time-lapse attenuation differences. Since the amplitude differences are not calculated, I do not perform amplitude calibration and phase matching.

Time-lapse attenuation is computed similarly to the 2D case. However, since the acquisition settings are different from the 2D datasets, I perform another spectral comparison between vintages for parameterization instead of using same frequency regression range as in the 2D case. The operating time gate is then reselected based on the new frequency range. I extract the time-lapse changes in attenuation along the two interpreted sandstones.

The data re-binning and acquisition footprints may influence computed time-lapse attenuation differences. In addition, shallow structures may leave imprints on deeper results. These potential shallow structures are detected from trace-by-trace cross-correlation coefficients between stacked seismic traces at a shallow time interval less than 400 ms. In order to reduce uncertainties for deep events, the following steps were applied: (1) calculating attenuation changes at three horizons below the deep sandstone, separately by constant time intervals; (2) vertically averaging these three maps and (3) subtracting the averaged map from the estimated attenuation changes for the deep sandstone.

The major source for the underground blowout into the sandstone formation is through the exit behind the 20" casing at approximately 900 m depth. Therefore I assume no attenuation changes below this point. Steps 1 and 2 are thus used to eliminate nonphysical attenuation changes due to noise created by acquisition footprints and shallow structures. Artifact removal step is important in the workflow because it not only cancels out shallow artifacts but also smooths the final result for quality improvement.

3.4 Results

3.4.1 2D

Repeatability and multiple removal

Figure 3.3 compares different demultiple methods performed on the 1990 dataset. Figure 3.3a displays raw stacked data after a basic processing routine, including trace editing, AGC, frequency filtering, velocity analysis and NMO correction. Parameterizations are chosen for visually best outcomes. Figures 3.3b–d show stacked sections after demultiple application using predictive deconvolution in t–x and τ–p domains and SRME, respectively.

In the predictive deconvolution approach (Figures 3.3b,c), the second-order multiples of the seabed, the shallow sandstone and a primary at 650 ms are removed. In general, these two methods seem to be more effective in the deeper part of the section as part of the 650 ms event's first multiple is attenuated as well. In the shallower part, t–x domain deconvolution is more effective than τ–p domain deconvolution since the first-order multiple of the seabed is more attenuated. The fact that τ–p domain deconvolution is limited may be due to limitations imposed by the τ–p transformation since only a few traces contain useful reflection and multiple information for shallow reflectors before they are contaminated by direct waves. Both methods also attenuate other primaries, e.g., the one at 350 ms. Based on these observations, it is found that single-pass predictive deconvolution, in either domain, does not succeed in removing multiples in shallow water areas properly. This issue is the result of missing near offset receivers and the fact that shallow water bottom multiples significantly interfere with primaries.

The SRME demultiple result (Figure 3.3d) is significantly better than the two previous methods. All multiples of the shallow seabed and the deeper 650 ms event are adequately removed while the primary at 350 ms is still preserved. This method also attenuates most energy of the shallow sandstone first order multiple at 610 ms. A small residual of this event may still be present. It is possible that judicious optimization of the adaptive subtraction parameters would fully remove this residual multiple event.

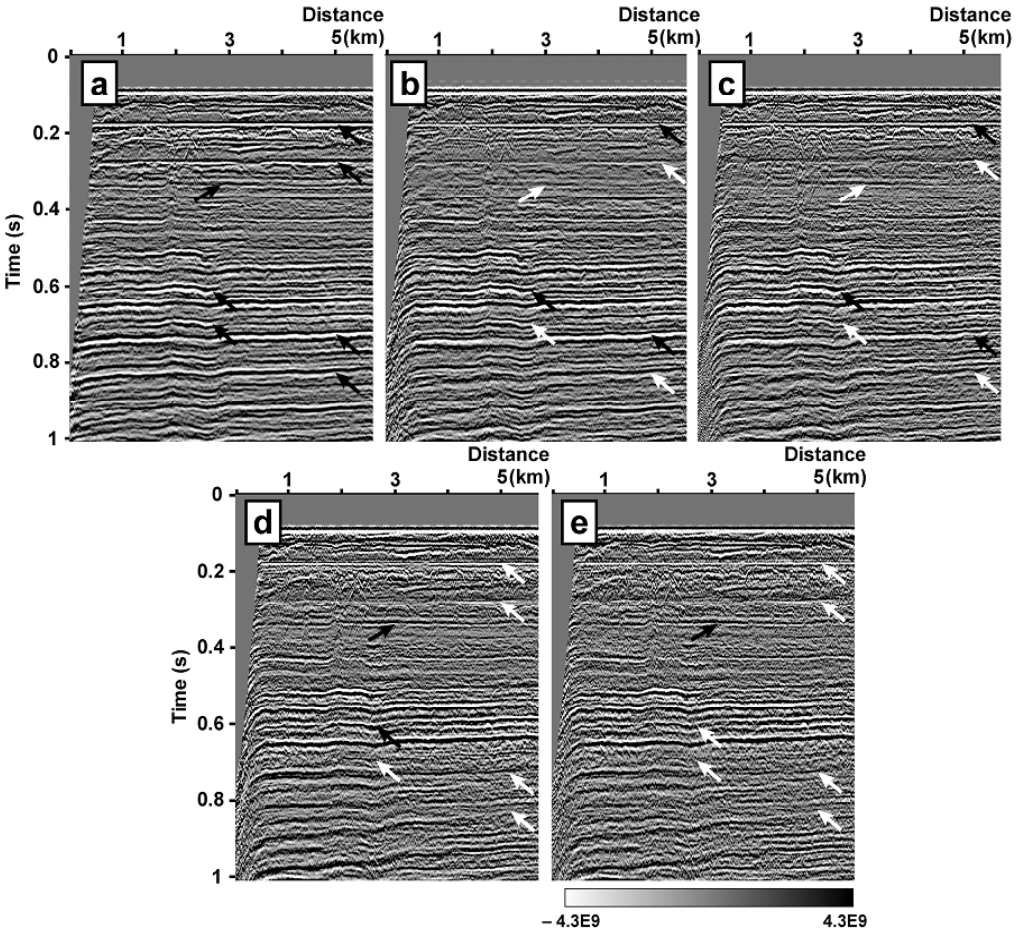

Figure 3.3: Demultiple results for 1990 2D data. Black arrows, events of interest; white arrows, removed events. (a) Brute stack with multiples (left-pointed black arrows). Predictive deconvolution performed in the (b) t–x and (c) τ–p domains leaves first-order multiples. The primary at 350 ms (right-pointed black arrow) is also attenuated in these deconvolution methods. (d) The SRME demultiple result removes most multiples and preserves the 350 ms primary better. (e) A combination of SRME followed by t–x domain deconvolution leads to an even better result. Data are displayed in normal SEG polarity standard after processing.

To improve the SRME demultiple quality, I subsequently applied t–x domain predictive deconvolution on this dataset because it performs better than its τ–p domain variant as seen in the previous tests. The final result is shown in Figure 3.3e. This combination provides superior results to the other demultiple workflows with all multiples of the seabed, shallow sandstone at 520 ms and primary at 650 ms attenuated. In addition, all primaries of interest are retained. Predictive deconvolution performed after SRME benefits from the extrapolated near-offset traces recovered in the SRME workflow.

In this case study, SRME is found to be the key demultiple solution for these legacy 4D shallow water data where strong multiples are present and missing near traces prevent predictive deconvolution to work effectively. SRME is effective in this North Sea area because of the simple seabed topography and regular acquisition spacing.

In the geometry re-assignment step, I manually pick common CDP positions in the middle of two feathering lines and define rectangular CDP bins of 50 $\times$ 6.25 m. The chosen width of 50 m is sufficiently wide to include adequate midpoints throughout the survey. After this step, both seismic vintages share identical geometry information with common CDP numbering.

Time-lapse processing and amplitude differences

Time-shifts between seismic vintages are then calculated with a maximum allowed difference of $\pm$15 ms (Figure 3.4c). Time shifts are close to zero outside of the blowout gas areas, vary up to 3.1 ms for top of the shallow sandstone (at 520 ms) and increase up to 10 ms below this sandstone (at 700 ms). This implies a velocity drop due to accumulated gas in the shallow sandstone during the blowout. However, no time-shifts are detected for the deep sandstone at 880 ms.

I then apply phase-shift and wavelet shape matching operators with maximum correlation shift of 10 ms and a similarity threshold of 65%, respectively. This threshold must be chosen judiciously to obtain sufficient corrections as well as to maintain original signal characteristics (Lumley et al., 2003). These parameters ensure good alignment of coherent features without visual artefact creation (e.g., due to overcorrection).

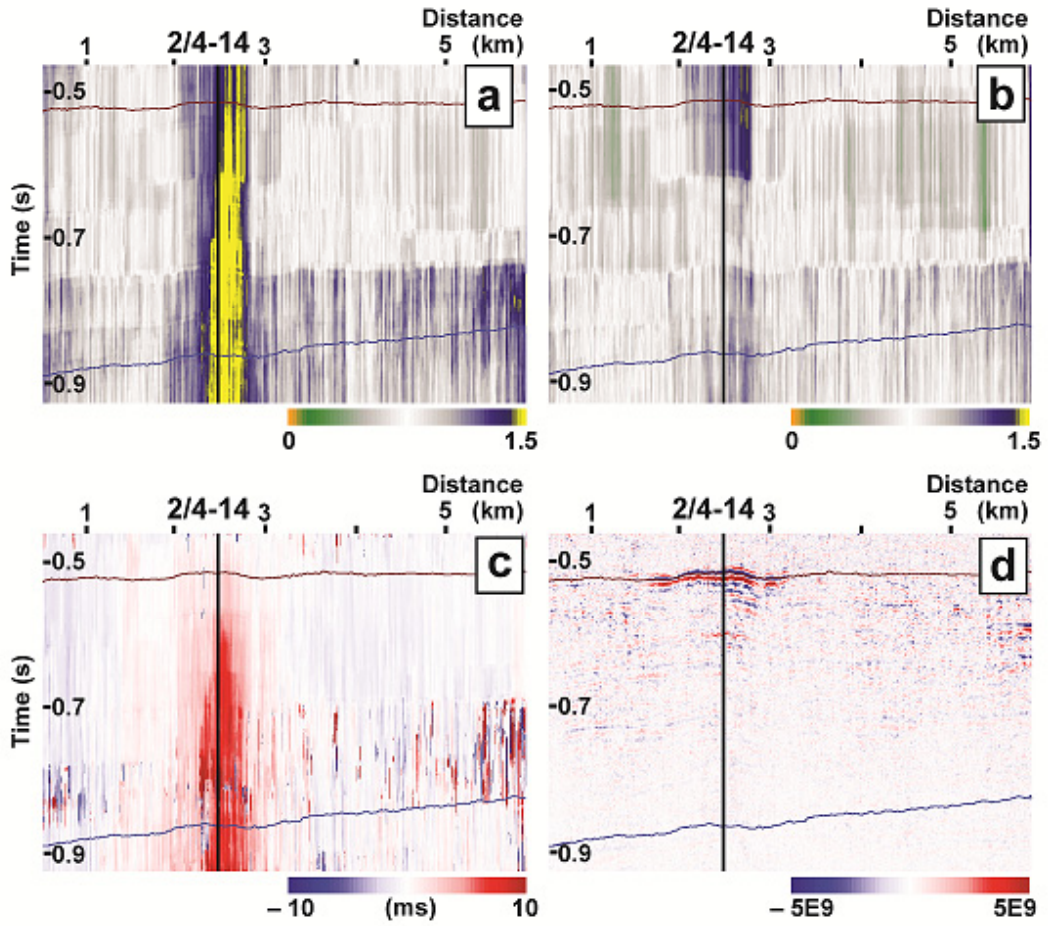

Figure 3.4: The 2D time-lapse attributes and repeatability. Comparison between NRMS sections computed (a) before and (b) after time-lapse processing shows repeatability has been improved. (c) Time shifts show velocity drop below the shallow sandstone layer. (d) Amplitude differences, indicating new gas accumulation within the shallow sandstone. Vertical black line: projection of the blowout well. Horizontal brown line: shallow sandstone layer; dipping blue line: deep sandstone layer.

To evaluate the repeatability improvement, I compute NRMS values between vintages before and after time-lapse processing. The charged gas into the shallow sandstone layer does not only reduce velocity, as observed by the time-shifts (Figure 3.4c), but also reduces signal similarity. Low repeatability zones are expressed by NRMS values larger than 1.5, such as at the 520 ms shallow sandstone interval around the blowout well (Figure 3.4a). The time-lapse processing significantly improves repeatability, correcting for most non-physical differences due to different acquisition parameters (Figure 3.4b).

The resulting amplitude difference section (Figure 3.4d) shows a noticeable negative change at 520 ms that extends for 1.5 km around the blowout well. This amplitude decrease suggests a decrease in P-impedance at the top of this interval due to gas inflow. This anomaly is dome shaped and corresponds to the location of the shallow sandstone, indicating new gas accumulation from 1988 to 1990. On the other hand, no significant amplitude change is observed for the deep sandstone layer at 880 ms.

Time-lapse attenuation

Examination of amplitude spectra before and after the blowout is used to determine feasibility of estimating time-lapse attenuation. Spectra for each vintage are computed using a fixed-window Fourier transform, over a 100 ms interval at and above the shallow sandstone horizon around the blowout well. Spectral comparison shows similar features above the sandstone layer before and after the blowout (Figure 3.5a). A dominant notch at 60 Hz might be due to the source and receiver ghost. Within the sandstone layer, there is an overall shift to lower frequencies in the spectra (Figure 3.5b). The most significant frequency shift is observed at the second dominant peak. It is reduced from 75 Hz to 70 Hz. The 60 Hz notch is shifted closer to 50 Hz. This suggests spectral attenuation due to the accumulation of gas in the shallow sandstone after the blowout.

Next, time-lapse attenuation is estimated for the 2D lines using Equation 3.1 within the frequency range from 20 Hz to 120 Hz (Figure 3.6). An attenuation increase is observed within the shallow sandstone at 520 ms around the blowout well. The attenuation anomaly has a slightly domal structure, similar to the

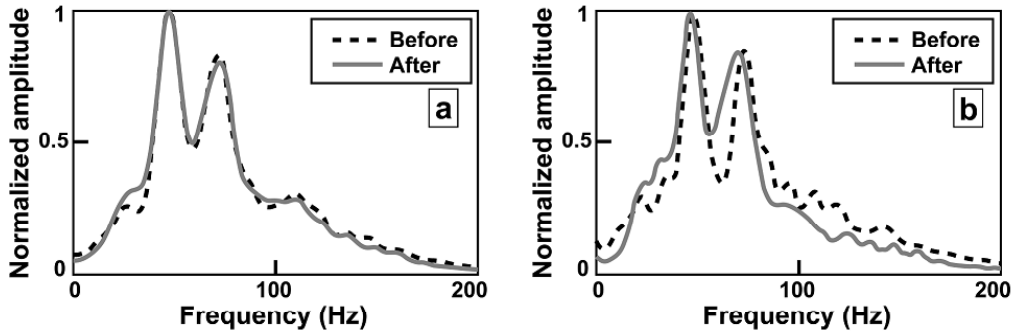

Figure 3.5: Amplitude spectra (a) above and (b) inside the shallow sandstone layer for 1988 (dashed black line) and 1990 (solid gray line) data sets. Reduced frequency content greater than 50 Hz suggests gas accumulation after the blowout within the shallow sandstone layer.

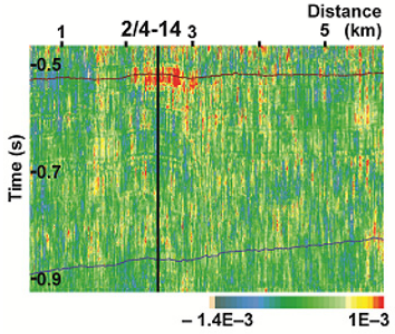

Figure 3.6: Attenuation increase (ΔQ^{-1}) at the shallow sandstone (hot colors) indicates new gas accumulation between 1988 and 1990. Vertical black line: projection of the blowout well. Horizontal brown line: shallow sandstone layer; dipping blue line: deep sandstone layer.

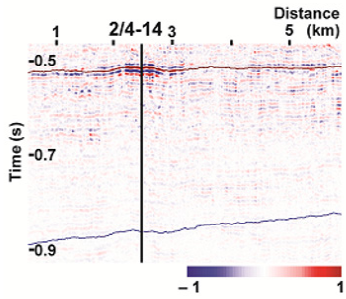

Figure 3.7: Scaled vertical Poisson's ratio for the 1990 data. Increased contrast near the shallow sandstone indicates gas accumulation. Vertical black line: projection of the blowout well. Horizontal brown line: shallow sandstone layer; dipping blue line: deep sandstone layer.

amplitude difference section (Figure 3.4d), but with a smaller lateral extent of about 1.1 km and centered somewhat more to the northeast of the well. The attenuation increase indicates an increase in absorbed seismic energy due to the presence of more gas after the blowout. No noticeable attenuation change is observed for the deep sandstone.

Prestack attributes: AVO and inversion

I perform AVO analysis after offset-to-angle conversion on the prestack 1990 monitor data using picked velocities from the processing stage. From intercept and gradient examinations, the shallow sandstone appears as a class 4 AVO anomaly with decreasing negative amplitudes with offset. Figure 3.7 shows the scaled vertical Poisson's ratio. It provides in this case superior detection results compared to the product of intercept and gradient (not shown). The shallow sandstone layer is represented as an 830 m long feature at 520 ms with higher Poisson's ratios than in the surrounding area. For the deeper sandstone layer, there is no significant AVO response.

Prestack inversion results show low densities and P-wave impedances at the shallow sandstone interval (Figures 3.8a,b). This is expected from the amplitude differences (Figure 3.4d) and class 4 AVO intercept. This zone appears as a feature at 520 ms and extends for 1.16 km on the P-impedance section and for 1.23 km on the density section. The anomalies also show lower P-impedance and density at the northeast side of the well. This feature agrees with both the

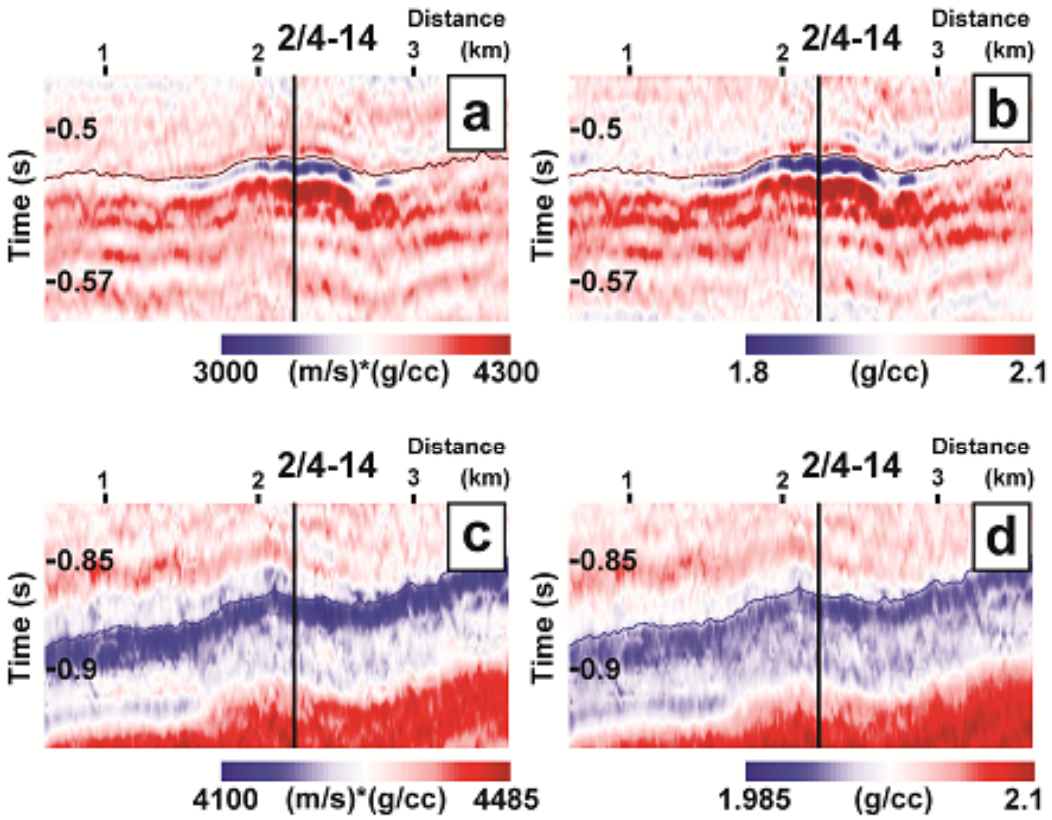

Figure 3.8: Prestack inversion results for 1990 data. Left column: P-wave impedance; right column: density. Top row: Shallow sandstone; bottom row: deep sandstone. Low P-wave impedance and density are observed at the shallow sandstone (a and b, respectively) and the deep sandstone (c and d, respectively). Vertical black line: projection of the blowout well. Horizontal brown line: shallow sandstone layer; dipping blue line: deep sandstone layer.

computed time shifts (Figure 3.4c) and time-lapse attenuation (Figure 3.6). It is another confirmation of gas charged into the shallow sandstone.

Along the deeper sandstone body, low densities and P-wave impedances are observed in a 60 ms interval, with lowest values at the top of the interval (Figure 3.8c,d). In this Southwest dipping layer, a moderate push down effect is observed at the projection of the well 2-4/14 location in the 1990 data (for example at the 750 ms event in Figure 3.2, dashed square). As the push down extent agrees with that of the shallow sandstone layer, it confirms again reduced velocities due to the gas charged into this shallow formation.

Different 2D attributes show that the imprint of charged gas into the shallow

sandstone is clearly seen. There is much less evidence for gas moving into the deeper layer despite best efforts above to enhance repeatability and data quality; yet this was inferred from other 2D lines (Remen, 1991). The described processing strategies for the subsequent 1991 and 2005 3D datasets however provide more insight of gas movement into both sandstone layers.

3.4.2 3D

Repeatability and coordinate regularization

In order to obtain identical geometries, the 1991 base dataset is re-gridded to the 2005 monitor dataset, because the earlier dataset contains the smaller 2005 acquisition (Figure 3.1). Final bin size is chosen to maintain output 3D inline/crossline spacing of 12.5 $\times$ 12.5 m. In addition, the monitor data are shifted by 16 ms and truncated at 2 second to match the base data in the time domain. After these calibrations, the shallow and deep sandstone layers are located at 540 and 940 ms at the exact blowout well location, respectively.

Time lapse processing and analysis

Repeatability issues prevent the analysis of time-lapse instantaneous amplitude differences. Only time shifts and time-lapse attenuation are computed since only the post-migration volumes are available.

Time and RMS amplitude horizon maps show that the shallow sandstone layer is almost horizontal and has a strong amplitude anomaly near the blowout well (Figures 3.9a,b). The deep sandstone is a south-west dipping formation (Figure 3.9c). In the corresponding amplitude map (Figure 3.9d), there is a slight amplitude anomaly surrounding the blowout well on the deep sandstone, which has less areal extent than that seen on the shallow sandstone. Furthermore there is very faint amplitude anomaly trend from the northwest to southeast that is consistent with the time structure map in Figure 3.9c.

Figure 3.10 shows the calculated time shifts at the shallow and deep sandstone layers. Both maps are contaminated by north–south/northeast–southwest noise which may be remnant acquisition footprint differences unresolved by data regridding. No clear systematic features are visible for the shallow sandstone

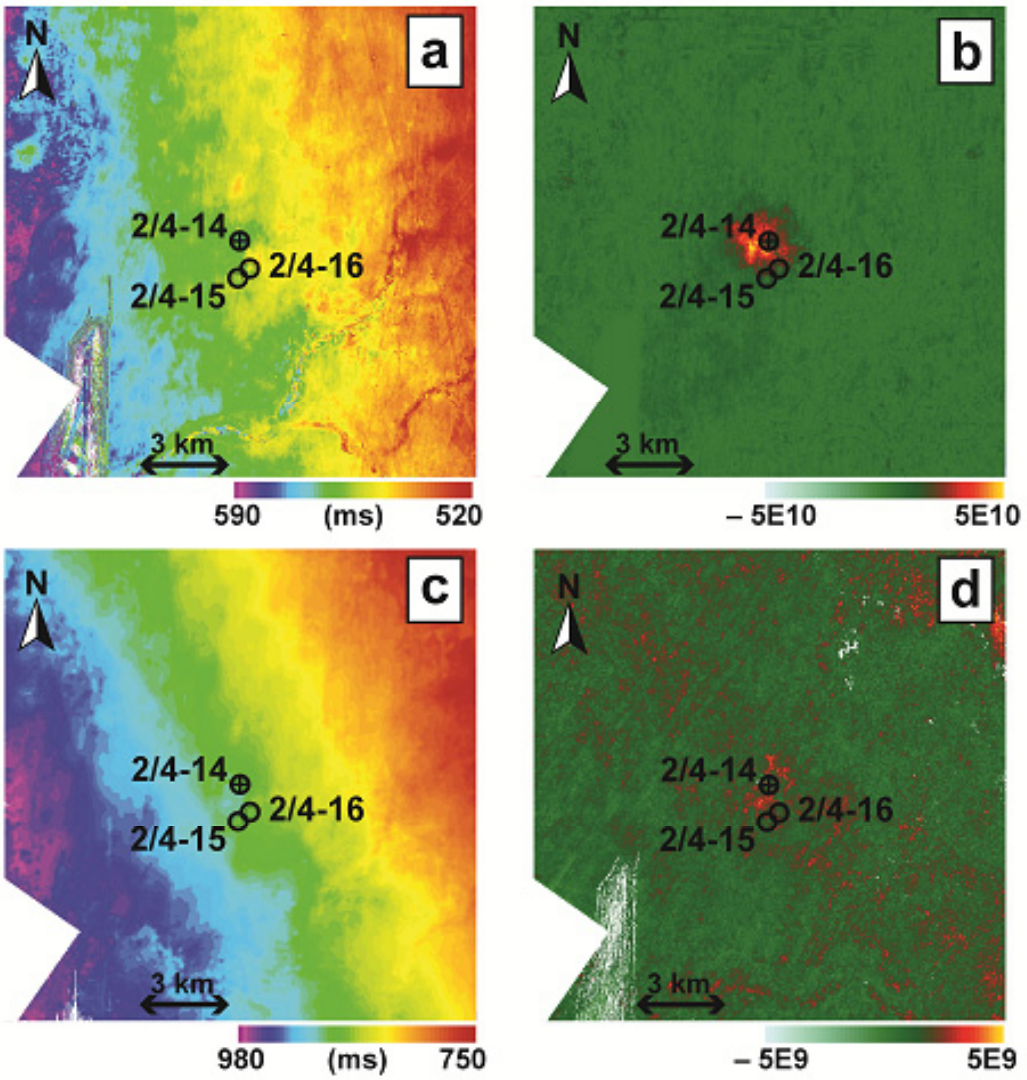

Figure 3.9: (Left) Time and (right) rms amplitude horizon maps for the 2005 3D data set show the flat shallow sandstone with (a and b) high-amplitude anomaly and (c and d) the inclined deep sandstone with small amplitude variation. Locations of the wells are marked by crossed circle (blowout well 2/4-14) and regular circles (relief well 2/4-15 and control well 2/4-16).

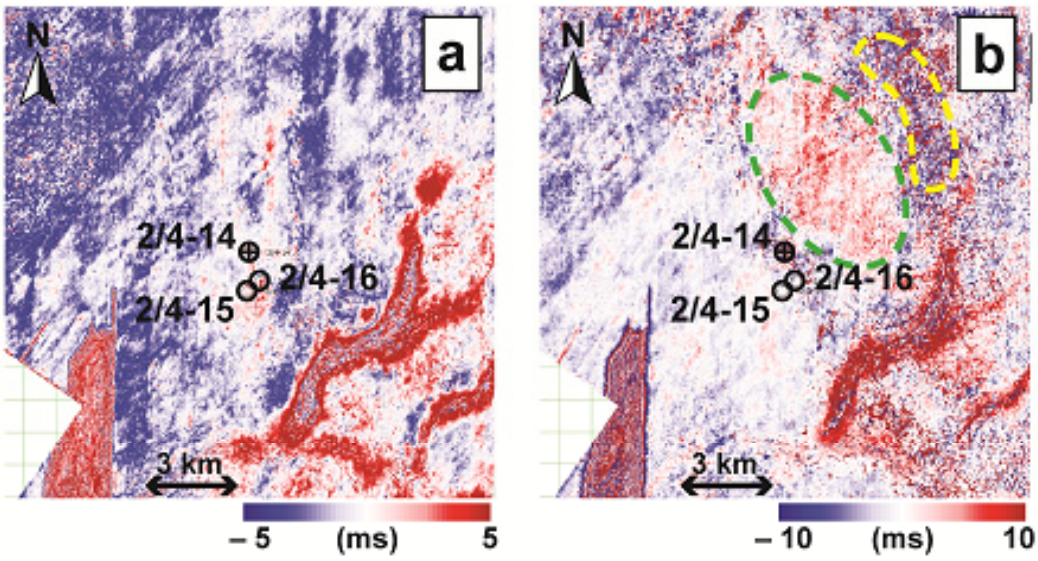

Figure 3.10: Time shifts for the (a) shallow and (b) deep sandstone layers. The dashed outlines indicate the time-shift anomaly zones (green, increase; yellow, decrease). Locations of the wells are marked by the crossed circle (blowout well 2/4-14) and regular circles (relief well 2/4-15 and control well 2/4-16).

(Figure 3.10a). On the other hand, the deep sandstone shows a positive time shift anomaly northeast of the blowout well, resembling a northwest to southeast elongated ellipse of 6.5 km long and 3.5 km wide (Figure 3.10b, green ellipse). Further to the northeast, this anomaly is followed by a zone of negative time-shifts which is 5.5 km long and 1.2 km wide (yellow ellipse). These anomalies suggest an 11 km^2 reduced velocity zone at the well and a 6.5 km^2 increased velocity zone further northeast.

There is also a significant positive anomaly located in the southeast corner of the area. An edge detection variance attribute (Chen and Sydney, 1997) calculated at 360 ms (Figure 3.11) suggests this feature is a remnant artefact from a shallow tunnel valley system that has been investigated by Haavik and Landrø (2014). Such shallow geologic features may introduce imprints (artifacts) on other attributes at larger depth. Finally, the blocky noisy area in the southwest area of Figure 3.10b and 3.11 is introduced by missing data. It is excluded from further examination.

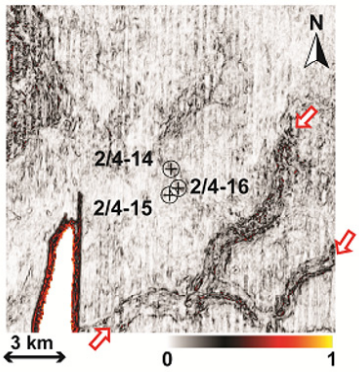

Figure 3.11: Shallow tunnel valley (red arrows) detected by a variance attribute at 360 ms for 2005 data set. The locations of the wells are marked by crossed circles.

Time-lapse attenuation

I repeat the comparison in amplitude spectra for the 3D datasets for the shallow sandstone between the 1991 base and 2005 monitor data to evaluate feasibility of estimating 4D attenuation changes (Figure 3.12). Both amplitude spectra above the sandstone are similar for 1991 and 2005. However, subtle changes occur within the shallow sandstone layer. The 1991 main frequency peak at 35 Hz is slightly reduced to 30 Hz, and some energy has decreased (e.g., at 25 Hz and 60 Hz). Such irregular/complex changes may be caused by the different acquisition geometries and/or processing strategies to obtain the dataset or they could indicate intricate gas migration behaviors. This is investigated via a time-lapse attenuation analysis.

Time-lapse attenuation estimation is done within the frequency range from 15 to 80 Hz using an operator window length of 80 ms to cover at least one period of the lowest 25 Hz peak in the test spectra above. For the deeper sandstone, shallow tunnel valley imprints are removed using the 3-step noise averaging technique described earlier using 3 horizons below this sandstone. Attenuation changes at the shallow and deep sandstone layers are shown in Figure 3.13.

For the shallow sandstone, the extracted 4D attenuation map is contaminated with speckle noise due to low repeatability but provides more notable details compared to the time-shift result (Figure 3.10a). Attenuation is reduced

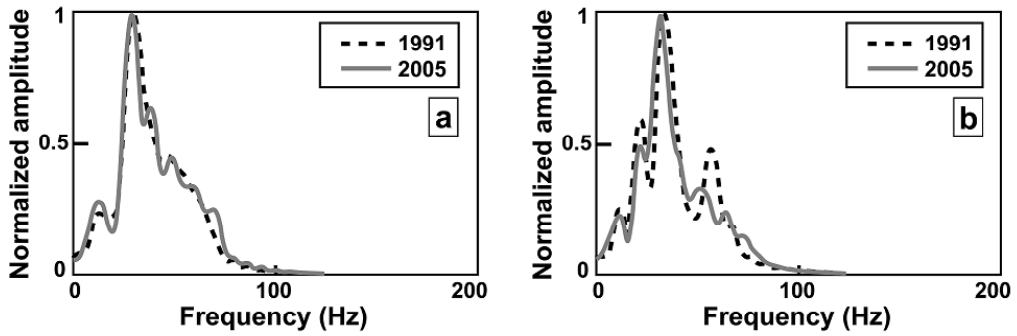

Figure 3.12: Amplitude spectra (a) outside and (b) inside the shallow sandstone layer for both 3D data sets. Varying frequency content suggests further gas movement between 1991 (dashed black line) and 2005 (solid gray line).

at the blowout well 2-4/14. This zone radially extends 1.2 km to the well 2/4-16 (dashed circle). This decreased attenuation zone is encircled by a 200 m wide positive anomaly of increased attenuation reaching the relief well 2/4-15 (solid circle). The radially symmetric anomalies imply that gas has spread to 6.2 km^2 between 1991 and 2005 and extends beyond the 800 m anomaly observed between 1988 and 1990 in the 2D data (Figure 3.6). However, gas flow has significantly slowed down from 1991 to 2005 compared with the time lapse changes seen in the first year after of the blowout.

For the deep sandstone layer, the time-lapse attenuation attribute shows similar features to the time-shifts (Figure 3.10b) but possibly with less noise contamination (Figure 3.13b) now that the southeastern tunnel valley effect has been removed. A strong positive anomaly is visible northeast of the blowout well (red dashed curve), coinciding with the area of positive time shifts. It is followed by a reduction in attenuation at the position of the negative time shifts further to the northeast (blue dashed curve).

Both anomalies are elongated in the northwest southeast direction. The first zone of attenuation increase has an elliptical shape with a length of 6.6 km and width of 2 km, yielding an area of 13.25 km^2. It occurs 250 m away from the well 2-4/14. The second zone of attenuation decrease occurs 5.36 km away from the blowout well and is 2.5 km wide. The reduction in attenuation also occurs in an arc surrounding the positive attenuation anomaly (blue dashed area). Such an arc is not visible in the time shift map except possibly its

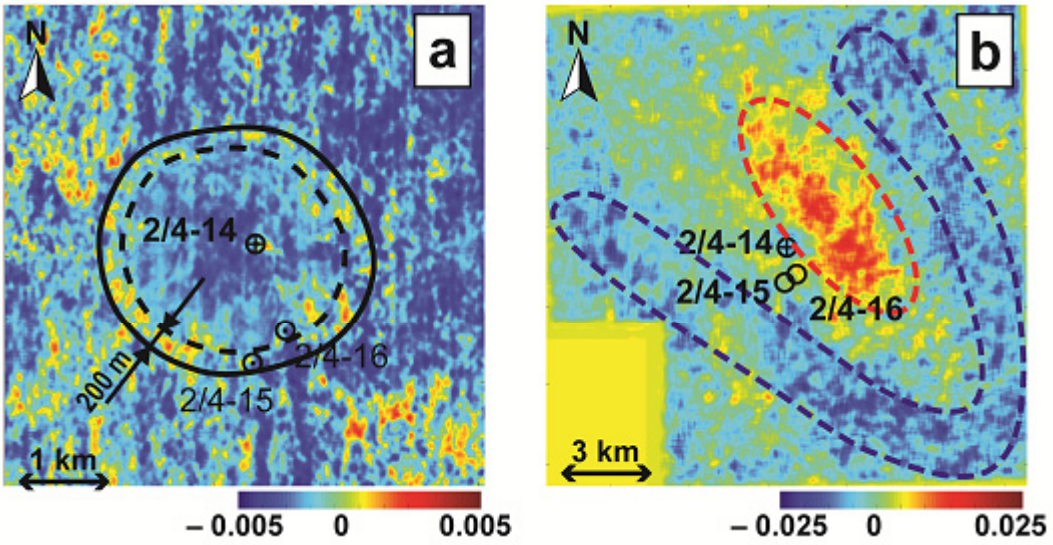

Figure 3.13: The 4D attenuation changes between 1991 and 2005 observed at (a) the shallow sandstone layer (two circles, zone of horizontal gas expansion) and (b) the deep sandstone layers (dashed red and blue outlines, zones of increased and decreased attenuation, respectively). The locations of the wells are marked by the crossed circle (blowout well 2/4-14) and regular circles (relief well 2/4-15 and control well 2/4-16).

northeastern portion (Figure 3.10b, yellow dashes), indicating the attenuation map provides more information.

The lateral expansion of gas migration is more visible in both sandstone layers in the 3D data. The 4D attenuation features suggest that the blowout gas has simply spread out horizontally within the shallow sandstone; yet it may have migrated up dip to the northeast within the dipping deep sandstone, causing a more complex zone of attenuation variations in this area, due to combined pore pressure and gas saturation changes (Dinh et al., 2015).

3.5 Discussion

The underground gas blowout has been studied by various authors, yet its interpretation still faces substantial challenges and uncertainty mainly due to the data quality (Lie and Larsen, 1991; Landrø, 2011). The various sets of legacy data are plagued by poor repeatability between data acquisitions, application of different processing strategies, missing prestack data and the presence of

multiples. This severely prevents quantitative interpretation and limits interpretation confidence. This thesis shows that (1) careful 4D processing may provide useful information even from legacy data but also that (2) judicious quality control and comparison of various attributes is highly important to get consistent results. I will discuss the SRME and time-lapse attenuation techniques in detail first. Then I focus on the implemented quality control strategies to determine which attributes show the most reliable and conforming features.

Various multiples overlap with the subtle primary reflections of interest. In this case, there is a simple seabed topography and regular acquisition spacing, yet near-offset traces are missing. It is likely that several factors contribute to the superiority of SRME over predictive deconvolution and Radon demultiple as a first step. SRME predicts the multiples from the data by iterative convolution, rather than assuming a simple structure (Verschuur, 2006). Therefore, it is less affected by small velocity differences between multiples and primaries. However, SRME does not attenuate far offset multiples well because of its limitation at high incident angles (Hugonnet and Lecocq, 2003; Dragoset et al., 2010). Thus, Radon demultiple or τ–p deconvolution is generally applied as well. In our case this does not lead to favorable results because of a variety of reasons including (1) the very shallow water, (2) small differences between primaries and multiples velocities and (3) artifacts introduced during domain transforms. Instead, I use additionally regular predictive deconvolution because of both cost and simplicity.

SRME includes a trace reconstruction step in the Radon domain, which helps reduce the edge effect of the missing near-offset traces. To account for possible complex subsurface structures that might move the reflection point to the other side of the source, data are extrapolated beyond zero offset. In this step, the number of traces used to model the split spread is crucial for good SRME results. It must be chosen such that there are on the one hand sufficient traces to obtain a clear signal in the Radon domain but on the other hand not too many to avoid uncertainties at high incident angles. Trial-and-error tests show between 10 to 12 traces works best in our case.

An associated parameter is the maximum interpolation slowness. It is chosen according to maximum moveout of interest in the reconstructed near-offset

traces. A value of ±30 ms works well for this dataset.

Another key parameter for SRME is the number of convolution iterations used when predicting multiples from the data. Amplitude predictions in the first iteration are generally incorrect because of source wavelet distortion during propagation (Dragoset et al., 2010). Therefore, it requires more convolution iterations and thus more input traces to estimate the multiples correctly. In this dataset, tests show that using as many traces as offset up to 1,000 m provides best result (more traces do not improve result).

A final advantage of SRME is that it employs a separate subtraction step which aids in balancing the amount of removed multiple energy even when multiples overlap with subtle primary signals. Fortunately, because of the simple seabed tomography, 2D SRME is sufficient to predict the multiples from the single 2D streamer lines. The adaptive subtraction step thus becomes less important to remove timing errors.

The additional predictive deconvolution step benefited from the data reconstruction step in SRME. The most important parameter is the deconvolution operator length, chosen to equal the observed periodicity of the multiples, which is 90 ms in this case.

The time-lapse attenuation measurements play a key role in detecting changes in gas migration in all 2D and 3D datasets. The time-lapse ΔQ values are estimated from poststack seismic data using the using spectral ratio method. Contrary to time-lapse amplitude analysis, this attribute does not require scalar energy calibration between seismic vintages because the amplitude difference only influences the intercept of the logarithm of spectra ratios. Application on poststack data has the benefit that results are more stable. However, only qualitative analysis is possible (that is, trends in values) since only prestack Q estimation can produce unbiased estimates.

Spectral ratio methods require careful choice of the frequency range used in the regressions. This range is chosen to emphasize stable regions (Reine et al., 2009; Reine et al., 2012b). For example Figure 3.14 shows no change in spectra above the sandstone layer (flat response in spectral ratios) but attenuation changes within the shallow sandstone in the 2D data (dipping trend in the log spectral ratios). Frequencies are then chosen in the stable bandwidth, excluding

notches and poles, preferably representing more than 25% of the total signal energy. In this case, frequency ranges from 20 to 120 Hz for the 2D data, and 15–80 Hz for the 3D data are found to yield stable regression results.

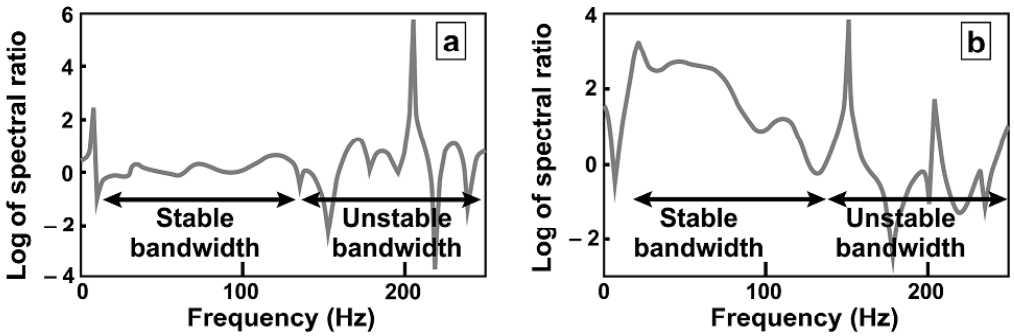

Figure 3.14: Examples of the logarithm of the spectral ratio used for time-lapse Q parameterization for the 2D data, measured (a) above and (b) inside the shallow sandstone.

The analysis window length is another important parameter. It must be chosen large enough to include at least one or two of the longest periods of interest (that is, lowest frequencies of interest). Simultaneously, a long length is avoided to prevent poor vertical resolution of the output. For example, with frequency ranges used in the 2D and 3D datasets, minimum operator lengths are 50 ms and 66 ms, respectively. Numerous parameter tests showed that a window length of 100 ms and 80 ms provides stable results for the 2D and 3D data, respectively.

Reine et al. (2009) and Reine et al. (2012b) recommend the use of variable-window time-frequency transforms for attenuation analysis such that a long time window is used to analyze the low frequencies and a short one for the higher frequencies. This provides an enhanced time-frequency resolution over the use of fixed-window transforms such as the short-time Fourier transform (Tary et al., 2014), for instance by ensuring that contamination from adjacent reflections is minimized. I do not anticipate large changes in the detected qualitative time-lapse Q features if a variable-window time-frequency transform is used since the emphasis in this thesis is on detection of time-lapse changes instead of resolving the exact quantitative differences.

In this study, much emphasis is placed on quality control of derived at-

tributes. This is achieved by computing various attributes for both the 2D and 3D time-lapse datasets and then comparing both their supporting and conflicting features. The shallow sandstone is expressed by an 800–1,000 m wide domal structure with low impedance and density in the 1990 2D data (Figures 3.7a,b). Differences between 1988 and 1990 have been observed with positive changes in arrival time and attenuation and negative changes in amplitude (Figures 3.4c,d and 3.6). These observations consistently suggest presence of gas at this interval due to the subsurface blowout. The reprocessed data provide better images than previous works (Landrø, 2011) with multiples and strong artefacts removed; yet this feature has been consistently noticed in all previous work as well.

The operator used multiple temperature and noise logs as well as a camera to unravel a complex pattern in the subsurface blowout with various types of casing failing at different time, resulting in changing underground flow paths for the gas (Remen, 1991; Landrø, 2011; Langseth and Landrø, 2012). The main escape point into the surrounding formations is thought to have been at the bottom of the 20" surface casing at 900 m, rendering the 828 m sandstone the most likely recipient formation (Remen, 1991). Examination of different 2D amplitude sections for all sail lines by Lie and Larsen (1991) confirms gas accumulation in the northeast area after the blowout. Langseth and Landrø (2012) observe subtle time shifts and amplitude changes after the blowout in this sandstone based on analysis of the raw 2D data. Using the reprocessed 2D data, time shifts, time-lapse amplitudes and attenuation show weak evidence of a gas anomaly in the deep sandstone (Figures 3.4 and 3.6), but prestack inversion results do give some indication (Figures 3.8c,d). Unfortunately the lack of well log data beyond gamma rays in the regions of interest complicates the impedance inversions. Although the 2D data are carefully processed, the non-repeated acquisition geometries may have led to lower quality and thus poorer resolution with increasing depth. On the other hand, the shallow sandstone is around 3–10 m thick, whereas the deeper sandstone has a thickness of up to 60–80 m (Remen, 1991; Lie and Larsen, 1991). Thus, despite closeness to the inferred point of casing failure, the greater thickness of the deeper sandstone may have rendered time-lapse changes harder to see.

In a later time frame, for the 3D datasets acquired in 1991 and 2005, an amplitude and time-lapse attenuation anomaly is observed again for the shallow sandstone (Figure 3.9b and 3.13a) but time-shift results are less clear (Figure 3.10a). In a similar time frame between 1990 and 2009, Landrø (2011) finds both time shifts and amplitude changes (2D) in this sandstone, again confirming clear changes in the shallow sandstone due to gas migration.

For the deep sandstone layer, Landrø, 2011 finds no major changes in time-shift (2D) between 1990 and 2009. Langseth and Landrø (2012) observe only a faint amplitude anomaly in the 1991 3D dataset. In the current study, evidence for gas migration within the deeper sandstone between 1991 and 2005 is better visible in both the time-shift and time-lapse attenuation results (Figures 3.10b and 3.13b) but less so in the 2005 amplitude map (Figure 3.9d). I find that this is in qualitative agreement with Lie and Larsen (1991) in the sense that I observe anomalies to the northeast of the well location. Although our results are obtained for a later time interval (1991–2005) and from 3D data instead of multiple 2D sail lines, these combined observations may be supportive to study long term gas migration pattern in this sandstone layer.

To briefly summarize, the reprocessed results for the 2D and 3D datasets confirm much gas spread radially around the blow-out well into the flat shallow sandstone after the blowout (Figures 3.2, 3.4, 3.6–3.8, 3.10, 3.13). The diminishing spread rate in both the time-lapse amplitude and attenuation changes (Figures 3.2, 3.9b, 3.13a) suggests gas migrated quickly at first (from 1989 to 1990) and then slowed down over time (from 1991 to 2005). I attribute the changing flow rates both to the cessation of incoming gas and the effect of the horizontal layering, preventing movement due to buoyancy effects. These results are corroborated by 2D reservoir simulation results by Langseth and Landrø (2012) who observe that from August 1989 to October 1990 there is an increase of pore pressure and gas saturation around the well at different distances. This implies concentric anomalies after the blowout.

For the deeper sandstone, gas migration is less clear. In this thesis, the 3D time shifts and time-lapse attenuation maps (Figures 3.10b and 3.13b) indicate gas migrated up dip between 1991 and 2005. These observations are consistent with gas accumulation before 1991 (Lie and Larsen, 1991) and imply that the

dipping structure has facilitated migration away from the blowout well due to gas buoyancy. The 2D reservoir simulation results for 1989 and 1990 by Langseth and Landrø (2012), assuming horizontal stratigraphies, show a slight decrease in gas saturation close to the well position and a similar increase for distances larger than 3–4 km on both directions from the well. This predicts donut-shaped anomalies for gas saturation changes. This is indeed observed for the shallow gas layer in a later time frame (Figure 3.13a). Since the deep sandstone layer is dipping towards south-west, it is reasonable to assume that this anomaly might be distorted and shifted towards the up dip direction as interpreted in Figure 3.13b. In order to understand more accurately how gas distribution changes in this sandstone layer, a 3D reservoir simulation including a deeper tilted sandstone layer should be considered to allow for gravity-dominated flow. A more in-depth analysis including estimation of quantitative changes in pore pressure and saturation is planned in a follow-up paper.

3.6 Conclusion

Our results show that not all attributes may reveal consistent subsurface changes, especially in case of legacy data which often have acquisition and processing challenges. All attributes are sensitive to 4D repeatability, yet often in different fashions. For instance, time-lapse amplitude changes are often investigated as a first telltale signature. Yet even if there are no amplitude differences then this does not necessarily imply that there are no time-lapse changes in other attributes. 4D repeatability can be significantly improved by careful processing, which in turn facilitates detection of subtle time-lapse changes. In this case study, a judicious multiple removal and geometry calibration is crucial to obtain improved 4D repeatability and data quality. It is also very important to compare and contrast various attributes, including, for example, time shifts, time-lapse attenuation and impedance inversions. Combining analysis of multiple attributes enhances our confidence in qualitative interpretation. In this study, time-lapse attenuation proved highly valuable because it provides independent information from the other attributes, both in terms of its computation via a spectral analysis, and the fact that attenuation does not depend

on velocity or density changes.

Chapter 4

4D Inversion method and Interpretation [1]

Estimating reservoir conditions is important for risk analysis and prospect development planning. I introduce a grid-search-based inversion method to discriminate between changes of pore pressure and water saturation using time shifts and time-lapse attenuation attributes. Given the initial conditions, the inversion method compares the measured with the grid-predicted time-lapse attributes to find the most likely updated reservoir conditions from the solution space. A synthetic example illustrates the inversion workflow and parameterization. It demonstrates a powerful visualization method in uncertainty analysis and a stable inversion algorithm using two independent input attributes. I apply our method to a real underground blowout example in the North Sea area where gas has migrated into two sandstone layers at different conditions. The inversion results show that careful data preparation and constrained initial conditions are necessary, not only to obtain stable inversion performance, but also to capture valuable information when interpreting the blowout development.

[1] A version of this chapter has been submitted to Geophysics as Dinh and Van der Baan, 2018: A grid-search approach for 4D pressure-saturation discrimination and is undergoing a minor revision request.

4.1 Introduction

In reservoir management, the final objective is to quantitatively observe reservoir parameter variations over time. Hard constraints are either obtained at a limited number of wells, or soft constraints are required from indirect observations such as time-lapse changes in reflection seismic data. Within regular reservoir properties, pressure and fluid saturation have major, non-unique effects on time-lapse seismic responses. Therefore understanding changes in pressure and saturation is important. In order to discriminate these two parameters, most of current studies use a combined rock physics model (Ødegaard and Avseth, 2003) of the Hertz-Mindlin model (Mindlin, 1949) and Gassmann's equation (Gassmann, 1951) to relate them with traditional time-lapse attributes, namely time shifts, amplitude and impedance responses (Tura and Lumley, 1999; Landrø, 2001; Moraes and MacBeth, 2005). Although the Hertz-Mindlin model has some limitations with its parameterizations and assumptions (Dinh et al., 2016), this approach works well in traditional porous sandstone and when prestack data are available. Nevertheless, because both time shifts and amplitude attributes depend on velocity changes, these inputs are not independent and reduce inversion stability.

One possible approach to reduce non-uniqueness is to employ time-lapse attenuation as additional attribute for the inversion input. Because attenuation is independent from velocity and density changes, whilst also strongly affected by the changes of pressure and saturation, combining of time-lapse attenuation enhances confidence in qualitative interpretation and quantitative inversion (Blanchard et al., 2010b; Blanchard, 2011).

In this thesis I introduce a grid-search based inversion method which uses time-lapse attenuation and time shifts to estimate changes in the reservoir. To link observations and predictions, I use an integrated rock physics model that relates changes in pressure and saturation to changes in elastic properties. Our objective is to quickly match the observed time-lapse attributes with the predicted attribute variations to find the corresponding changes in pressure and saturation. The methodology is applied on a synthetic and a real data example in the North Sea area.

4.2 Observables

In time-lapse analysis, variations in medium properties (such as P-wave velocity V_P, density ρ and attenuation Q^{-1}) cause changes in possible observables (e.g., time shifts, impedance changes, attenuation changes). In our case, I select time shifts and changes of attenuation to be the input for our inversion scheme as these are decoupled parameters.

In case of solely velocity change ΔV_P (that is, no variations in thickness), time shifts Δt can be expressed as:

$$\frac{\Delta t}{t} = \frac{\Delta V_P}{V_P}, \tag{4.1}$$

where t, V_P are the one-way travel time and velocity in the layer before the change (Landrø and Stammeijer, 2004). Practically, time shifts over a layer can be estimated from 4D seismic data by finding the lag of maximum correlation between two seismic traces of the two vintages above and below the zone of interest (Calvert, 2005).

For attenuation changes estimated from 4D seismic data, several methods can be used (Tonn, 1991) including log spectral ratio, central frequency shifts, instantaneous frequency matching. In this thesis I use the log spectral ratio (Dasgupta and Clark, 1998). The direct estimation of effective quality factor Q_{eff} changes at a reflector at time t can be linearly linked to frequency f as:

$$\ln\left[\frac{S'(f)}{S(f)}\right] = -\pi f\left(\frac{t'}{Q'_{eff}} - \frac{t}{Q_{eff}}\right) + \ln\frac{R'}{R}, \tag{4.2}$$

where S is the amplitude spectrum, R is the term containing information about the frequency independent reflectivity, primed and non-primed symbols denote the parameters in the monitor and base data (Blanchard, 2011). The interval attenuation changes between two reflectors 1 and 2 (whose arrival time is t_1 and t_2), $\Delta Q^{-1}_{eff_{12}}$, can be calculated after obtaining direct effective changes at each reflector, $Q^{-1}_{eff_1}$ and $Q^{-1}_{eff_2}$, as follows:

$$\Delta Q^{-1}_{eff_{12}} = \frac{t_2 - t_1}{Q^{-1}_{eff_2} - Q^{-1}_{eff_1}}. \tag{4.3}$$

4.3 Theory

I introduce an integrated rock physics template to link pressure and saturation variations to the changes in attenuation and time shifts (changes in velocity) mentioned above. This template is the combination of the Batzle-Wang (Batzle and Wang, 1992) equations, Reuss average (Reuss, 1929), Pore space stiffness model (Mavko and Mukerji, 1995), and Random patchy saturation model (Müller and Gurevich, 2004). The Batzle-Wang and Reuss equations estimate fluid properties with respect to pressure and saturation. The Pore space stiffness model calculates rock moduli with respect to pressure. The Random patchy saturation model uses rock and fluid moduli from the other models to calculate rock elastic properties. I summarize each of these theories below, from the most generic to most specific, starting with the final seismic properties (velocity and attenuation), and ending with computation of the rock and fluid properties. Finally I explain how the various quantities are influenced by pressure and saturation.

4.3.1 Random patchy Saturation model

The random patchy saturation theory (Müller and Gurevich, 2004) uses the effective complex P-wave modulus $\widetilde{H}$ to calculate compressional velocity V_P and intrinsic attenuation Q_{int}^{-1}:

$$V_P = \sqrt{\frac{\Re(\widetilde{H})}{\rho_S}}, \tag{4.4}$$

$$Q_{int} = \frac{\Re(\widetilde{H})}{\Im(\widetilde{H})}, \tag{4.5}$$

where $\Re$ and $\Im$ respectively represent real and imaginary parts and ρ_S is the saturated rock density, estimated from rock matrix density ρ_m, dry rock porosity ϕ and effective fluid density ρ_f by:

$$\rho_S = (1-\phi)\rho_m + \phi\rho_f. \tag{4.6}$$

The complex P-wave modulus $\widetilde{H}$

$$\widetilde{H} = H\left(1 + \frac{s}{1 + \frac{2i}{kd}}\right), \tag{4.7}$$

is a function of the effective wavenumber k of Biot's slow wave, the dimensionless inhomogeneity degree s, the heterogeneity correlation length d, and the regular (real-valued) P-wave modulus H (i.e., $H = K_S + 4\mu_S/3$ where K_S and μ_S are the bulk and shear moduli of the saturated rock), which are given by:

$$k = \sqrt{\frac{i\omega\eta}{\kappa N}}, \tag{4.8}$$

$$s = H\left[\left(\frac{\alpha^2}{L^2}N\right)^2 - \left(\frac{\alpha}{L}\right)^2\left(\frac{1}{N}\right)^{-1}\right], \tag{4.9}$$

$$L = K_D + \frac{4\mu_S}{3}, \tag{4.10}$$

$$N = \frac{ML}{H}, \tag{4.11}$$

$$M = \left(\frac{\alpha - \phi}{K_S} + \frac{\phi}{K_f}\right)^{-1}, \tag{4.12}$$

$$\alpha = 1 - \frac{K_D}{K_S}, \tag{4.13}$$

where ω is the angular frequency, K_D, ϕ, κ are the bulk modulus, porosity and permeability of the dry rock, K_f, η are the bulk modulus and viscosity of the effective fluid.

The modeled intrinsic attenuation (Q_{int}^{-1}, Equation 4.5) includes fluid effects only. The measured effective attenuation (Q_{eff}^{-1}, Equation 4.2) incorporates also the effect of scattering such that:

$$Q_{eff}^{-1} = Q_{int}^{-1} + Q_b^{-1}, \tag{4.14}$$

where Q_b^{-1} is the background apparent attenuation. In our study, Q_b is not modeled (e.g., using the approach of Van der Baan (2001); Van der Baan (2002) and references therein) but is corrected as illustrated in the two examples.

The five rock physics parameters for this model are properties of the rock (dry bulk modulus K_D, saturated bulk modulus K_S, saturated shear modulus μ_S) and the effective fluid (bulk modulus K_f and density ρ_f). These rock- and fluid-properties are respectively modeled by the pressure-dependent Pore space stiffness theory (Mavko and Mukerji, 1995) and the pressure-saturation-dependent Batzle-Wang-Reuss equations (Batzle and Wang, 1992; Reuss, 1929), as explained next.

4.3.2 Pore space stiffness model

The stiffness of the pore space describes the ability of the pore space to resist volumetric changes under external pressure (Mavko and Mukerji, 1995). The dry rock bulk modulus K_D, the first input for the Random patchy saturation model, Equations 4.10 and 4.13, can be determined from the bulk moduli of pore space K_ϕ and rock matrix K_m, given the porosity ϕ as:

$$\frac{1}{K_D} = \frac{1}{K_m} + \frac{\phi}{K_\phi}. \tag{4.15}$$

When fluid with modulus K_f is substituted into the pore space, the dry rock modulus K_D in Equation 4.15 becomes the saturated rock modulus K_S:

$$\frac{1}{K_S} = \frac{1}{K_m} + \frac{\phi}{\widehat{K_\phi}}, \tag{4.16}$$

where:

$$\widehat{K_\phi} = K_\phi + \frac{K_m K_f}{K_m - K_f}. \tag{4.17}$$

The saturated rock modulus K_S is the second input for the Random patchy saturation model, Equation 4.13.

To address the pressure dependance, Russell and Smith (2007) first rewrote Equation 4.15 as:

$$K_D = \frac{K_m}{1 + \frac{\phi}{c}}, \tag{4.18}$$

where $c = \frac{K_\phi}{K_m}$. Russell and Smith (2007) and Russell (2013) then fitted an empirical function to a single sandstone sample from Han et al. (1986)'s dataset.

This dataset consists of 75 sandstone samples from well cores or quarries with varying clay contents (2–30%) and porosities (0–50%), one third comes from the Gulf of Mexico. They obtained the following relation between the dry rock bulk modulus (K_D in Equations 4.10 and 4.15) and effective pressure P_e:

$$c = 0.065 + 0.027 \ln P_e, \tag{4.19}$$

where the effective pressure P_e can be related to pore pressure P_p and the lithostatic pressure P_l as:

$$P_e = P_l - P_p. \tag{4.20}$$

This relationship was extended by Dinh et al. (2016) when they fitted average empirical functions to Han et al. (1986)'s data. Their general relationship yields a simpler way to estimate two dry rock moduli from effective pressure, finding the following more generic relations:

$$\begin{aligned} c &= A + 0.001 P_e, \\ \mu_D &= B + 0.08 P_e, \end{aligned} \tag{4.21}$$

where A and B are free intercepts and need to be calibrated for each rock sample, 0.001 and 0.08 are best-fitting gradients for Han et al. (1986)'s 75 samples. They are obtained after dividing the full dataset into training and validation portions to encourage general applicability beyond the actual samples. A detailed derivation is shown in appendix A. I strongly recommend to test the validity of Equation 4.21 if other areas are considered. Assuming fluid substitution does not change shear modulus, the saturated shear modulus is equal to that of the dry rock (i.e., $\mu_S = \mu_D$).

In this Pore space stiffness model, the remaining parameter to calculate the saturated bulk modulus is the fluid modulus K_f (Equation 4.17). This is the effective bulk modulus of the phase-mixed fluid that can be estimated from the Batzle-Wang equations and Reuss averaging, as explained next.

4.3.3 Batzle-Wang equations and Reuss averaging

The combination of the Batzle-Wang and Reuss equations provides a pressure-saturation-dependent relationship of fluid properties, K_f, ρ_f, which are used in the Random patchy saturation (Equations 4.4, 4.12) and the Pore space stiffness models (Equation 4.17). The Batzle-Wang equations (Batzle and Wang, 1992) are sets of empirical relationships that apply for the three main fluid phases: brine, gas and oil. The Reuss equation (Reuss, 1929) is a simple average to estimate the elastic parameters for mixtures of these three phases.

According to Batzle and Wang (1992), the density ρ_i (g/cc) and modulus K_i (GPa) of each fluid phase can be empirically calculated from reservoir conditions, e.g., pore pressure P_p (MPa), temperature T (^{0}C), salinity S (weight fraction); and properties of the fluids, e.g., gas specific gravity G (API), gas to oil ratio R_G (l/l); as described below:

Brine case

In the case of brine, the modulus K_{brine} and density ρ_{brine} are given by:

$$K_{brine} = \rho_{brine} V_{brine}^2 \times 10^{-6}, \tag{4.22}$$

$$\begin{aligned}\rho_{brine} =& \rho_w + 0.668S + 0.44S^2 \\ &+ 10^{-6} S \left[300P_p - 2400P_pS + T(80 + 3T - 3300S - 13P_p + 47P_pS)\right],\end{aligned} \tag{4.23}$$

where

$$\begin{aligned}V_{brine} = V_w &+ S(1170 - 9.6T + 0.055T^2 - 8.5 \times 10^{-5}T^3 + 2.6P_p - 0.0029TP_p - 0.0476P_p^2) \\ &+ S^{1.5}(780 - 10P_p + 0.16P_p^2) - 1820S^2,\end{aligned} \tag{4.24}$$

$$\begin{aligned}\rho_w = 1 + 10^{-6}(&- 80T - 3.3T^2 + 0.00175T^3 + 489P_p - 2TP_p + 0.016T^2P_p \\ &- 1.3 \times 10^{-5}T^3P_p - 0.333P_p^2 - 0.002TP_p^2),\end{aligned} \tag{4.25}$$

where V_w is the known P-wave velocity in pure water, calculated as

$$V_w = \sum_{i=1}^{5} \sum_{j=1}^{4} w_{ij} T^{i-1} P_p^{j-1}, \tag{4.26}$$

with constants w_{ij} given in Table 4.1.

$w_{11} = 1402.85$	$w_{12} = 1.524$	$w_{13} = 3.437 \times 10^{-3}$	$w_{14} = -1.197 \times 10^{-5}$
$w_{21} = 4.871$	$w_{22} = -0.0111$	$w_{23} = 1.739 \times 10^{-4}$	$w_{24} = -1.628 \times 10^{-6}$
$w_{31} = -0.04783$	$w_{32} = 2.747 \times 10^{-4}$	$w_{33} = -2.135 \times 10^{-6}$	$w_{34} = 1.237 \times 10^{-8}$
$w_{41} = 1.487 \times 10^{-4}$	$w_{42} = -6.503 \times 10^{-7}$	$w_{43} = -1.455 \times 10^{-8}$	$w_{44} = 1.327 \times 10^{-10}$
$w_{51} = -2.197 \times 10^{-7}$	$w_{52} = 7.987 \times 10^{-10}$	$w_{53} = 5.23 \times 10^{-11}$	$w_{54} = -4.614 \times 10^{-13}$

Table 4.1: Coefficients w_{ij} for water velocity V_w calculation (Equation 4.26)

Gas case

In the case of gas, the modulus K_{gas} and density ρ_{gas} are calculated from the pseudo-reduced temperature T_{pr} and pressure P_{pr} (the critical phase homogenization conditions for mixed gas and liquid) by:

$$K_{gas} = \frac{\gamma_0 P_p}{1000 \left(1 - \frac{P_{pr}}{Z} \frac{\delta Z}{\delta P_{pr}}\right)_T}, \tag{4.27}$$

$$\rho_{gas} = \frac{28.8 G P_p}{8.314 Z (T + 273.15)}, \tag{4.28}$$

where

$$T_{pr} = \frac{T + 273.15}{94.72 + 170.75G}, \tag{4.29}$$

$$P_{pr} = \frac{P_p}{4.892 - 0.4048G}, \tag{4.30}$$

$$\gamma_0 = 0.85 + \frac{5.6}{P_{pr} + 2} + \frac{27.1}{(P_{pr} + 3.5)^2} - 8.7 \exp\left[-0.65(P_{pr} + 1)\right], \tag{4.31}$$

$$Z = U P_{pr} + (0.642 T_{pr} - 0.007 T_{pr}^4 - 0.52) + EV, \tag{4.32}$$

$$\left(\frac{\delta Z}{\delta P_{pr}}\right)_T = U + E^2 F, \tag{4.33}$$

$$U = 0.03 + 0.00527(3.5 - T_{pr})^3, \tag{4.34}$$

$$E = 0.109(3.85 - T_{pr})^2, \tag{4.35}$$

$$F = -\frac{1.2P_{pr}^{0.2}}{T_{pr}}\left[0.45 + 8\left(0.56 - \frac{1}{T_{pr}}\right)^2\right]V, \tag{4.36}$$

$$V = \exp\left\{-\frac{\left[0.45 + 8\left(0.56 - \frac{1}{T_{pr}}\right)^2\right]P_{pr}^{1.2}}{T_{pr}}\right\}. \tag{4.37}$$

Oil case

In the case of live oil, the modulus K_{oil} and density ρ_{oil} are calculated from saturation density ρ_s (with dissolved gas), pseudo density ρ_{ps} (based on the expansion caused by dissolved gas) and reference (at 15^0C) oil density ρ_0 by:

$$\rho_{oil} = \frac{\rho_s + (0.00277P_p - 1.71 \times 10^{-7}P_p^3)(\rho_s - 1.15)^2 + 3.49 \times 10^{-4}P_p}{0.972 + 3.81 \times 10^{-4}(T + 17.78)^{1.175}}, \tag{4.38}$$

$$K_{oil} = \rho_{oil}V_{oil}^2 \times 10^{-6}, \tag{4.39}$$

where

$$V_{oil} = 2096\sqrt{\frac{\rho_{ps}}{2.6 - \rho_{ps}}} - 3.7T + 4.64P_p + 0.0115\left[\sqrt{\frac{18.33}{\rho_{ps}} - 16.97} - 1\right]TP_p, \tag{4.40}$$

$$\rho_s = \frac{\rho_0 + 0.0012GR_G}{B_0}, \tag{4.41}$$

$$\rho_{ps} = \frac{\rho_0}{(1 + 0.001R_G)B_0}, \tag{4.42}$$

$$B_0 = 0.972 + 0.00038\left[2.495R_G\sqrt{\frac{G}{\rho_0}} + T + 17.8\right]^{1.175}. \tag{4.43}$$

Effective fluid properties—Reuss equation

After computing the modulus of each of n fluid phases, I use Reuss's average (Reuss, 1929) to estimate the effective fluid modulus K_f:

$$K_f^{-1} = \sum_{i=1}^{n} S_i K_i^{-1}, \tag{4.44}$$

where K_i and S_i are the modulus and saturation of individual phase mixed in the effective fluid. Reuss's equation is used because it is valid for conventional hydrocarbon substitution (assuming zero shear modulus) in terms of exactly describing effective moduli of the saturated rock (Mavko et al., 2009).

The effective fluid density ρ_f can also be determined as:

$$\rho_f = \sum_{i=1}^{n} S_i \rho_i, \tag{4.45}$$

where ρ_i are the density of different mixed fluid phases. The effective, saturated rock density ρ_S (Equation 4.4 in the random patchy saturation model) is then estimated by Equation 4.6.

4.4 Forward modeling method

The three models described in the Rock physics template link the reservoir conditions with seismic responses. Figure 4.1 summarizes the computational procedure: Firstly, from given individual fluid characteristics (gas specific gravity G, reference oil density ρ_0, gas to oil ratio R_G, brine salinity S), the effective mixed fluid properties can be estimated with respect to pressure (using the Batzle-Wang Equations 4.22–4.26 for brine, 4.28–4.37 for gas and 4.38–4.43 for oil) and fluid saturation (using the Reuss Equation 4.44). Then, from given mineral modulus of matrix composition (matrix density ρ_m, bulk K_m and shear matrix modulus μ_m) and rock porosity ϕ, the dry K_D and saturated bulk modulus K_S and shear rock modulus μ can be calculated (using the Pore space stiffness model Equations 4.16, 4.18 and 4.21) with respect to pressure and the mixed fluid properties estimated previously. Next, the complex P-wave

modulus $\widetilde{H}$ are predicted (using the Random patchy saturation model Equations 4.7–4.13) from these calculated fluid and rock properties (K_f, ρ_f, K_D and K_S). Finally, the P-wave velocity and attenuation are estimated (using the Random patchy saturation model Equations 4.4 and 4.5). When using the combined rock physics model, the remaining parameters (temperature T, viscosity η, permeability κ, correlation length d, free Pore space stiffness intercepts A, B) need to be calibrated for each case study. They can be derived from core sample measurements or by obtaining from similar researches in the same area.

In this thesis, I wish to relate changes in pore pressure and saturation to variations in P-wave velocity and attenuation (Equations 4.4, 4.5). By varying pressure (in Equations 4.21, 4.22, 4.23, 4.27, 4.28, 4.38, 4.39) and saturation (in Equations 4.44, 4.45) within a reasonable range based on the rock and fluid characteristics of the case study, the final velocity and attenuation changes are mapped accordingly (Equations 4.4, 4.5). I then obtain two 2D grids which represent possible absolute values of velocity and attenuation in the monitor dataset (Figure 4.2, step 1a). The absolute values for the base dataset with initial pressure and saturation can also be estimated using the same rock physics template (Figure 4.2, step 1b) and are represented on these maps by a specific referenced point (for example, in Figure 4.4). Finally, I convert the velocity perturbations into two-way traveltime shifts using Equations 4.1 and 4.3 while assuming a constant reservoir thickness (Figure 4.2, step 1c). The resulting maps can then be used in an inversion strategy to link variations in observed quantities to changes in pore pressure and saturation, as explained in the next section.

4.5 Inversion method

The inversion workflow is summarized in Figure 4.2. After performing forward modeling (steps 1a,b,c) and measuring the observables (step 2), I obtain two sets of time-lapse attributes: the measured time shifts ($\Delta t_{Measured}$) and attenuation ($\Delta Q^{-1}_{Measured}$) and the modeled time shifts ($\Delta t_{Modeled}$) and attenuation ($\Delta Q^{-1}_{Modeled}$) from the reference conditions of the reservoir. I solve for the

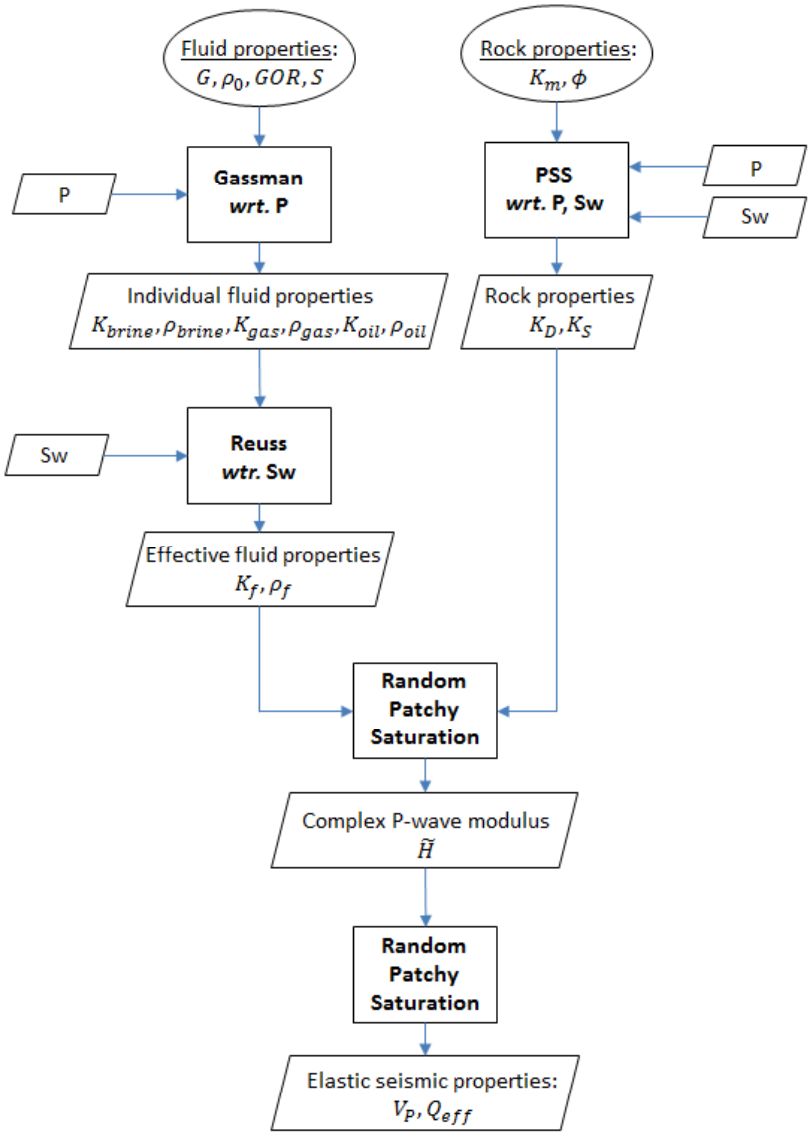

Figure 4.1: Rock physics template used for forward modeling: the fluid properties (derived from the Gassmann and Reuss equations) are combined with the dry rock properties (obtained from the Pore space stiffness model) and the Random patchy saturation model to calculate seismic velocities and attenuation. *wrt* reads "with respect to", indicating principal variable to be estimated.

time-lapse inversion problem by minimizing two misfit functions between these model predicted and actual measured time-lapse attributes.

I first calculate the misfit function of each attribute (step 3), the difference between modeled and measured time shifts ($J(\Delta t)$) and attenuation ($J(\Delta Q^{-1})$):

$$\begin{aligned} J(\Delta t) &= |\Delta t_{Measured} - \Delta t_{Modeled}|, \\ J(\Delta Q^{-1}) &= |\Delta Q^{-1}_{Measured} - \Delta Q^{-1}_{Modeled}|, \end{aligned} \tag{4.46}$$

and then compute the total joint misfit function J (step 4):

$$J = \omega_1 J(\Delta t) + \omega_2 J(\Delta Q^{-1}). \tag{4.47}$$

The purpose of the weights ω_1 and ω_2 is to ensure that both misfits ($J(\Delta t)$, $J(\Delta Q^{-1})$) contribute proportionally to the total misfits (J) by preventing dominance of a single term, for instance, because of its dimensions and range of significant values. Common choices are the reciprocals of the average individual misfits or their standard deviation. The minimum of the joint misfit J, Equation 4.47, then reveals the estimated reservoir conditions in the monitor dataset (step 5).

Because of the complex interaction between the numerous reservoir parameters, multiple scenarios can lead to the same change in observables (e.g., time shifts). Hence there is often no unique solution (that is, single minimum) in the individual misfits $J(\Delta t)$ and $J(\Delta Q^{-1})$. However, often their combination leads to a global minimum. This occurs because velocity and attenuation generally are independent quantities.

4.6 Examples

4.6.1 Synthetic time-lapse example

Problem setup

In the field example I consider an internal blowout where gas leaked into shallower layers in the North Sea area. As a result, the synthetic example will

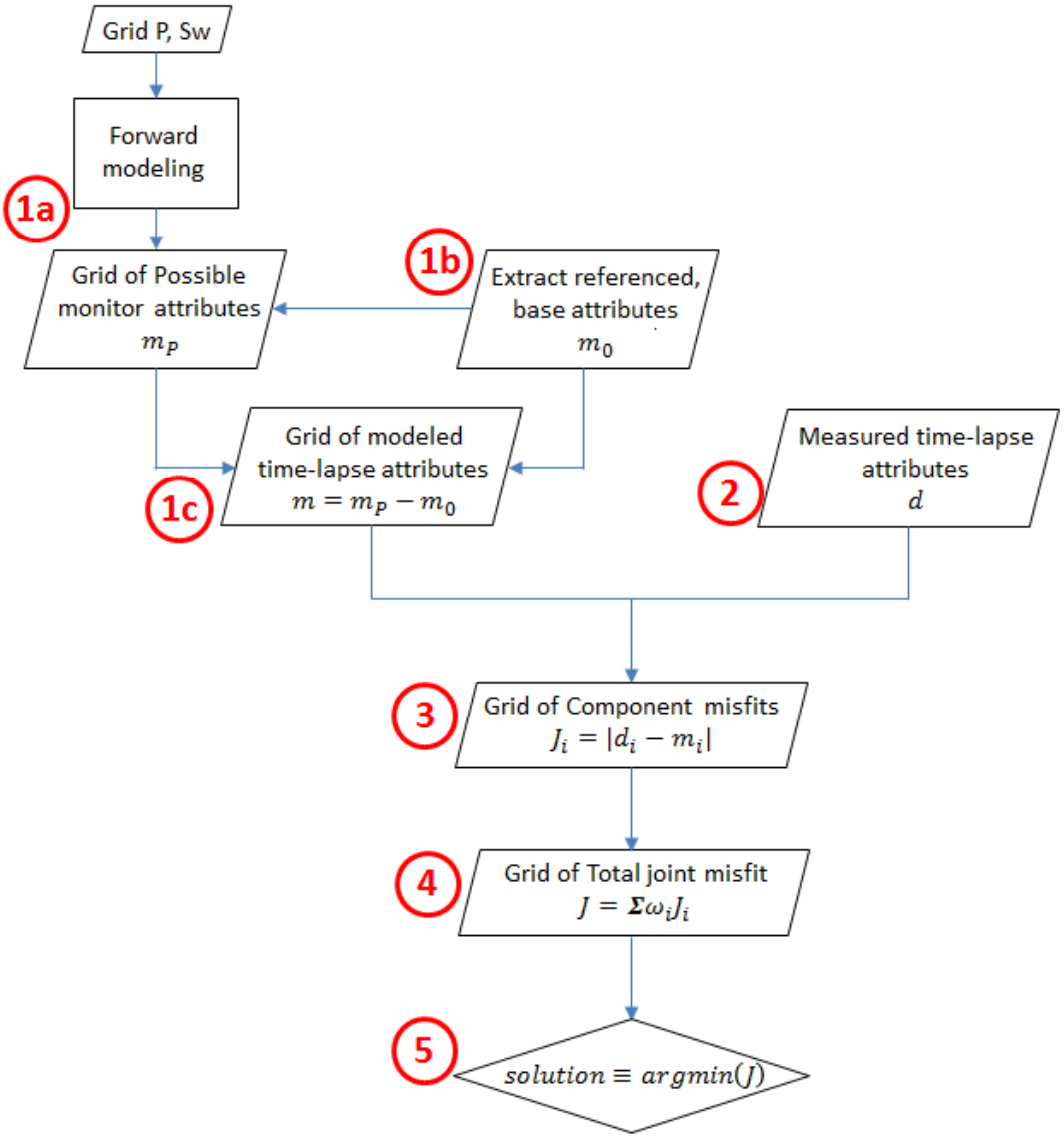

Figure 4.2: Inversion scheme: The forward modeling process creates grids of modeled time-lapse attributes (steps 1a,b,c), which are compared with the time-lapse measurements (step 2) to obtain the grids of individual component misfits (step 3). The total joint misfit is then calculated from these components (step 4). Finally, the inversion solution is the minimum of the joint misfit (step 5).

therefore show the opposite of a depletion scenario where gas content increases within a layer. Swapping the base and monitor data turns the example into a depletion case.

I create a 3-layer model where gas is introduced into the middle layer with thickness of 100 m. The top and bottom layers have identical parameters ($Vp =$ 2.6 km/s, $Vs = 1.2$ km/s, $\rho = 2$ g/cc, $Q_{int} = 10^5$) which remain fixed over time such that their exact fluid and rock parameters become irrelevant. In the middle layer, initial conditions are set as fully brine saturated $Sw_{base} = 100\%$, pore pressure $Pp_{base} = 10$ MPa, lithostatic pressure $P_l = 15$ MPa (the initial effective pressure is therefore $P_e = 5$ MPa, Equation 4.20) and a constant background attenuation of $Q_b = 150$.

To address changes in pressure and saturation only, I assume a simple set of other rock and fluid parameters in the middle layer as summarized in Table 4.2. Most of these parameters are chosen to mimic the reservoir states that were used for the field example considered below (Langseth, 2011; Bhakta and Landrø, 2014; Dinh et al., 2016). For the correlation length d (used in the Random patchy saturation model, Equation 4.7), I choose $d = 0.25$ m because it generally produces the maximum attenuation changes at a nearby location in the North Sea area (Blanchard, 2011). Corresponding elastic parameters for this layer (velocities, density and intrinsic attenuation) at initial conditions are calculated from our rock physics model and shown in Table 4.3 under base data.

I test a scenario of introducing 50% gas and increasing pore pressure to 14 MPa. The monitor elastic parameters change accordingly to these pressure and saturation variations as summarized in Table 4.3 under monitor data. To calculate the vertical-incidence seismic traces for base and monitor conditions, I convolve a 45 Hz Ricker wavelet with the reflection coefficients computed from all parameters in Table 4.3. The predicted seismic traces are displayed in Figure 4.3a. These traces are used to measure time-lapse attributes as the input for the inversion process.

Parameter and unit	Value
ϕ (%)	40
ρ_m (g/cc)	2.65
K_m (GPa)	40
μ_m (GPa)	44
T (^{0}C)	40.5
S (ppm)	15,500
G (g/cc)	0.85
η_w (Pa·s)	0.0005
η_g (Pa·s)	0.00003
κ (Darcy)	1
A (unitless)	-0.003
B (unitless)	0.51
d (m)	0.25

Table 4.2: Synthetic rock and fluid parameters, mostly chosen to reflect real data studies from Langseth (2011), Bhakta and Landrø (2014) and Dinh et al., 2016.

	Base (vel=km/s, ρ=g/cc) Pp = 10 MPa, Sw = 1				Monitor (vel=km/s, ρ=g/cc) Pp = 14 MPa, Sw = 0.5			
	Vp	Vs	ρ	Q	Vp	Vs	ρ	Q
Layer 1	2.6	1.2	2	10^5	2.6	1.2	2	10^5
Layer 2	2.85	1.88	1.99	123	1.94	1.53	1.83	61.5
Layer 3	2.6	1.2	2	10^5	2.6	1.2	2	10^5

Table 4.3: Synthetic data parameters, including velocities, density and Q factor in the three layers for the base (left) and monitor (right) conditions.

Forward modeling (Inversion scheme, step 1)

By applying the proposed rock physics template to the intermediate layer with rock and fluid parameters shown in Table 4.3, I make 2D solution grids of the reservoir P-wave velocity V_P and attenuation Q for a range of pore pressure and water saturation conditions within: Pp = 0–15 MPa ($P_P \leq P_l = 15$ MPa) and Sw = 0–1. The base and monitor states are represented by 2 points connected by an arrow indicating direction of changes on these maps (Figure 4.4).

The two modeled time-lapse changes ($\Delta t_{Modeled}, \Delta Q^{-1}_{Modeled}$) are then computed for each possible pressure and saturation as a pertubation from the initial conditions of Pp_{base} = 10 MPa, $Sw_{base} = 1$. As illustrated in Figure 4.5, both of them increase with pressure and are non-linearly dependent on satu-

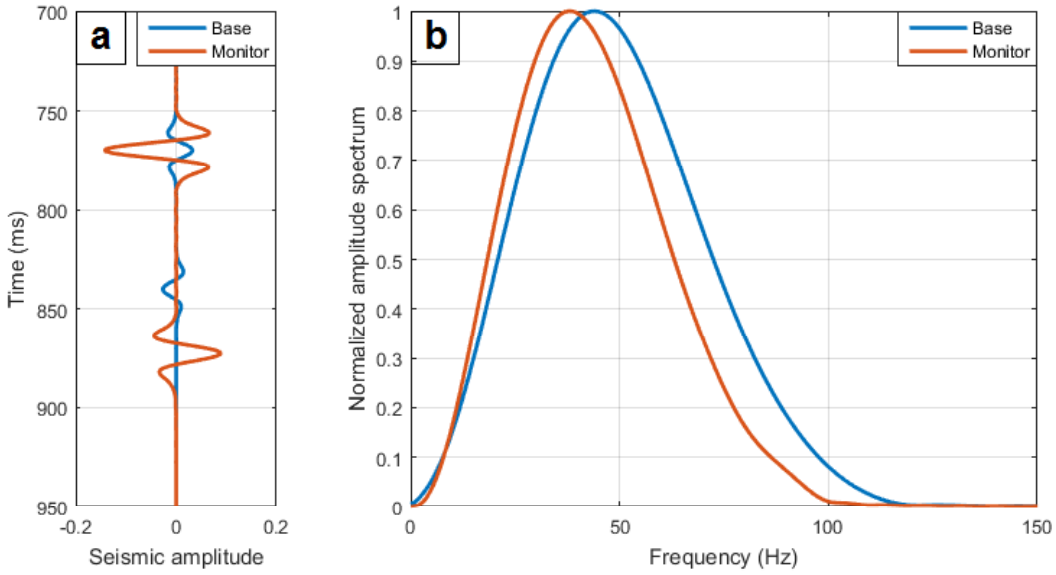

Figure 4.3: a) Base (blue) and monitor (red) seismic traces of the synthetic example using parameters in Table 4.3. b) Amplitude spectrum of the base and monitor data at the second event show movement towards lower frequency content.

ration. This similarity between them is reasonable because they are related to the complex P-wave modulus (Equations 4.4, 4.5). Despite their resemblance, differences exist. Attenuation changes foremost with saturation, whereas the P-wave velocity depends more on the pore pressure for small to intermediate water saturation ($Sw < 0.5$, Figure 4.4). Their behavior is most similar for large water saturation ($Sw > 0.8$). Similar trends can be seen in Figure 4.5 showing the corresponding time shifts and attenuation changes from base conditions. Therefore, the combination of these attributes can reveal different effects of pressure and saturation.

Measure input time-lapse attributes (Inversion scheme, step 2)

From the synthetic traces, two time-lapse attributes are measured: time shifts and attenuation changes.

The time shifts are measured by taking the differences in time arrivals at the top and bottom of the middle layer between the base and monitor traces. I assume no change in layer thickness; therefore time shifts simply depend on velocity changes (Equation 4.1). In this example, because there are no

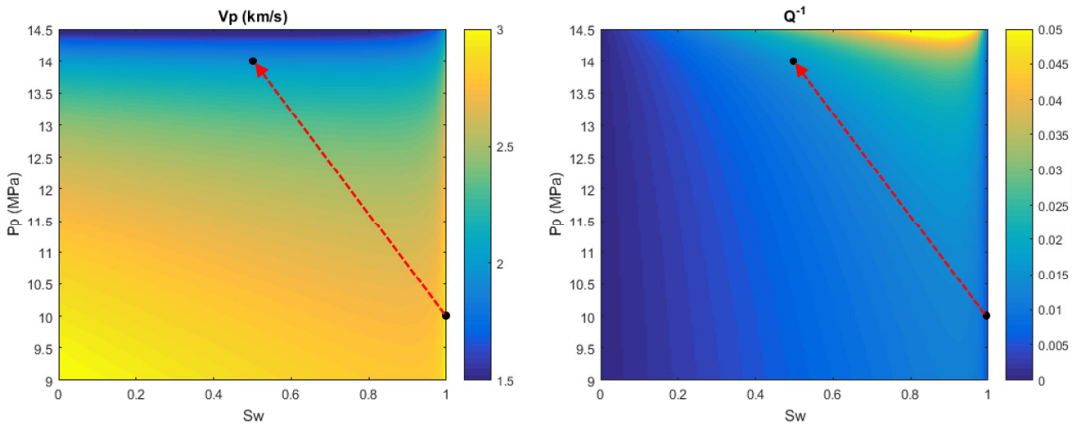

Figure 4.4: Seismic properties of the 2nd layer in the synthetic example depending on pore pressure and water saturation using the described rock physics model: P-wave velocity (left) and Attenuation (right). The red arrow represents the direction of changes from the base ($Sw = 1$, $Pp = 10$ MPa) to the monitor conditions ($Sw = 0.5$, $Pp = 14$ MPa) represented as two black circles.

velocity changes within the top layer, time shifts are determined only by time differences for the second reflector. The time shift in the synthetic example is $\Delta t_{Measured} = 33.05$ ms (Figure 4.3a).

The effective attenuation changes within layer 2 are estimated using the spectral ratio method. First, I estimate the effective attenuation changes at the top and bottom of the middle layer (Equation 4.2). The amplitude spectra of the bottom reflection (Figure 4.3b) show a shift towards lower frequencies, indicating increased attenuation. I then use Equation 4.3 to calculate effective changes within the middle layer, producing $\Delta Q^{-1}_{Measured} = 0.0081$.

Inversion process and results

Two misfit maps are created (Figures 4.6a,b) by taking the absolute value of the difference between the measured and modeled time-lapse attributes (Inversion scheme, step 3). The final misfit map (Figure 4.6c) is the weighted sum of these misfit components (Inversion scheme, step 4). In this study, I use the root mean square (RMS) amplitude ratio to weight the two input features: $\omega_1 = 1, \omega_2 = \frac{RMS(J(\Delta t))}{RMS(J(\Delta Q^{-1}))}$ (Equation 4.47), where the root mean square amplitude of each feature is the square root of mean of the squared values of that 2D grid.

In Figure 4.6c, the minimum of the joint misfit (Inversion scheme, step 5)

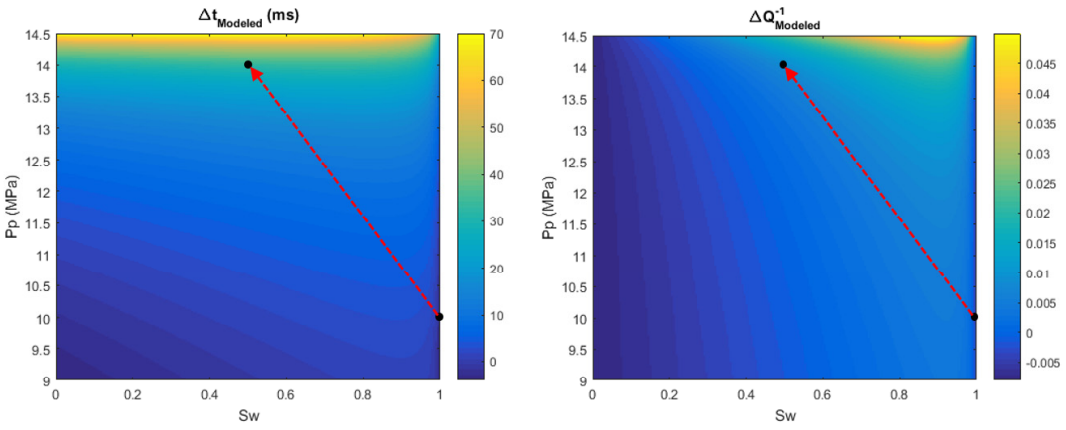

Figure 4.5: Predicted time-lapse attributes: with respect to Pp and Sw: time shifts (left) and attenuation changes (right). The red arrow represents the direction of changes from the base to the monitor conditions (two black circles): $Sw = 1$, $Pp = 10$ MPa to $Sw = 0.5$, $Pp = 14$ MPa.

shows that the monitor conditions are located at $Pp_{monitor} = 14$ MPa and $Sw_{monitor} = 0.495$. This yields the respective changes of pore pressure and water saturation of $+4$ MPa and -0.505, which are comparable with our expected values ($+4$ MPa and -0.5). This small difference occurs because I used estimated values for the time shifts and attenuation changes, instead of their exact values.

Figure 4.6 can also be used to investigate the uncertainty in estimated pressure and saturation by examining their influence on the individual and joint cost functions. In this case, both parameters seem to affect the joint cost function but not in the same way. Misfit $J(\Delta t)$ is strongly influenced by pressure only and saturation is unresolved, the other misfit $J(\Delta Q^{-1})$ indicates a positive correlation exists between pressure and saturation changes. The joint misfit however has a relatively sharp minimum, with uncertainties of $Sw = 0.50 \pm 0.05$ and $Pp = 14 \pm 0.2$ MPa if I extract the misfit functions at 95% of the minimum.

In practice, this inversion approach is repeated for each individual CMP location and all reflections of interest. It is possible to apply smoothing filters to either the estimated parameters or the joint misfit functions to stabilize the results as a function of two-way traveltime and position.

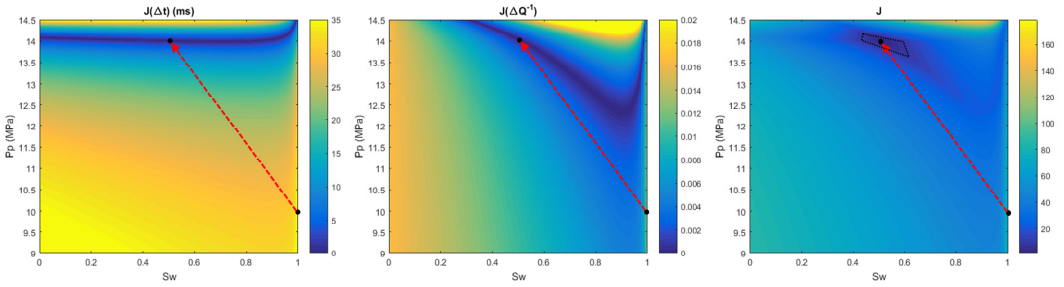

Figure 4.6: Misfit functions of the input attributes in synthetic example of individual time: time shifts (left) and attenuation changes (middle). The total joint misfit function after weighted (right) shows the minimum solution at $Sw = 0.5$, $Pp = 14$ MPa, corresponding to reservoir condition changes (Table 4.3). The dotted boundary marks the 95% of the minimum value. The red arrow represents the direction of condition changes towards the monitor conditions (black circle).

4.6.2 Real data time-lapse example

Introduction

In this field example, I look at an internal underground blowout in block 2/4, southern part of the North Sea. In January 1989, well 2/4-14, which was drilled on an Upper Jurassic prospect, kicked at 4,733 m. A relief well 2/4-15 drilled about 1,200 m to the south hit and completely killed well 2/4-14 by December 1989. However, signs of an underground blowout were recorded and leaked gas has been believed to charge mostly into two sandstone layers (Figure 4.7) located at 828 m and 495 m, chronologically (Lie and Larsen, 1991; Remen, 1991; Landrø, 2011). The deeper 87 m thick sandstone is Southwest dipping and the shallower 10 m thick sandstone is almost horizontal (Figure 4.8).

Multiple seismic surveys (2D and 3D) have been acquired in the area to monitor the blowout incident. Early interpretation of 2D seismic amplitude variations (Lie and Larsen, 1991) shows major gas leakage with main accumulation towards the Northeast in the lower 828 m deep sandstone and less influx but uniform accumulation in the upper 495 m deep sandstone by spring 1990. These observations indicate the effects of geological structure on gas migration. Remen (1991) modeled flow simulation in the deep sandstone at 6, 8, 10 and 14 months after the blowout, assuming the sandstone is 0.5 degree dipping from East to West. The time-lapse study using 2D seismic data conducted

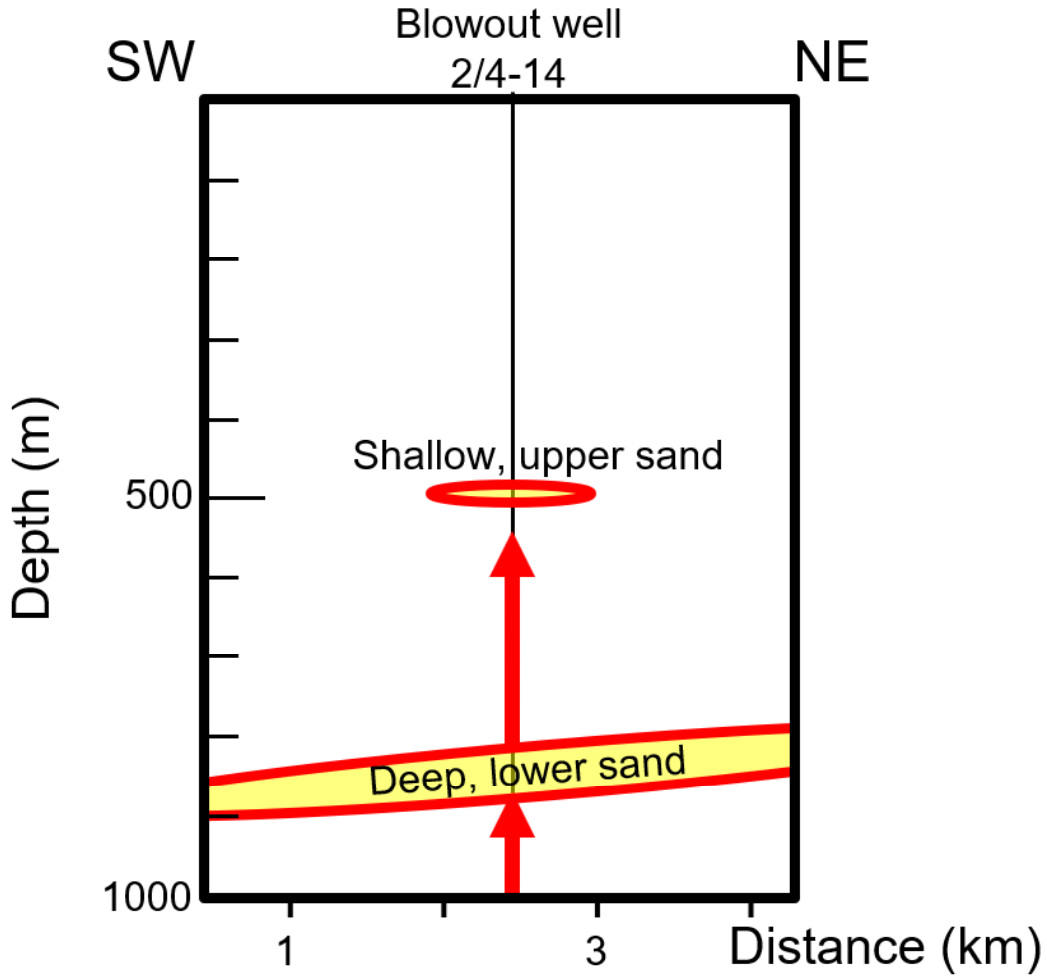

Figure 4.7: A simple sketch of the internal underground blowout in well 2/4-14 (vertical line), North Sea where gas has leaked (red arrows) into two shallow sandstones (yellow ellipses) at 828 m and 495 m. The lower sandstone is 87 m thick and dips towards the Southwest. The upper sandstone is 10 m thick and mostly horizontal. Edited from Dinh and van der Baan (2017).

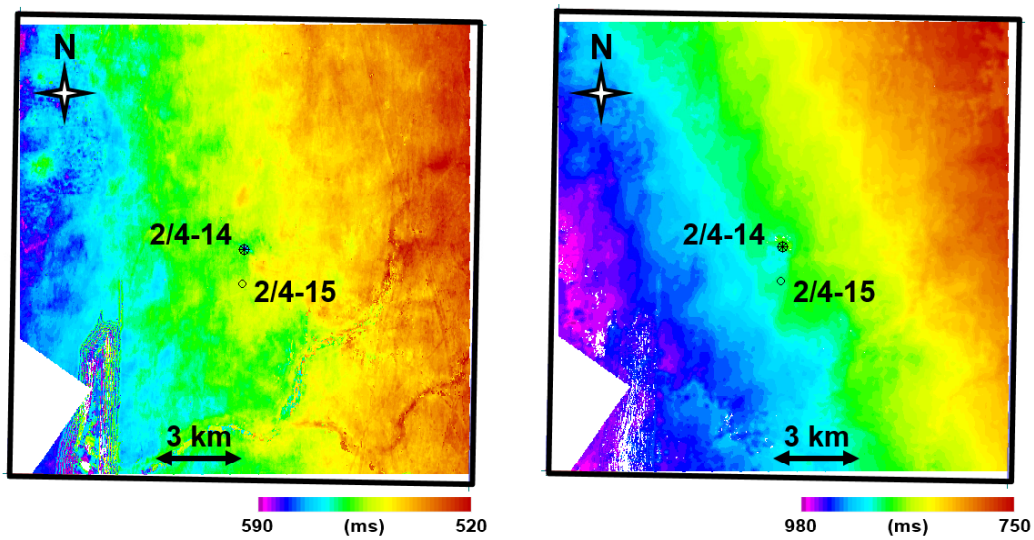

Figure 4.8: Time structure maps of the horizontal, shallower sandstone at 495 m deep (left) and the Southwest dipping, deeper sandstone at 828 m deep (right). The blowout well 2/4-14 is marked as a crossed circle. The relief well 2/4-15 is marked as the open circle at the south of well 2/4-14. Edited from Dinh et al. (2017b). Note different ranges on the color scales.

by Landrø (2011) in this area confirms gas accumulation in several sandstone layers in 1989, 1990 and 2009. This study is extended later by Langseth (2011) and Langseth and Landrø (2012) to include newer 3D seismic surveys. The authors found strong time-lapse amplitude anomalies in the shallow sandstone but very weak signals for the deeper one. Langseth (2011) performed reservoir fluid flow simulation in the two sandstone layers after the blowout in 1989, 1990 and 1996, assuming they are both flat formations. The simulation modeled gas saturation and pore pressure which I use to estimate approximate conditions at different times. When comparing the simulation with observed time-lapse signals, Langseth (2011) suggested that most observed 4D amplitude anomalies and time shifts are caused by changes in gas saturation and that pressure effects are not detectable.

Recently, Bhakta and Landrø (2014) have separated pressure and saturation effects in the shallow sandstone between 1988 and 1990 from the 2D time-lapse data. The authors used a modified AVO method proposed by Landrø (2001) which measures changes in AVO intercept and gradient. In this thesis, I investigate gas migration by applying our inversion method on the independent

time shifts and attenuation changes, obtained from Dinh et al. (2017b). The input includes time shifts and attenuation changes for both sandstone layers using the Northeast-Southwest 2D seismic line between 1988–1990 and the 3D seismic surveys between 1991–2005.

Attribute input and conditioning

Shallow sandstone

Figure 4.9 show the estimated time shifts and attenuation changes for the upper shallow sandstone between 1988–1990 and 1991–2005 (these maps are extracted under the sandstone body from the 3D volumes). Although both attributes show some gas effects between 1988–1990, only attenuation changes suggest gas movement from 1991–2005 data (it is mostly noise in the time-shift attribute). For a demonstration of our proposed inversion method, data with decent quality are required. Therefore, I do not use the noisy 3D time shifts as an input. In other words, for the shallow sandstone, only a 2D inversion between 1988 and 1990 is conducted.

From the original 2D attribute sections (Figure 4.9 left), I extract the time shifts and attenuation changes underneath the shallow sandstone horizon at 520 ms. The lateral extraction is selected for 2 km around the well to capture the attribute anomalies. After applying a smooth operator with a span of 10% of the total number of data points, I obtain symmetric anomalies around the blowout well as shown in Figure 4.10, red curves. There are noticeable non-zero artifacts at the two far ends (Northeast and Southwest) where I expect no changes of pressure and/or saturation. I preserve this input for the shallow sandstone between 1988–1990, but careful interpretation needs to be considered at the edges.

Deep sandstone

Figure 4.11 show the estimated time shifts and attenuation changes for the lower deep sandstone between 1988–1990 and 1991–2005 (these maps are extracted under the sandstone body for the 3D volumes). The 2D seismic data, whose locations are indicated by the dashed line on the maps, mostly follows the dipping structure of Northeast–Southwest. Unlike the shallow sandstone, between 1988–1900, the lower sandstone has no significant attenuation anomaly

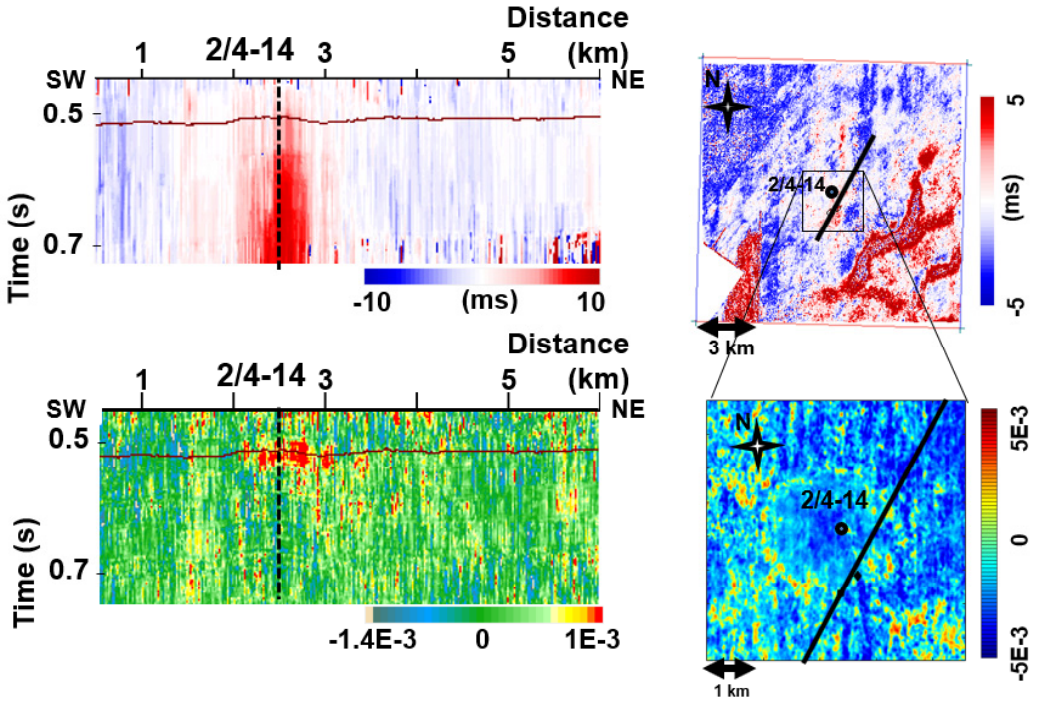

Figure 4.9: Time-lapse attributes for the shallow sandstone between 1988–1990 (left) and 1991–2005 (right): time shifts (top) and attenuation changes (bottom), for the shallow sandstone. Edited from Dinh et al. (2017b). On the 2D sections, the vertical dashed line represents the projection of the blowout well on the 2D line, the red horizon represents the interpreted shallow sandstone. On the 1991–2005 maps extracted below the sandstone body, the 2D line is marked as a solid black line, the blowout well is marked as an open black circle, the black square in time shifts map represents the boundary of attenuation changes displayed at the bottom.

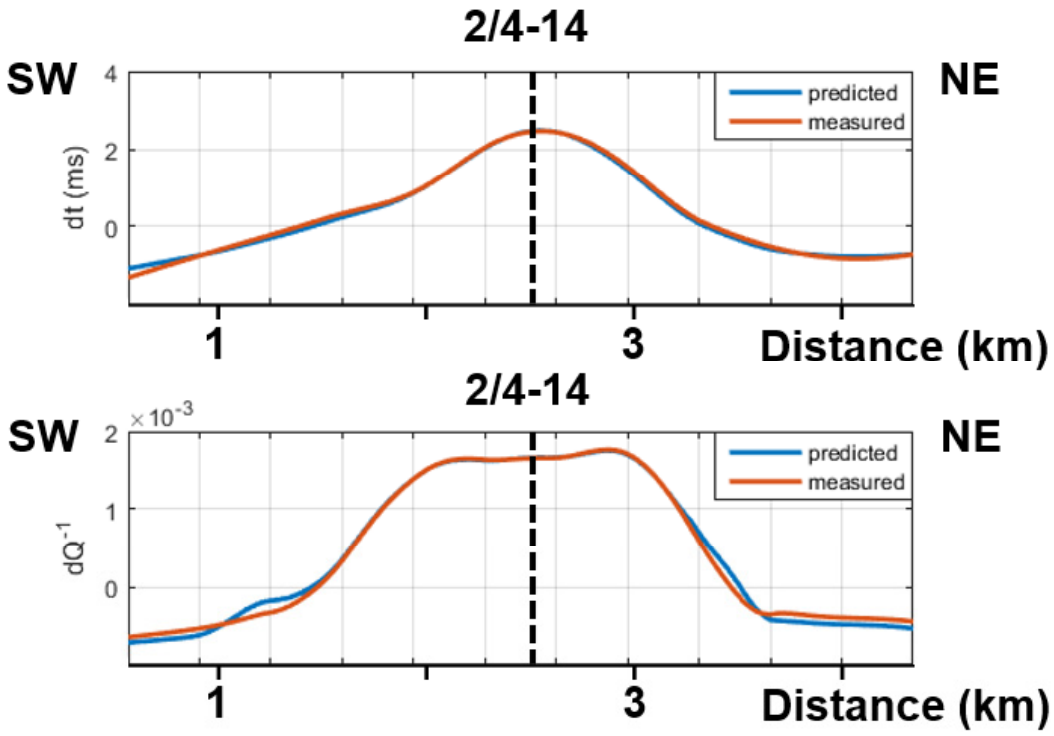

Figure 4.10: Conditioned input (red curves) and predicted attributes (blue curves) for the shallow sandstone between 1988–1990: time shifts (top) and attenuation changes (bottom). The vertical dashed line represents the projection of the blowout well on the 2D line. Both input attributes are centrally symmetric around the well location. Some non-zero values are observed at two edges of the area where zero changes are expected. The comparison between the measured and predicted attributes show small differences around the well location indicating stable inversion. Larger differences at two tails indicate less stable inversion where suspected artifacts are present in the input.

and the time-shift image is dominated by the shadow caused from the upper sandstone. On the other hand, anomalies from both attributes show up clearly on the 1991–2005 data. Therefore, for the same data quality reason, I only focus on the later time interval for this sandstone layer.

With these data (Figure 4.11, right), I extract the attributes from the Southwest to the Northeast through the blowout well 2/4-14 (black solid diagonal line). This direction is selected because it follows the dipping structure. Conversely, the shallow sandstone is mostly flat with symmetric anomalies observed around the well (Figures 4.8 and 4.9). Hence a direct comparison can be done with both inversion results despite their slightly different spatial orientations.

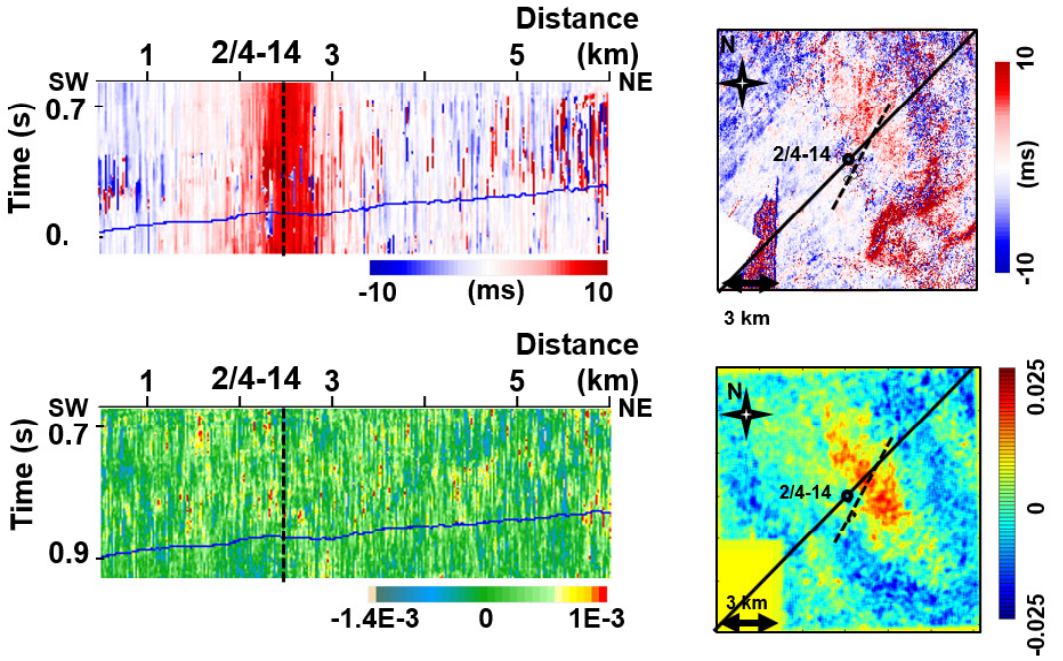

Figure 4.11: Time-lapse attributes, i.e., time shifts (top) and attenuation changes (bottom), for the deep sandstone between 1988–1990 (left) and 1991–2005 (right). Edited from Dinh et al. (2017b). On the 2D section, the vertical dashed line represents the projection of the blowout well on the 2D line, the blue dipping horizons represents the interpreted sandstone. On the 1991–2005 maps extracted below the sandstone body, the 2D line is marked as a dashed black line, the blowout well is marked as an open black circle, the inversion input is extracted along the diagonal solid black line.

In the missing-data area at the Southwest end (distance less than 4 km), I assign zero values to both attributes. Because the attributes are more noisy, I

apply a smooth operator with a span of 20% of the total number of data points, and obtain the inversion input as shown in Figure 4.12, red curves; note that the two attributes are skewed towards the Northeast updip direction.

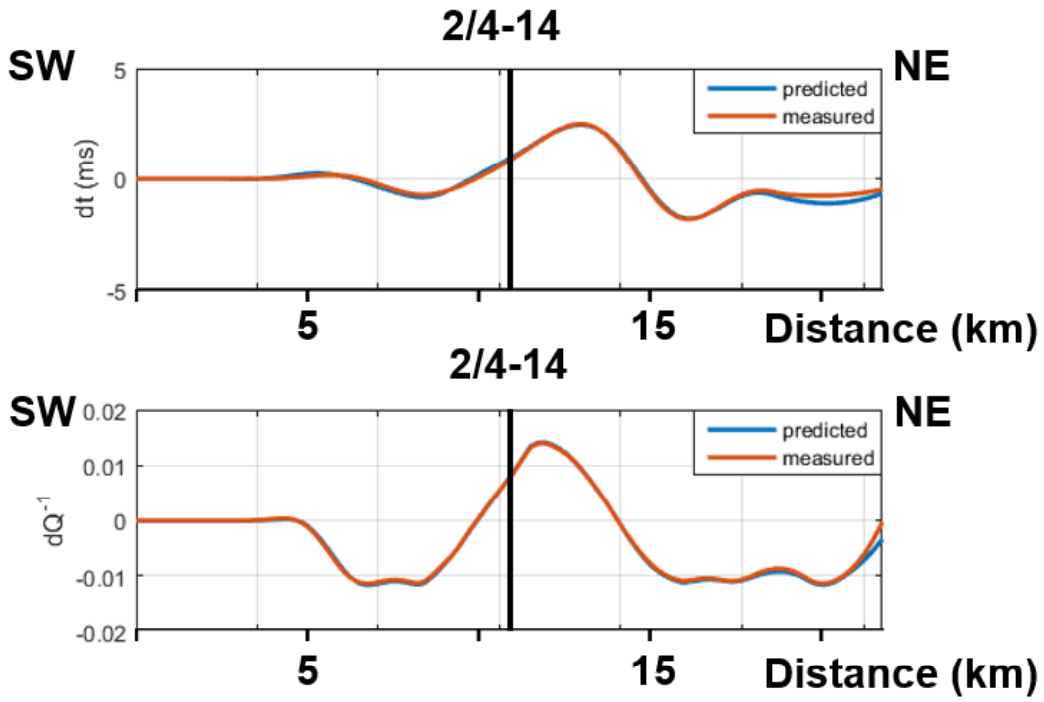

Figure 4.12: Conditioned input (red curves) and predicted attributes (blue curves) for the deep sandstone between 1991–2005: time shifts (top) and attenuation changes (bottom). The vertical line represents the blowout well location. Maximum peaks of two input attributes are skewed towards the Northeast of the well. At distance less than 4 km, the values are set to zero due to the missing data here. The comparison between the measured and predicted attributes shows slightly time-shift and attenuation discrepancies respectively at distance larger than 19.5 km which might be caused by data conditioning artifacts.

Initial conditions

Due to the data quality, I only perform inversions for two cases: (1) for the shallow sandstone, between 1988–1990 and (2) for the deep sandstone, between 1991–2005. Two initial conditions need to be set up accordingly: (1) the shallow sandstone in 1988 and (2) the deep sandstone in 1991.

The shallow sandstone, 1988

Before the blowout, I simply assume fully wet rock (Sw = 1) at hydrostatic pressure. The initial hydrostatic pore pressure is 5.1 MPa at 495 m depth ($1.05g/cc \times 9.8m/s^2 \times 0.495km$) and in agreement with reservoir simulation by Langseth (2011). This conditions are represented in Figure 4.13, blue curves.

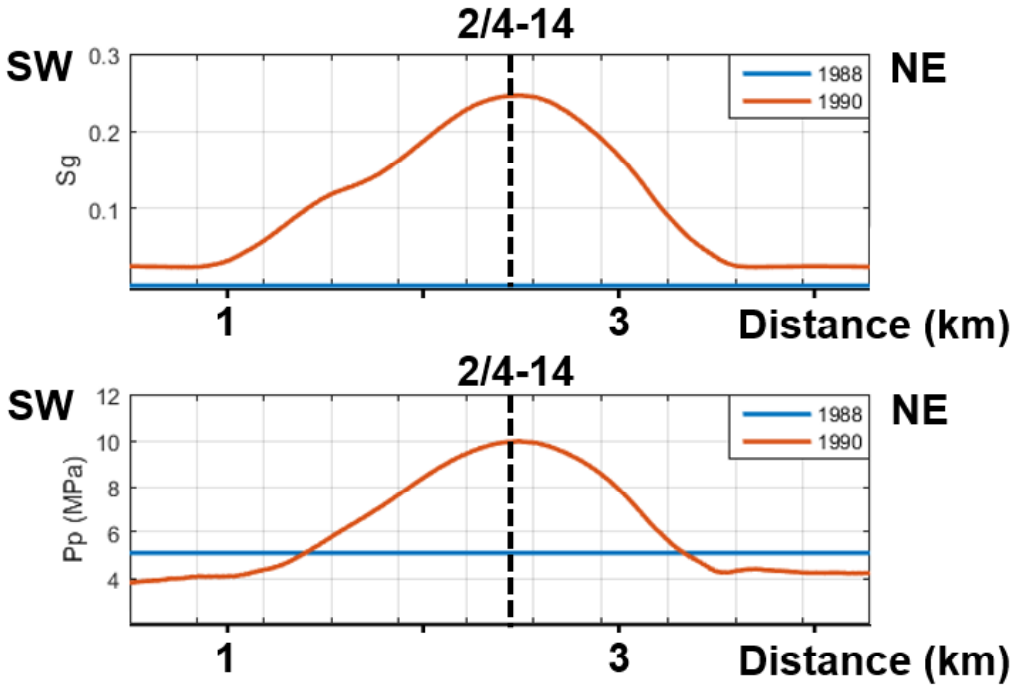

Figure 4.13: Initial conditions (blue curves) of gas saturation (top) and pore pressure (bottom) at the shallow sandstone in 1988: $Sg = 0, Pp = 5.1$ MPa. Inverted results (red curves) show that gas saturation and pore pressured has increased around the blowout well projection (vertical dashed line) and spread out for 1 km. Note how gas saturation and pore pressure results respectively mimic the behavior of the time shifts and time-lapse attenuation in Figure 4.10.

The deep sandstone, 1991

At the base time in 1991, gas had been in this sandstone for three years following the 1989 blowout. Therefore, the assumption of hydrostatic pressure and fully wet is not appropriate. To obtain a more decent estimation of the initial conditions, I can estimate the 1991 pressure and saturation from the reservoir simulation results at the lower sandstone by either Langseth (2011) or Remen (1991). Both models are built to match initial flow volumes reported by the contractor from 1989. The main differences between them are the sandstone structure (Langseth assumed flat sandstone while Remen used an East–West

dipping sandstone), different time-snapshots (Langseth modeled in 1989, 1990, 1996 while Remen modeled for 4 different times within 14 months after the blowout), model variations (Langseth tested different parameter cases) and injection pressure conditions (Langseth used bottom-hole pressure while Remen used this pressure as a boundary condition).

In this thesis, I use the more recent results (Langseth, 2011) because she modeled the conditions up to 1996, which is required to estimate conditions in 1991. However, because this simulation assumed a deep flat sandstone, I will correct for the dip effect in a later step. The simulation results (Figure 4.14) show that pore pressure at the well location has reduced quickly from 24 MPa in 1989 (blue curve) to 11.5 MPa in 1990 (red curve), and slowed down to 8.2 MPa in 1996 (orange curve). Langseth (2011) noticed that the 1996 modeled pressure is below hydrostatic pressure (constant value of 8.4 MPa at this depth, assuming a flat sandstone) with lowest pressure at the well location. In the same time frames, gas saturation has reduced from 0.88 (blue curve) and 0.76 (red curve) to 0.22 (orange curve) at the well location but slightly increased from 0.15 (1989) to 0.2 (1990 and 1996) at a distance of 3 km away from the well.

I estimate the 1991 conditions by interpolating the data simulated in 1989, 1990 and 1996. Particularly, at each distance from the well, I fit an exponential function through three data points in 1989, 1990 and 1996 simulated at that location. I apply the same process for every point along the horizontal axis, in both pressure and saturation plots. Because the original simulation only models up to a distance of 7 km from the well, it does not cover the full length of our input attributes. Hence, I simply extend the 1991 conditions by assuming they are constant beyond 7 km. The interpolated 1991 data (Figure 4.14, purple curves) suggests a maximum gas saturation of 0.64 at the well location ($Sw = 0.36$) and relatively stable pore pressure between 9.1–9.3 MPa along the line.

To take the dip into account (which was not considered in Langseth's simulation), I first recalculate the hydrostatic pressure along the considered 2D seismic line (diagonal black line in Figure 4.11), assuming the sandstone is dipping towards Southwest at 1 degree as calculated by Dinh and van der Baan

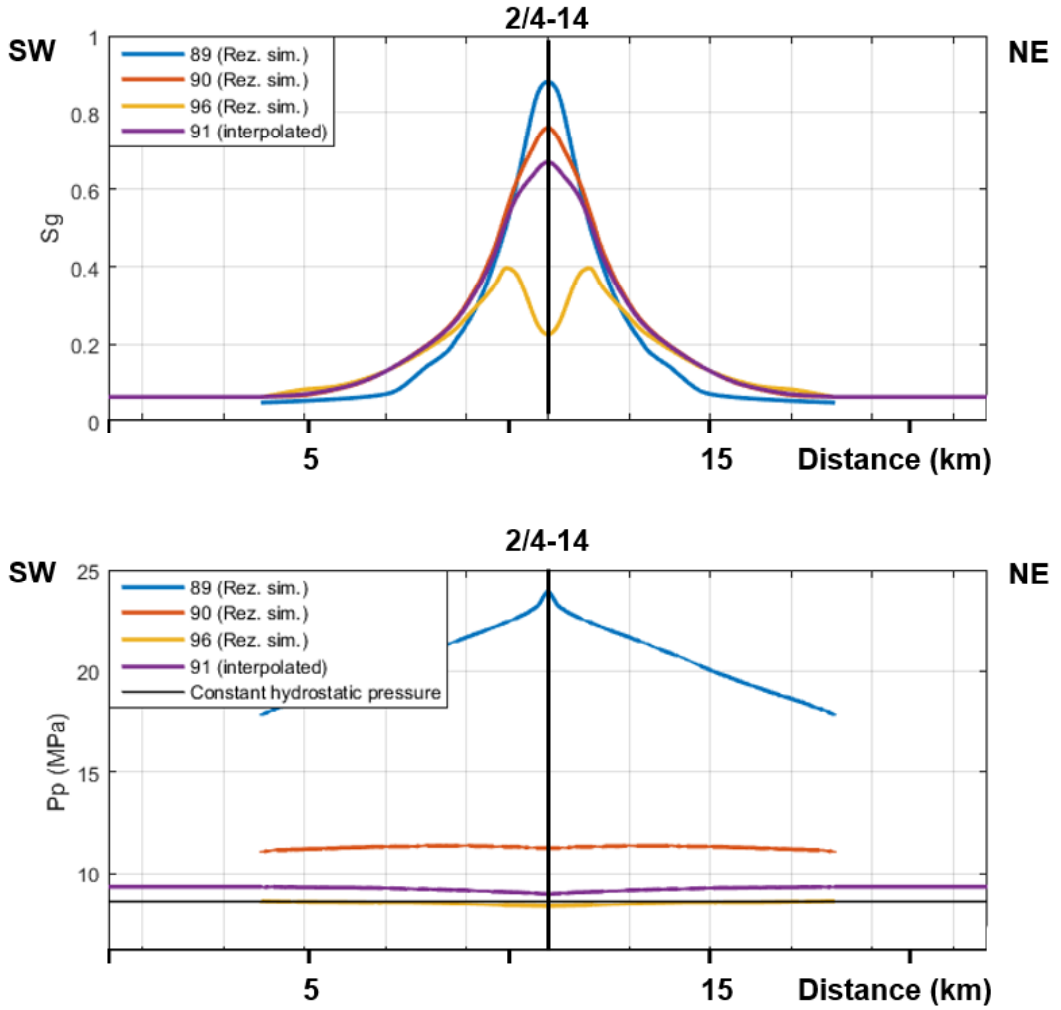

Figure 4.14: Exponential interpolation results to obtain initial conditions of gas saturation (top) and pore pressure (bottom) in 1991 (purple curve) from reservoir simulation in 1989, 1990 and 1996 (blue, red and yellow curves, respectively), edited from Langseth (2011). The horizontal black line is the constant hydrostatic pressure of 8.4 MPa (assuming the sandstone is flat). 1991 condition values are extended for distances less than 4 km and larger than 17.5 km, assuming they are constant. The vertical black line represents the blowout well location.

(2017). The hydrostatic pressure decreases linearly from 10.42 MPa at the deeper Southwest side to 6.5 MPa at the shallower Northeast side. Next, the difference between the initial 1991 pressure estimation and the constant hydrostatic pressure (difference between the purple curve and the black horizontal line, Figure 4.14) is added to the structurally-consistent hydrostatic pressure to correct for the dip effect. The initial interpolated gas saturation and this new dip corrected pressure profile are set as the final initial conditions in the deeper sandstone in 1991 (Figure 4.15, blue curves).

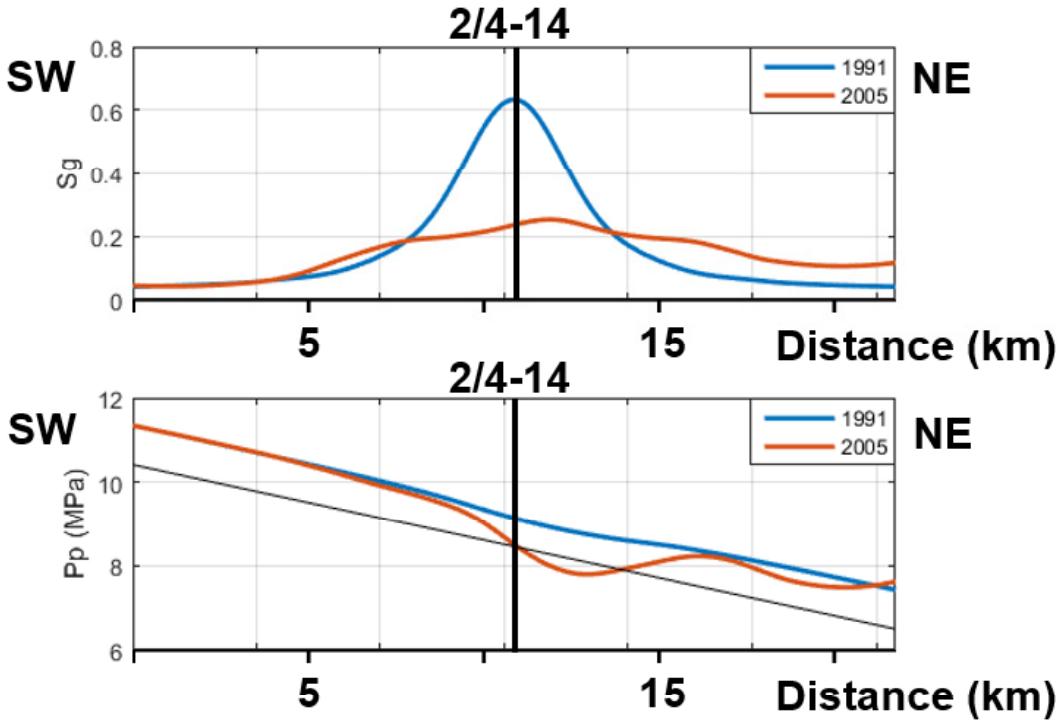

Figure 4.15: Initial conditions (blue curves) of gas saturation (top) and pore pressure (bottom) at the deep sandstone in 1991 (purple curves extracted and dip-corrected from Figure 4.14). Initial conditions at the well location are: $Sg = 0.64, Pp = 9.1$ MPa. The inverted results (red curves) show that 2005 conditions are highly skewed towards the Northeast with highest changes at distance 12.5 km. Gas is interpreted to migrate to the Northeast where lower potential is observed. The vertical black line represents the well location and the dipping black line represents the depth-dependent hydrostatic pressure.

Rock physics parameterization and Forward modeling

For rock and fluid parameters, I assume both sandstone layers have identical properties and are charged with the same type of gas from the same hydrocarbon source. Most parameters are derived from previous studies (Langseth, 2011; Bhakta and Landrø, 2014; Dinh et al., 2016) and are summarized in Table 4.2. A minor difference between the used parameters and Table 4.2 is the temperature. I assume a geothermal gradient of 2.6^0C for every 100 m depth below the 15^0C, 90 m depth sea bottom. The corresponding temperature at the shallow sandstones (495 m depth) and deep sandstone (828 m depth) are 25.5^0C and 34.2^0C, respectively.

I build a solution grid where pressure varies from 0 to 12 MPa and water saturation from 0 to 1 (corresponding to gas saturation from 1 to 0, respectively). In order to take into account the background attenuation, I set $Q_b = 150$ as the common value for porous medium. Our calculation shows that differences in temperature do not affect the outcome significantly. Therefore, the estimated velocity and Q factor of both sandstones are almost identical to Figure 4.4.

The main difference in forward modeling between this real case study and the synthetic example is the predicted time shifts, which are modeled based on the thickness of each sandstone intervals. In this field example, two modeled time shifts scenarios at two sandstone layers are illustrated in Figure 4.16. The black circles represent the initial conditions at the well location of each case: $Sw = 1, Pp = 5.1$ MPa in the shallow sandstone, 1988, and $Sw = 0.36, Pp = 9.1$ MPa in the deep sandstone, 1991 (extracted from Figure 4.15, blue curves). Initial conditions of different locations along the two sandstone layers are mapped to corresponding single points on these two grids.

Inversion and Results

For each of these two cases, the inversion is performed along its lateral direction. At each location on the horizontal axis, the two corresponding values from the input attributes (Figures 4.10, 4.12, red curves) are fed into the inversion scheme. I match our solution grid with these input features, similar to what I have done in the synthetic example, including using the RMS amplitude ratio

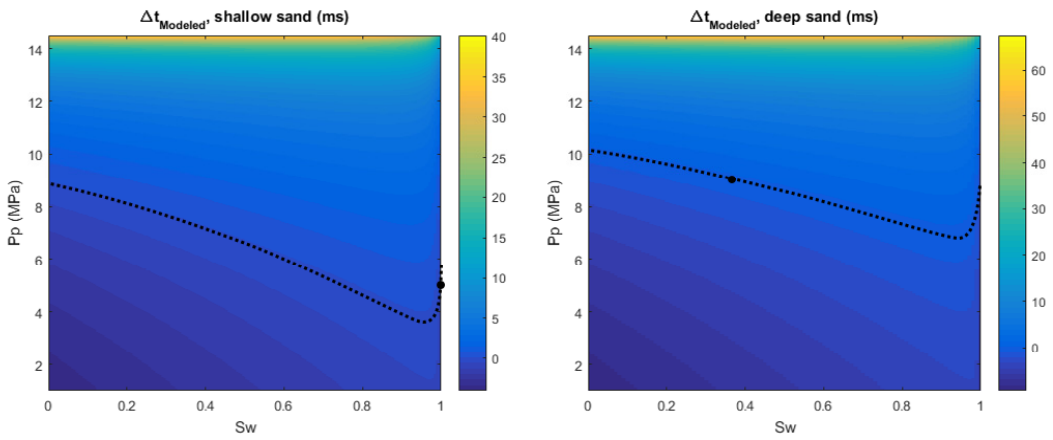

Figure 4.16: Modeled time shifts for the shallow sandstone (left) and deep sandstone (right). Black circles represent initial conditions of each case at the well location: $Sw = 1, Pp = 5.1$ MPa at the upper sandstone in 1988, and $Sw = 0.36, Pp = 9.1$ MPa at the lower sandstone in 1991 (inferred from Figure 4.15). In both cases, the dotted curve $dt = 0$ are crossing the initial condition points.

scale to sum both individual misfit functions (Figure 4.2). The output results are then smoothed with a moving average spanning 5 points. Finally, I evaluate the inversion quality by reconstructing the time-lapse attributes corresponding to the estimated pore pressure and saturation changes and comparing them with the original measured ones.

The shallow sandstone, 2D data, from 1988 to 1990

The inversion results in Figure 4.13, red curves, reveal a symmetrical image of gas saturation and pore pressure changes around the blowout well. From 1988 to 1990, a maximum increase of 0.25 gas saturation and about 5 MPa pore pressure is observed at the projection of the well location (note that the 2D line is not crossing the blowout well as illustrated in Figure 4.9). These anomalies gradually reduce in a radius of 1 km around the well projection. These extensions match the observed time-lapse anomalies (Figure 4.10, red curves). The results suggest gas saturation changes have a slightly larger lateral effect than pressure changes. Noticeably, there is a pressure reduction zone of about -1 MPa beyond the gas front where only small changes in gas saturation are observed.

Figure 4.10 compares the measured time-lapse attributes (red curves) and

the predicted ones (blue curves) from the inversion results. Overall a high similarity suggests stable inversion. However, small discrepancies at the two far ends of the line indicate areas with less confident outcomes. This may come from non-ideal data in these areas where zero changes should be expected in both attributes.

The deep sandstone, 3D data, from 1991 to 2005

On Figure 4.15, red curves, I observe a general decrease in both gas saturation and pore pressure in this time interval. Interestingly, the maximum for gas saturation and minimum for pressure in 2005 have moved away from the well for 1.5 km up dip. At the well location, gas saturation and pore pressure have reduced by 0.4 and 0.6 MPa down to 0.23 and 8.5 MPa.

In 2005, the maximum gas saturation is only 0.25 and minimum pressure is now 7.9 MPa, both observed at the distance of 12.5 km. In the Northeast side, gas saturation increases on average by 0.07 and pressure decreases on average by 0.25 MPa. Noticeably, beyond the distance of 19.5 km, there is a predicted pressure drop of 0.3 MPa and a pressure increase of 0.05 MPa at the very Northeast end.

Figure 4.12 compares the measured (red curves) and predicted (blue curves) time-lapse attributes at the deep sandstone layer. The inversion uncertainties are low at the skewed peak positions in both attributes, represented by small difference between the input and reconstructed attributes. At two sides, the uncertainties slightly increase. The highest discrepancies between the measured and predicted attributes are observed at the Northeast side for the time shifts at the distance of 19.5 km and the attenuation changes at the very end of the line. They may cause the inverted pressure drop and high pressure at these locations. Both cases correspond to the area of unexpected measured attributes because of edge artifacts due to smoothing.

Interpretation

The shallow sandstone, 2D data, from 1988 to 1990

In the upper sandstone, the inversion results suggest a simple story. Shortly after the blowout, gas has charged into the sandstone body and started to increase the pore pressure. By 1990, it reached a 0.25 saturation and 10 MPa

pressure at the well projection location and spread out radially for 1 km (Figure 4.13, red curves). This agrees with the flat, horizontal strata of the sandstone. Here, the behavior of pore pressure and gas saturation increase has a strong correlation with the variations of the input attributes (Figure 4.10, red curves).

The deep sandstone, 3D data, from 1991 to 2005

In the lower sandstone, the inverted results still share high similarities with the input time-lapse attributes (Figure 4.12, red curves). Figure 4.15 (red curves) indicates that, from 1991 to 2005, gas has moved updip towards the Northeast where lower pressure is observed, in agreement with the geological structure. The fact that both gas saturation and pressure reduce at the blow out well location suggests no more gas is charging into this sandstone. On the other hand, pressure reduction around the well location (observed at the distance of 12.5 km in 2005) may also be an indicator of vertical gas leakage to shallower formations. The 2005 pressure profile indicates that most of the sandstone formation is still overpressured (compared to the black dipping hydrostatic pressure line). There is an unexpected apparent underpressured zone at distance 12.5 km but hydrostatic pressure falls within the solution uncertainty of 0.2 MPa (Figure 4.6). The second unexpected pressure increase at the distance of 21 km is possibly caused by data conditioning as pointed out in the results.

4.7 Discussion

4.7.1 Rock physics and Forward modeling

The implemented forward modeling approach via a grid search leads to a simple but flexible inversion methodology with visual quality control. The rock physics and fluid models can be substituted if other templates are more appropriate.

An alternative to the pore space stiffness method is for instance the Hertz-Mindlin model (Mindlin, 1949). The fluid model can also be extended easily with more phases included in the fluid mixture. A complete three-phase fluid (brine, gas, and oil) modelled by Batzle-Wang equations would introduce a 3D solution grid.

Other reservoir conditions can be also considered and included. For example, in unconventional heavy oil assets, bitumen properties can be modeled with respect to temperature and pressure using the generalization of the Gassmann equation (Ciz and Shapiro, 2007) in order to investigate phase changes and increase steam chamber productivity (D. Todorovic-Marinic, personal communication, 2017).

Likewise, for the combined rock physics template, a different integrated model can be used such as those proposed by Dvorkin and Nur (1996) and Ødegaard and Avseth (2003), involving Hertz-Mindlin, Hashin-Shtrikman and Gassmann equations. They are used in AVO modeling for sandstone and therefore, becomes applicable when AVO/impedance attributes are available. In this thesis, the combination of the pore space stiffness and random patchy saturation models is chosen because of their generality. For instance, the pore space stiffness model incorporates the Gassmann equation and can be applied in unconsolidated sandstone (Dinh et al., 2016). Similarly, the random patchy saturation model can predict attenuation.

The random patchy model assumes of mesoscopic fluid flow (diffusion) which is dominant in homogeneous, partially saturated rock (Müller et al., 2010). In other cases when attenuation is known to be caused by other mechanisms, macroscopic global flow (Biot, 1956; Mavko et al., 2009), the microscopic local squirt flow (Mavko and Jizba, 1991), its extensions (Dvorkin et al., 1995; Gurevich et al., 2010), or dynamic permeability (Pride et al., 2004) may be more appropriate.

4.7.2 Parameterization

The combination of different rock physics models requires careful parameterization. Different parameters contribute to the elastic properties differently. Initial sensitivity tests show that gas gravity, temperature, salinity in Batzle-Wang-Reuss equations and rock bulk and shear moduli, porosity in pore space stiffness model have only a small effect on the final predictions.

Parameters in the Random patchy saturation have more impact, mostly on gas saturation results. In descending order, gas saturation is most affected by

the heterogeneity correlation length d (uncertainty variation up to 0.25) and permeability (uncertainty variation up to 0.05–0.1). The correlation length d can be statistically analyzed from well-log (White et al., 1990) or VSP data (Müller and Shapiro, 2001). It can be also estimated from the CT scans of the rock sample (Müller and Gurevich, 2004) or chosen such that experimental and theoretical maximum attenuation concur (Blanchard (2011) proposed a good range for d between 0.1–0.6 m).

Another important parameter in the forward model process is the background attenuation Q_b. Since apparent attenuation can be even greater in magnitude than intrinsic attenuation (Kang and McMechan, 1994; Van der Baan, 2002), the measured effective attenuation (Equation 4.2) does not necessarily represent changes in the intrinsic attenuation which are caused by pressure and saturation variations. Assuming the fluid-caused intrinsic attenuation, the non-fluid-related apparent attenuation can be estimated by comparing core attenuation measurement in dry versus saturated cases (Toksöz et al., 1979; Winkler, 1983). Q_b is normally found between 120–750 for seismic bandwidth between 20–150 Hz (White et al., 1990).

In the Pore space stiffness model, the linear coefficients (intercepts and gradients in Equation 4.21) need to be calibrated from core sample measurements for each case study. The calibration is performed by the process of dividing measurements into training and validating datasets and fitting Equation 4.21 to the various trends (Dinh et al., 2016).

In this case study, most parameters are best assigned from available data and analyses and may not represent true properties of the sandstones. The rationale for this selection comes from the fact that very limited field measurements were recorded at these sandstones in the blowout. My assumption of 40% porosity (close to critical porosity value of typical sandstone), and 1 Darcy permeability (Table 4.2) may imply better quality sandstones than reality. Using these parameters may lower the validity of the inversion results but does not affect the demonstration of the inversion method feasibility. For justification, porosity logs and Gamma ray logs would be helpful to estimate these parameters.

4.7.3 Inversion scheme

The grid-search inversion approach has two main advantages. First, it incorporates the full nonlinear behavior in the implemented rock physics and fluid models, instead of using linearization to facilitate the inversion. Secondly, it provides an effective visualization to examine and investigate numerous quantities including pore pressure and saturation, the elastic and attenuation properties, reservoir conditions and the solution space. This visualization is useful for quality control as it gives insight into the solution space. For instance, whether solutions are well constrained or multiple minima do or do not exist. Plus, the stabilization with an L1 norm (Equation 4.46) reduces noise sensitivity of the algorithm.

4.7.4 Real example

Shallow sandstone, from 1988 to 1990

The most recent studies on the shallow sandstone in this time frame are the reservoir simulation by Langseth (2011) and saturation-pressure inversion by Bhakta and Landrø (2014) based on changes in AVO intercept/gradient. At the projection of the blowout well on the 2D line, Langseth (2011) modeled gas saturation increase from 0–0.37 and pore pressure increase from 5.1–9.7 MPa, Bhakta and Landrø (2014) estimated gas saturation increase from 0–0.1 and pore pressure increase from 3.5–6.3 MPa, and our inversion results predict a gas increase from 0–0.25 and pore pressure increase from 5.1–10 MPa.

These various predictions all agree in terms of general trends of increased gas saturation and pore pressure, although the actual numbers vary somewhat due to different methodologies and estimations for initial conditions. Bhakta and Landrø (2014) base their predictions on time-lapse AVO inversion of the same original 2D seismic line that I used (albeit with different processing applied, less focused on enhancing repeatability) and use a different rock physics model (a combination of the Hertz-Mindlin and Gassmann equations). Yet qualitatively their predictions agree with ours. Since this is an internal blowout, unfortunately only very limited information is available on the actual in-situ conditions at any time, likely causing some of the divergence between the var-

ious predictions.

Deep sandstone, from 1991 to 2005

Unfortunately, no other data-driven inversion results exist for the deep sandstone in this period. In addition, the Langseth (2011) simulation study is used as an initial condition. Nevertheless, our study has provided the first look into the lower sandstone 16 years after the blowout. The results indicate continued up-dip gas movement from 1991–2005, extending early findings of Lie and Larsen (1991) for 1990 and 1991.

Attenuation behavior

From the same time-lapse attenuation observations (Figures 4.9 and 4.11), Dinh et al. (2015) suggested simple qualitative changes in gas saturation and pore pressure. Their study interpreted that gas migration can be associated with both increased and decreased attenuation, depending whether initial gas saturation is lower or higher than 20% which corresponds to maximum attenuation changes for the chosen rock physics parameters (Table 4.2). This interpretation is now quantified in our field example. I also observe that an attenuation increase may correspond to *both* increasing and decreasing of *both* pore pressure and gas saturation. A similar observation on the time shifts (Figure 4.11) suggests similar behavior for P-wave velocity.

Indeed, all these behaviors can be inferred from Figure 4.5, right. Depending on the initial condition, a same attenuation variation can read different changes in the two conditions. This is not specific to attenuation because both P-wave velocity increase and decrease can also be related to gas migration as illustrated in Figure 4.5, left. Regarding attenuation, in the shallow sandstone, its increase corresponds to the increase of both gas saturation and pore pressure because of the significant drop of Q-factor when gas is introduced to a wet condition. In the deeper sandstone, an increase of attenuation is caused by the reduction of both gas saturation and pore pressure. For example, at the distance of 12.5 km where gas has already existed, a decrease in both gas saturation and pressure can increase attenuation.

4.8 Conclusion

I have developed a grid-search inversion scheme to solve for changes in pore pressure and fluid saturation from time shifts and attenuation changes. These two independent attributes are predicted from a flexible combined rock physics modeling framework. Since most 4D inversion methods are generally based on linearized complex rock physics models and dependent variables, our approach promises a better inversion performance. Our synthetic example illustrates the feasibility of the method and introduces an easy way to visualize the solution space. For a real blowout example, our method estimates reasonable gas saturation and pore pressure that are consistent with the geological structure. For reservoir application, results could be used to update existing reservoir simulation models.

4.9 Appendix A: Derivation of Equation 4.21[1]

The following appendix presents the foundation of the extended Pore space stiffness rock physics model presented earlier in this chapter.

4.9.1 Summary

In this thesis I develop a new pressure-dependent rock physics model combining Gassmann's equation and pore space stiffness. I first introduce the pore space stiffness concept (PSS). I then use laboratory sandstone measurements to derive and validate empirical relationships between two rock moduli and the effective pressure. The pore space stiffness and the shear modulus are found to be linear dependent on various expressions of pressure but are most stable with respect to linear pressure. Finally I compare the PSS model with the classical Hertz-Mindlin contact theory. The simpler linear pressure PSS-based rock physics model provides more reasonable predicted velocities in the low pressure zone. This new PSS model is thus more suited for shallow reservoirs and/or

[1]A version of this appendix has been presented as Dinh, N. H., M. Van der Baan, and B. H. Russell, 2016, Pore space stiffness approach for a pressure-dependent rock physics model: 86th Annual International Meeting, SEG, Expanded Abstracts, 3226–3230.

unconsolidated sandstones.

4.9.2 Introduction

In rock physics modelling, Gassmann's equation often provides reasonable estimates for seismic velocities for different fluid states. However, the dependency of velocity on pressure is more difficult to predict precisely. The most widely-known method used to calculate the rock moduli from the effective pressure P_e is based on the Hertz-Mindlin grain contact theory (Mavko et al., 2009), where:

$$\begin{aligned} K_D &= f_1(\sqrt[3]{P_e}), \\ \mu_D &= f_2(\sqrt[3]{P_e}), \end{aligned} \tag{4.48}$$

for dry bulk modulus K_D and dry shear modulus μ_D. However the applicability of this model is limited because its heavily parameterized equations tend to overestimate the velocity (Duffault and Landrø, 2007). In addition, it is based on the less realistic assumption of identical spherical grains.

Recent studies of Russell and Smith (2007) and Russell (2013) have showed that for a constant pore pressure, pore space stiffness theory can be used to predict the effective moduli better than Hertz-Mindlin based models. From empirical sandstone measurements, the pore space stiffness and the ratio of bulk to shear modulus were found to be constant over a range of porosities. It is less clear if this model also applies for varying pore pressures.

In this study, I use data from Han (1986), the same data as used by Russell (2013), to investigate more general relationships between the rock moduli and the effective pressure, assuming constant rock porosity. I show the effective moduli can be expressed in simple linear relationships with respect to pressure, still providing reasonable velocity predictions, especially for low pressure zones.

4.9.3 Pore space stiffness model (PSS)

The pore space stiffness K_ϕ (or "pore space bulk modulus") is defined as the inverse of the pore space compressibility. It measures the resistance of a dry pore to changing its volume V under an external confining pressure P_c at a

constant pore pressure P_p (Mavko and Mukerji, 1995):

$$\frac{1}{K_\phi} = -(\frac{1}{V_P})\frac{dV}{dP_c}|_{P_p}. \tag{4.49}$$

In case of a dry rock with porosity ϕ, its bulk modulus K_D can be calculated from the mineral bulk modulus K_m and the "pore space bulk modulus" K_ϕ as

$$\frac{1}{K_D} = \frac{1}{K_m} + \frac{\phi}{K_\phi}. \tag{4.50}$$

When considering the saturated rock as a dry pore replaced by a fluid, the saturated bulk modulus K_S is expressed as

$$\frac{1}{K_S} = \frac{1}{K_m} + \frac{\phi}{\tilde{K_\phi}}, \tag{4.51}$$

where $\tilde{K_\phi} = K_\phi + \frac{K_m K_f}{K_m - K_f}$ is the saturated pore space stiffness and K_f is the fluid bulk modulus.

Using Equation 4.50 to eliminate the pore space compressibility in Equation 4.51 I get the well-known Gassmann's equation for fluid substitution in saturated rock:

$$\frac{K_S}{K_m - K_S} = \frac{K_D}{K_m - K_D} + \frac{K_f}{\phi(K_m - K_f)}. \tag{4.52}$$

Equations 4.50 4.52 show that the dry moduli and saturated moduli share the same physical essence and are strongly connected by the material stiffness concept (Mavko and Mukerji, 1995, and Russell, 2013).

4.9.4 Pore space stiffness and Pressure

As proposed by Russell and Smith (2007), Equation 4.50 can be rewritten as

$$K_D = \frac{K_m}{1 + \frac{\phi}{k}}, \tag{4.53}$$

where $k = \frac{K_\phi}{K_m}$. From the PSS definition (Equation 4.49), the ratio k is inferred to be constant with constant pore pressure. They also found that k is linearly dependent on the natural logarithm of effective pressure:

$$k = 0.065 + 0.027ln(P_e). \tag{4.54}$$

However, this relationship was derived from only one sandstone sample (Russell and Smith, 2007) and therefore may not be statistically sufficiently reliable.

The modulus ratio ${}^{K_D}/_{\mu}$ is also found to be constant for constant pore pressure (Murphy et al., 1993) and used in the previous PSS model (Russell, 2013). However, this observation is not valid for varying pressures. Therefore, a new shear modulus pressure relationship must also be established.

4.9.5 Workflow

The data used in this thesis are 70 sandstone samples measured by Han (1986), similar to what Russell and Smith (2007) used in their study. Measurements of P- and S-wave velocities, density and porosity were done in both the dry and wet cases at effective pressures of 5, 10, 20, 30, 40, and 50 MPa. I use the dry measurements to calculate dry moduli (bulk and shear modulus) of these samples at 6 pressure values. I then separate the data into 2 parts: 50 samples as training data and 20 samples as validating data.

With the training data, I perform 3 linear least-square fits:

$$y = I + Gx, \tag{4.55}$$

to estimate the intercept I and gradient G for various output variables y and transformed input variables x. The 3 examined input variables x are the natural logarithm of the pressure $ln(P_e)$ (as in Russell, 2013), the cubic root of the pressure $\sqrt[3]{P_e}$ (as in the Hertz-Mindlin model) and the linear pressure P_e. The output variables are the ratio k and the shear modulus μ. The first step is then to evaluate the goodness of the 3 fits for each output variable y for each individually considered training sample. A high goodness of fit means a specific

formula matches an individual sample very well.

Next I establish which relationship provides the most general empirical formula if either a common gradient or intercept across all training samples is used. I calculate and compare the scatter plot and normal root mean square error NRMSE of intercept I and gradient G for the 3 fits per output variable. The scattering coefficient of variable t at the nth sample $s_t(n)$ and the overall error $NRMSE$ of variable t (that is gradient or intercept) are calculated as

$$\begin{aligned} s_t(n) &= sign[\Delta t(n)]\frac{\Delta t(n)^2}{\bar{t}}, \\ NRMSE_t &= \frac{\sigma_t}{\bar{t}}, \end{aligned} \tag{4.56}$$

where $\Delta t(n)$ is the residual at the n^{th} sample; $\bar{t}$ and σ_t are the mean and the variance of t, respectively.

To find the most representative formula, depending only on a single degree of freedom, I keep the expression that has the smallest error and scattering variance. The other variable (that is either intercept or gradient) is then estimated from the average of the individual fits. This step ensures identification of the most generic formulae given Equation 4.55.

Finally I use the separate validation dataset to evaluate if the discovered expression for output variables k and μ leads indeed to good predictability if a single degree of freedom is used in the linear Expressions 4.55.

4.9.6 Training results

Dry rock modulus versus pressure

Figure 4.17a compares the determined coefficients for ratio k versus $ln(P_e)$, P_e and $\sqrt[3]{P_e}$. All three linear fits show good correlation with average coefficient higher than 90% for most samples. Examples of linear fits are shown in Figure 4.18. Linear P_e has slightly lower correlation than the two transformed pressures. However, estimated intercepts and gradients for linear pressure are less diverse (Figure 4.17b). Table 4.4 shows the normalized RMS errors for intercept and gradient in each case. Clearly, the averaged gradient has a smaller

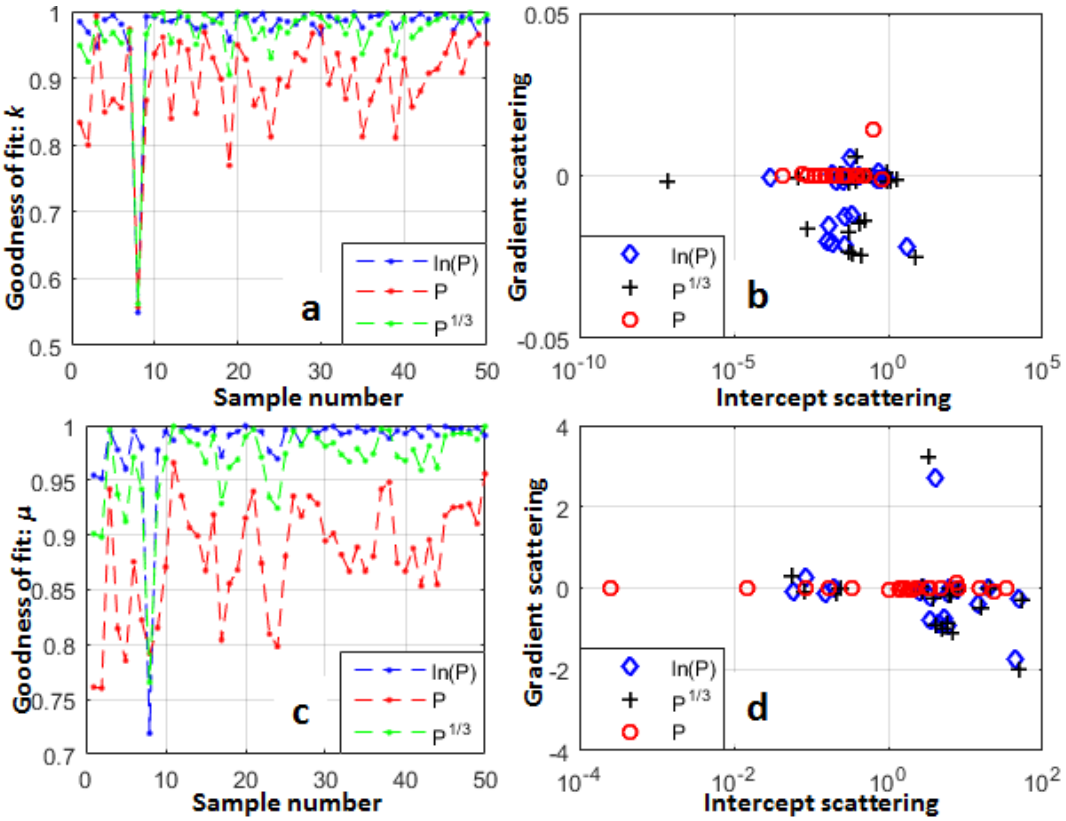

Figure 4.17: Coefficients of determination show good correlation of k (a) and μ (c) as a function of ln(Pe), Pe and $\sqrt[3]{P_e}$), expressed by blue, red and green dashed lines, respectively. Scatter plots show smaller variations in individual Gradients than Intercepts for the 3 fits for k (b) and μ (d). Symbols for $ln(P_e)$, P_e and $\sqrt[3]{P_e}$ are blue diamonds, red circles and black crosses, respectively.

spread than the estimated overall intercept. Table 4.5 provides the averaged gradients for each case. I thus obtain a simple generic equation, depending only on a variable intercept. For instance, for linear P_e:

$$k = I + 0.001 P_e, \tag{4.57}$$

where I is the free intercept that needs to be calibrated for each sample using validation or independent training data.

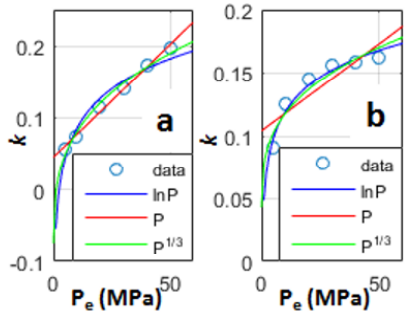

Figure 4.18: Fitness examples (from Figure 4.17a) of input variables of $ln(P_e)$, P_e and $\sqrt[3]{P_e}$ (blue, red and green curves, respectively) with training data (circles) for sample number 3 (a) and 19 (b).

NRMSE	$ln(P_e)$	P_e	$\sqrt[3]{P_e}$
$I(k)$	0.078	0.026	0.132
$G(k)$	0.0104	0.0005	0.0124
$I(\mu)$	4.158	2.828	4.458
$G(\mu)$	0.349	0.017	0.409

Table 4.4: Normal root mean square error of the intercept and gradient in linear regression of k and μ with respect to $ln(P_e)$, P_e and $\sqrt[3]{P_e}$

Mean(G)	$ln(P_e)$	P_e	$\sqrt[3]{P_e}$
k	0.027	0.001	0.031
μ	1.74	0.08	2.00

Table 4.5: Averaged gradient of linear regressions of k and μ with respect to $ln(P_e)$, P_e and $\sqrt[3]{P_e}$

Shear rock modulus versus pressure

I repeat the procedure for predicting shear modulus μ as a function of the three pressure variables, finding similar results. High goodness of fit (in excess of 90%) is found for most samples for all three fits (Figure 4.17c); yet individual intercepts and gradients are least scattered if linear pressure is used (Figure 4.17d).

Again averaged gradients have smallest spread (Table 4.4). Thus averaged gradients (Table 4.5) provide most generic expressions. For example, for linear P_e:

$$\mu = I + 0.08P_e. \tag{4.58}$$

4.9.7 Validation results

Next I evaluate the generality derived expressions with fixed gradient using the 20 validation samples. Gradients are found in Table 4.5. I fit again Expression 4.55 for ratio k and shear modulus μ and input variables $ln(P_e)$, P_e and $\sqrt[3]{P_e}$. Figure 4.19 shows the goodness of fit is not as high as it was observed in the training data, because only a single degree of freedom remains, namely the intercept.

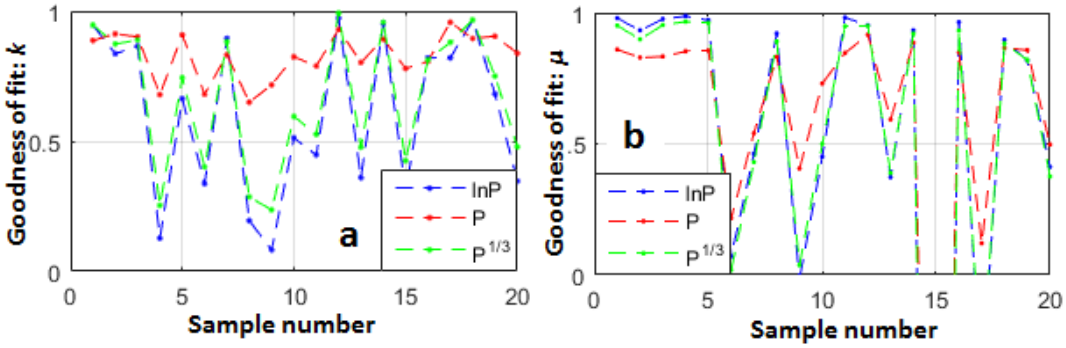

Figure 4.19: Goodness of fit shows generally better prediction of k (a) and μ (b) using linear P_e (red dashed lines).

Overall all predictions are reasonable except there are a few clear outliers for predicted shear modulus μ with even negative goodness of fits. Contrary to Figure 4.17, linear pressure as an input variable outperforms $x = ln(P_e)$ or $\sqrt[3]{P_e}$ because of the reduced spread in gradients in the latter case (Figure 4.17b and 1d). Examples of linear predictions are shown in Figure 4.20. Note that the original Expression 4.57 derived by Russell and Smith (2007) uses the natural logarithm.

4.9.8 Application to low pressure reservoir

Finally I examine a simple but illustrative example of predicted P-wave velocities versus effective stress for a shallow sandstone formation, by comparing the PSS and more complex Hertz-Mindlin models. I choose 2 PSS models to be examined: the linear and logarithmic P_e fits with fixed Gradients given in Table 4.5. Note that the logarithmic pressure is advocated by Russell (2013), Equation 4.57.

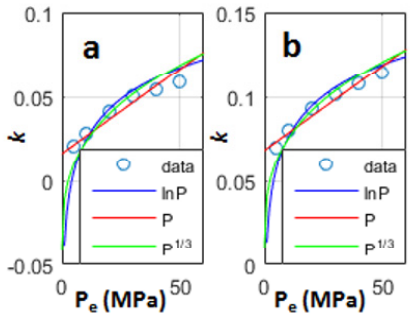

Figure 4.20: Various prediction degrees (from Figure 4.6a) of $ln(P_e)$, P_e and $\sqrt[3]{P_e}$ (blue, red and green curves, respectively) with validating data (circles) for sample number 5 (a) and 17 (b).

The case study is an internal underground blowout at the North Sea area where the gas has charged into a 495 m deep, 36% porosity sandstone layer and changed both the saturation and pressure over time (Bhakta and Landrø, 2014 and Dinh et al., 2015). The initial P-wave velocity is assumed to be 1,950 m/s before the blowout (Bhakta and Landrø, 2014). Corresponding S-wave velocity is assumed to be 698 m/s.

I assume fully wet saturated rocks ($Sw = 1$) before the blowout, hydrostatic pore pressures and a lithostatic stress of 12 MPa at the sandstone body. Therefore, $P_e \approx 6.9$ MPa.

Fitting the Hertz-Mindlin model

I use the same fitting method proposed by Bhakta and Landrø (2014) . The main procedure is comprised of testing different numbers of contacts C with predefined grain properties of quartz. The final C value is chosen such that it produces the initial P-wave velocity at the initial pressure. In this case study, C = 3 works best.

Fitting PSS model

Saturated rock moduli are calculated from the initial P- and S-velocities. Dry rock moduli are then back calculated from Gassmann's Equation 4.52. To find the free intercepts, I fit the validated generality Expressions 4.55 to the assumed initial velocities using fixed gradients found in Table 4.5. The intercepts after

data matching are presented in Table 4.6.

Free I	P_e	$ln(P_e)$
k	-0.003	-0.046
μ	0.51	-2.34

Table 4.6: Free intercepts in PSS expressions of k and μ after matching initial velocities.

Comparison of rock models

I calculate the P-wave velocity for each model for varying effective pressures from 0 to 50 MPa. Figure 4.21 shows that at low pressures, the less parameterized linear pressure PSS model provides a similar velocity prediction as the Hertz-Mindlin model. At high pressures, the linear and logarithm pressure-based PSS models predict similar velocities which are substantially different from the Hertz-Mindlin predictions. This is expected because both PSS methods are derived from the same dataset with pressures varying from 5 to 50 MPa (Han's data).

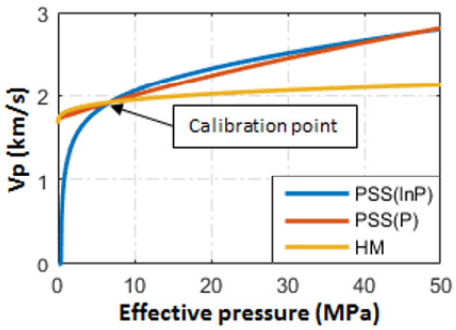

Figure 4.21: P-wave velocities predicted by Hertz-Mindlin and PSS models. The PSS model with linear pressure (red) provides a more realistic prediction than the PSS model with logarithmic pressure (blue) for very low effective pressures, with fewer parameters than the Hertz-Mindlin model (orange).

The relevance of this example is that after the blowout the increase in pore pressure leads to a further decrease in effective pressure. In this very low effective pressure regime, the linear dependence gives visually more realistic velocity predictions than the logarithm pressure variant. This observation shows

better potential performance of the linear pressure prediction in shallow and unconsolidated reservoirs.

4.9.9 Conclusion

I present a new pore-space-stiffness-based rock physics model in which the effective rock moduli are calculated from empirical linear functions of the effective pressure:

$$\begin{aligned} k &= A + 0.001 P_e, \\ \mu &= B + 0.08 P_e, \end{aligned} \tag{4.59}$$

where A and B are free intercepts and need to be fitted for every case study. The new method is easier to parameterize than the traditional Hertz-Mindlin method. An example shows that the new model is particularly promising for low pressure zones such as shallow or unconsolidated sandstone formations.

Chapter 5

Practical application: Gas migration rate[1]

I use time-lapse seismic attributes and a simple parameterization to estimate gas migration rates in a subsurface blowout using Darcy's law. Two sandstone layers in the North Sea area with different geological structures have been studied. The calculations derived from field observations show that, for a finite-duration point source (like a blowout incident), migration rates likely decrease exponentially over time with average rates as low as 9 m/year for a horizontal layer over a 16-year period which starts two years after the incident. The simple methodology developed in this thesis on how to estimate gas mobility has applications to other hydrocarbon case studies as well as studies on CO_2 sequestration and its short-term mobility.

5.1 Introduction

Monitoring hydrocarbon depletion is important in reservoir management. This includes aspects such as fluid migration fronts monitoring and enhanced hydrocarbon recovery schemes. Knowledge of fluid migration paths and rates are

[1]A version of this chapter has been presented as Dinh, N. H., M. Van der Baan, and M. Landrø, 2017, Estimation of shallow gas-migration rates after a subsurface blowout using time-lapse attributes: 87th Annual International Meeting, SEG, Expanded Abstracts, 1882-1886.

also useful in CO_2 sequestration projects. This thesis shows how gas migration rates over a 16 year period can be estimated from time-lapse seismic attributes using an internal underground blowout as a case example. The gas migration velocity in this incident also provides pertinent information on the potential of mobility in other hydrocarbon recovery or injection operations and for CO_2 storage planning.

In January 1989, an internal underground blowout occurred in block 2/4, Norwegian sector, North Sea area. The leaked gas charged and migrated into two sandstone layers: an 87 m thick, southwest dipping formation at 828 m and later another 10 m thick, flat formation at 495 m (Lie and Larsen, 1991; Landrø, 2011; Dinh et al., 2017b). Several seismic surveys have been acquired before and after the blowout in 1988, 1990 (2D), 1991 and 2005 (3D). Initial examination on 2D seismic amplitude anomaly from Lie and Larsen (1991) shows uniform lateral gas extension in the shallow sandstone and northeast oriented gas migration in the deep sandstone (Figure 5.1). A similar trend of movement in these two sandstone layers is observed in time-lapse attenuation maps (Figure 5.2) obtained from comparing the 1991 and 2005 datasets (Dinh et al., 2017b).

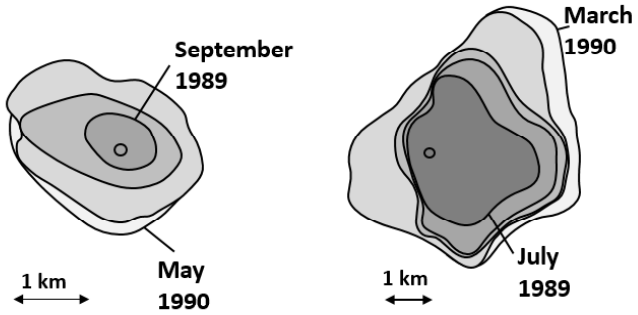

Figure 5.1: 2D seismic amplitude anomaly maps showing gas movement after the blowout in the shallow (a) and deep (b) sandstone layers (edited from Lie and Larsen, 1991). Circle indicates the blowout well.

In this thesis, I analyze the gas migration rate within these sandstone layers in two different time frames of the data (1988–1990 and 1991–2005). I first use Darcy's law to describe gas migration rates in the sandstone layers. I then break the movement mechanism (potential caused by pressure difference) into

simpler pressure components determined by the physical characteristics of each layer. Migration rate is finally estimated using simple parameterizations and the observations of the 2D seismic amplitude anomaly maps from Lie and Larsen (1991) and 4D attenuation maps from Dinh et al. (2017b) (further details are in Chapter 3).

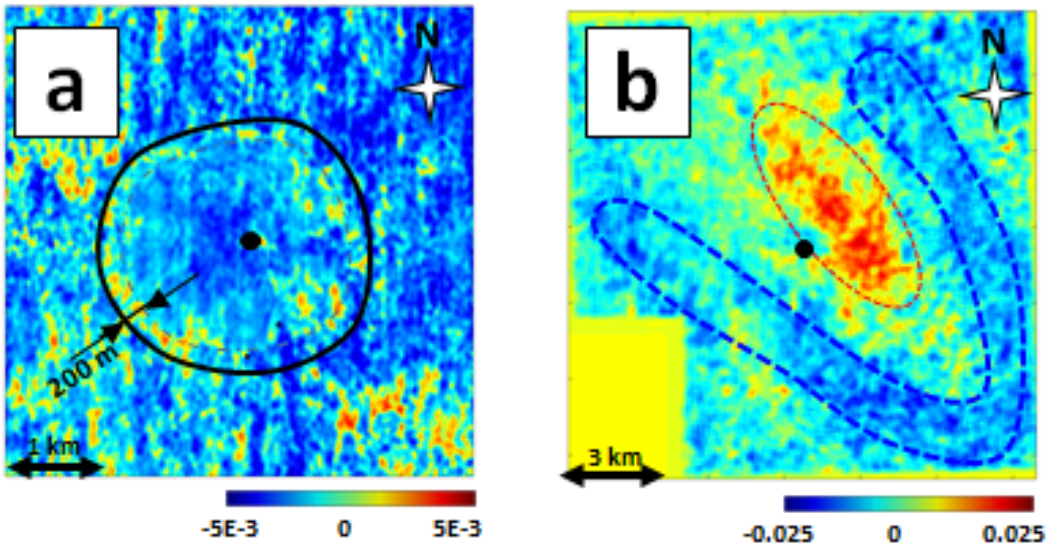

Figure 5.2: 4D attenuation anomaly maps showing gas movement effect between 1991 and 2005 in the shallow (a) and deep (b) sandstone layers (Dinh et al., 2017b). Black circle indicates the blowout well.

5.2 Methodology

5.2.1 Case 1: Continuously supported gas expansion

I assume gas has penetrated within the recipient sandstones because the sandstones are permeable and because there are pressure differences caused by the blowout. The simplest model when the blowout pressure source is continuously supported is shown in Figure 5.3 as type A. With supporting gas, the pressure is constant and gas expands linearly with a constant velocity. In this cases, the linear migration rate v_{lin} can be easily estimated by:

$$v_{lin} = \frac{dL}{dT}, \tag{5.1}$$

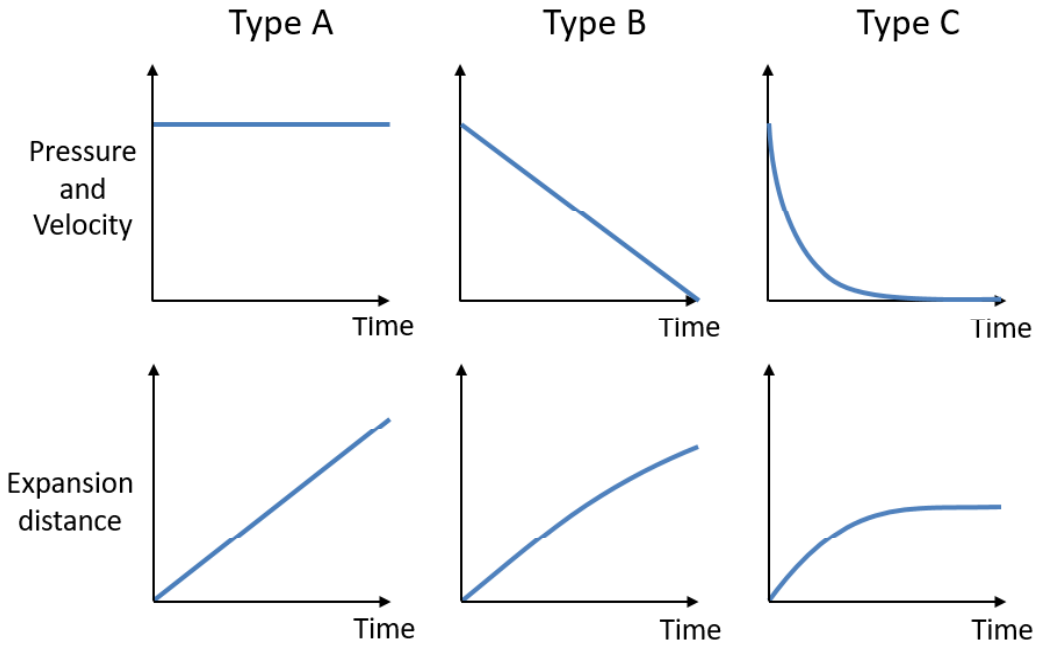

Figure 5.3: Model of gas expansion velocity and expansion distance according to the three pressure types within the same time interval. Top: three pressure types and their corresponding velocities. Starting pressures are identical in all 3 cases, and final pressures are identical in the last two cases. Bottom: the expansion distances of the three pressure scenarios with the same starting point. (A) a stable, continuous source maintains stable pressure and gas expands linearly with a constant velocity. (B — Darcy scenario) in a simple finite duration source case, gas migration velocity slows down linearly and the migration distance expands more slowly than type A. (C) when the source is finite with spatial spreading, the migration velocity dies out more quickly than type B, the expansion takes a longer time to happen than types B and A.

where dL and dT are the distance and duration of the gas migration.

5.2.2 Case 2: Discontinued support gas expansion

However, in this case study, because the well is closed after the blowout occurred, pressure is not likely to be supported (for example as modeled in Figure 2.8) and another relationship must be used to estimate gas migration velocity. Since natural gas is a common Newtonian fluid, Darcy's law (Darcy, 1856) is chosen to model its flow through the two porous sandstone layers. This relationship also stands behind the simulation model used by Langseth (2011).

The simplest form of Darcy's law assumes that viscous forces dominate

over inertial forces in porous media (Dake, 1983; Takhanov, 2011). In this case study, gas was charging into the main recipient sandstone at a moderate injection rate with much lower pressure than at the deeper reservoir pressure (about 9.5 MPa within the 828 m sandstone in January 1989 compared to 69 MPa at the well head when the blowout occurred). Therefore, I assume the inertial resistance coefficient is negligible. In addition, because the gas boundary in 1990 is far from the blowout well, this assumption is more valid in the later time frame (1991–2005). As illustrated in Figure 5.3 middle, when the source was discontinued, pressure reduced at a constant rate (type B) and so does the Darcy migration velocity. As a sequence, gas expansion slows down linearly with time.

Gas migration rate in the shallow sandstone

Using Darcy's law (Dake, 1983) for this case, the volumetric gas flow rate q (ft^3/day) through a cross-area A (ft^2) in the horizontal, shallow 495 m sandstone can be calculated as:

$$q = 5.615 \times 1.127 \times 10^{-3} \frac{\kappa A}{\eta} \frac{dP}{dL}, \tag{5.2}$$

where 5.615 is the cubic feet equivalent of one barrel; 1.127×10^{-3} is the conversion factor to imperial units; κ is the rock permeability (mD); η is the gas viscosity (cP). dP is the effective pressure difference (psi) between the two gas fronts along the horizontal movement axis (Figure 5.4 left). It is simply the difference between the pore pressure P_P (pushing gas) and the capillary resistance P_C (holding gas) calculated as (Muskat, 1949; Davis et al., 2011):

$$P_C = \frac{2\sigma \cos\theta}{r}, \tag{5.3}$$

where σ is the interfacial tension (dyne/cm), θ is the contact angle (degrees) and r is the radius of pore throat (μm).

The velocity of gas migration ($v_{Dar} = q/A$) in this sandstone can then be

inferred from Equation 5.2 as:

$$v_{Dar} = 5.615 \times 1.127 \times 10^{-3} \frac{\kappa}{\eta} \frac{dP}{dL}. \tag{5.4}$$

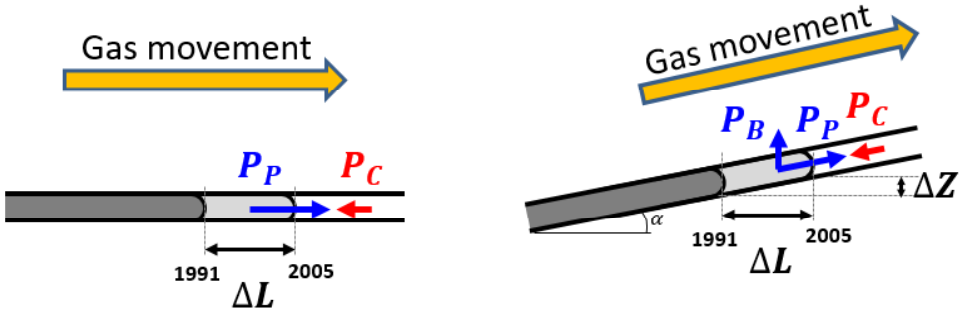

Figure 5.4: Three pressure components act in the shallow (left) and deep (right) layers: Pore pressure P_P, Capillary pressure P_C and Buoyancy pressure P_B. The capillary pressure opposes fluid movement which is governed by the pore pressure and the buoyancy pressure. In the horizontal shallow sandstone, there is no buoyancy effect.

Gas migration rate in the deep sandstone

In the lower 828 m sandstone, Equations 5.2 for flow rate and its derived velocity Equation 5.4 must be corrected for the dip. First of all, the numerator of the last term dP in Equation 5.2 becomes dP_{dip} (Dake, 1983):

$$dP_{dip} = dP + 0.4335\gamma dZ, \tag{5.5}$$

where γ is the fluid specific gravity (unitless) using pure water as a reference with a conversion factor of 0.4335 (psi/ft) and dZ is the vertical distance between the two gas fronts (ft).

In Equation 5.5, the term dP is still calculated along the gas movement axis. However, in the dipping sandstone, besides the pore pressure P_P and capillary resistance P_C, the effective pressure P is also affected by the buoyancy force P_B that corrects for the up dip migration (Figure 5.4):

$$P = P_P + P_B - P_C, \tag{5.6}$$

where the buoyancy pressure can be estimated by (Beaumont and Foster, 2000; Judd and Sim, 1998):

$$P_B = \Delta\rho h \sin\alpha, \tag{5.7}$$

where $\Delta\rho$ is the density contrast (g/cc) between gas and the formation fluid; h is the height of the gas column (ft) and α is the dip angle (degrees).

In the deep dipping sandstone, the capillary pressure counteracts the total effect of pore pressure and buoyancy pressure (Figure 5.4 right). On the other hand, in the horizontal shallow sandstone, the buoyancy pressure is omitted because the dip angle is zero (Equation 5.7).

Finally, the corrected form of the migration velocity (Equation 5.4) in this sandstone is:

$$v_{Dar} = 5.615 \times 1.127 \times 10^{-3} \frac{\kappa}{\eta} \frac{dP_{dip}}{dL}, \tag{5.8}$$

with the substitution of dP_{dip} from Equation 5.5.

5.2.3 Case 3: Discontinued support gas expansion with spatial spreading

In case of a non-continuous injection source resulting in nonlinear pressure changes (Figure 5.3, type C), e.g., due to the varying spatial spreading, gas migration velocity dies out more quickly than in type B to meet the same pressure value at the end of the time interval. As a result, the expansion distance increases more slowly than in type B. At the later stage of the time window, the velocity for type C approaches zero; gas expansion is slowly stopping.

In case of type C scenario, Darcy's law is only valid if the time window is divided into smaller intervals in which the pressure gradient is considered constant and Equations 5.4 and 5.8 can be applied step-wisely. Otherwise, these equations overestimate the migration velocity.

5.2.4 What is estimated?

In this case study, pressure type C is expected to be the most realistic scenario because the well was closed very soon after the blowout was detected. How-

ever, because of the sparsity of available time-lapse data (two intervals between 1989–1990 and one interval from 1991–2005), I are unable to use the step-wise approach mentioned above.

Instead, I calculate two types of gas migration rates: type A linear migration velocity v_{lin} (Equation 5.1) and type B simple Darcy migration velocity v_{Dar} (Equations 5.4 and 5.8). Although type C velocity with real spatial spreading is always smaller than type B, type B velocity can be close to type A if the pressure gradient is close to zero. Calculating and comparing both v_{lin} and v_{Dar} together are therefore useful to better understand real gas movement. Based on the data availability and the regional geology setting, the velocities are estimated along the Northeast-Southwest dipping direction in three different time intervals (these intervals also serve as dT in Equation 5.1): May 1989–July 1989, July 1989–March 1990, and 1991–2005 for the upper 495 m sandstone, and May 1989–September 1989, September 1989–May 1990, and 1991–2005 for the lower 828 m sandstone.

The procedure of calculating the two velocity types is summarized in Figure 5.5. The linear velocity v_{lin} is straightforward (Equation 5.1) with the observed lateral distance of gas movement (dL) in each time interval (dT) given above. On the other hand, for v_{Dar}, each input component of Equations 5.4 and 5.8 must be firstly determined (details in the next section). Then, from the typical interfacial tension σ and the contact angle θ between gas and water and the pore throat radius r, the capillary pressure P_C is calculated (Equation 5.3). Simultaneously, the buoyancy pressure P_B in the deep sandstone (Equation 5.7) can be estimated from the gas density contrast $\Delta\rho$, gas column height h and the dipping angle α. Combined with the pore pressure information P_P, the effective pressure differences are calculated for each sandstone layer (Equations 5.6 and 5.5). Finally, the Darcy velocities in each sandstone are calculated by using Equations 5.4 and 5.8.

5.3 Parameterization

In the previous section, I have outlined how the input parameters are used to calculate the linear velocity v_{lin} and the Darcy velocity v_{Dar} in each sandstone

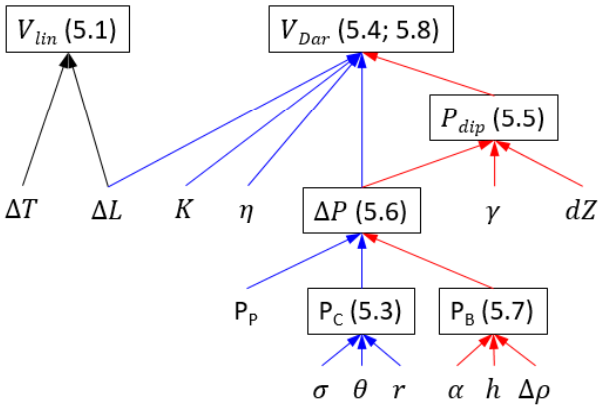

Figure 5.5: The workflow of estimating v_{lin} (black arrows) and v_{Dar} from all parameters. Blue and red arrows indicate v_{Dar} calculations for the shallow and the deep sandstones, respectively. Corresponding equations are numbered with rectangularized main parameters.

layer. The migration distance dL and the pore pressure component P_P are estimated from real data or other study results. Other remaining parameters are assumed properly or derived from the real case study geometry. These assumptions require me to use educated guesses to reduce uncertainties and to obtain reasonable estimates. The details how to estimate these parameters are described next.

First of all, the gas migration distances dL used in the main Equations 5.1, 5.4 and 5.8 are estimated directly from previous interpretation results. Particularly, as shown in Figure 5.6 where gas evolution from the original gas extension maps (Lie and Larsen, 1991, Figure 5.1) is overlaid on the time-lapse attenuation maps (Dinh et al., 2017b, Figure 5.2), the early migration distances (1989–1990) are estimated along the Northeast-Southwest direction (red arrows from the well).

Between 1991–2005, gas migration distances are estimated from the map of attenuation changes (Figure 5.2). In this time frame, pressure is believed to reduce in both sandstone layers because the well was closed early in January 1989. It is known from rock physics modeling that the total effective attenuation changes are governed by both changes in pressure and fluid saturation (Figure 5.7a). Attenuation is observed to decrease when pore pressure decreases (Figure 5.7b, blue curves). However, depending on the initial con-

dition, gas saturation may have different effects on attenuation. Dinh et al. (2015) observed that gas migration could be associated with both increased and decreased attenuation. This polarity switch is caused by a significant pore pressure decrease that may dominate the gas saturation change. Particularly, in the shallow sandstone, gas spreading to a new area creates the positive attenuation ring (Figures 5.2a, 5.7b left). On the other hand, gas spreading in the deeper sandstone to the Northeast creates the negative attenuation band (Figures 5.2b, 5.7b right). I assume for simplicity that the entire band of negative attenuation changes corresponds to the area of gas migration. Therefore, the gas migration distances from 1991–2005 in each sandstone are the widths of the positive ring and the negative band (also shown as red arrows in Figure 5.6).

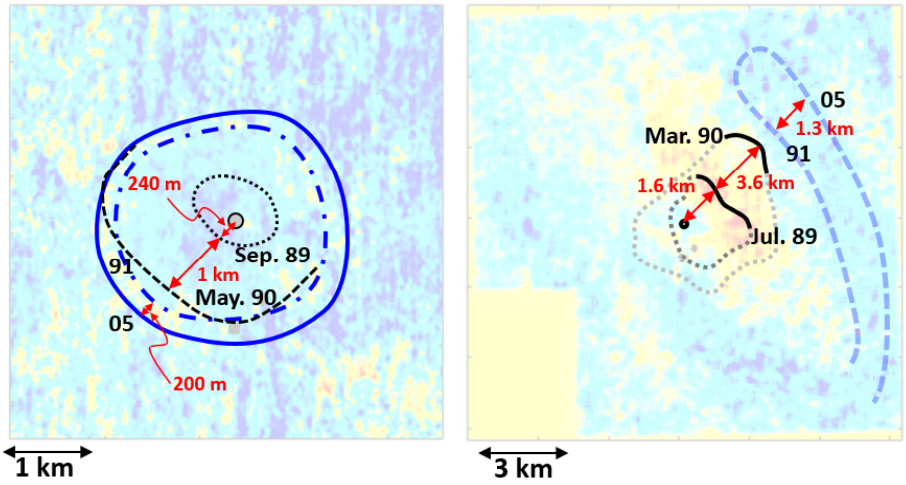

Figure 5.6: Example of travel distances (red arrows) measured at different time frames for the shallow (left) and deep (right) sandstones: the overlay of the gas extensions (Figure 5.1) superimposed on the time-lapse attenuation maps (Figure 5.2). I assume the increasing attenuation ring (in the shallow sandstone) and the reducing attenuation band (in the deep sandstone) indicate gas migration. The edges of these anomalies are assumed to be the gas fronts and used later to estimate pressure changes (Figure 5.9). Circle indicates the blowout well.

The next two parameters in Equations 5.4 and 5.8 are the rock permeability $\kappa = 1,000$ mD and the gas viscosity $\eta = 0.011$ cp. I use the permeability estimated from a reservoir simulation in the same target by Langseth (2011). The viscosity is experimentally estimated for a typical natural gas by Crane

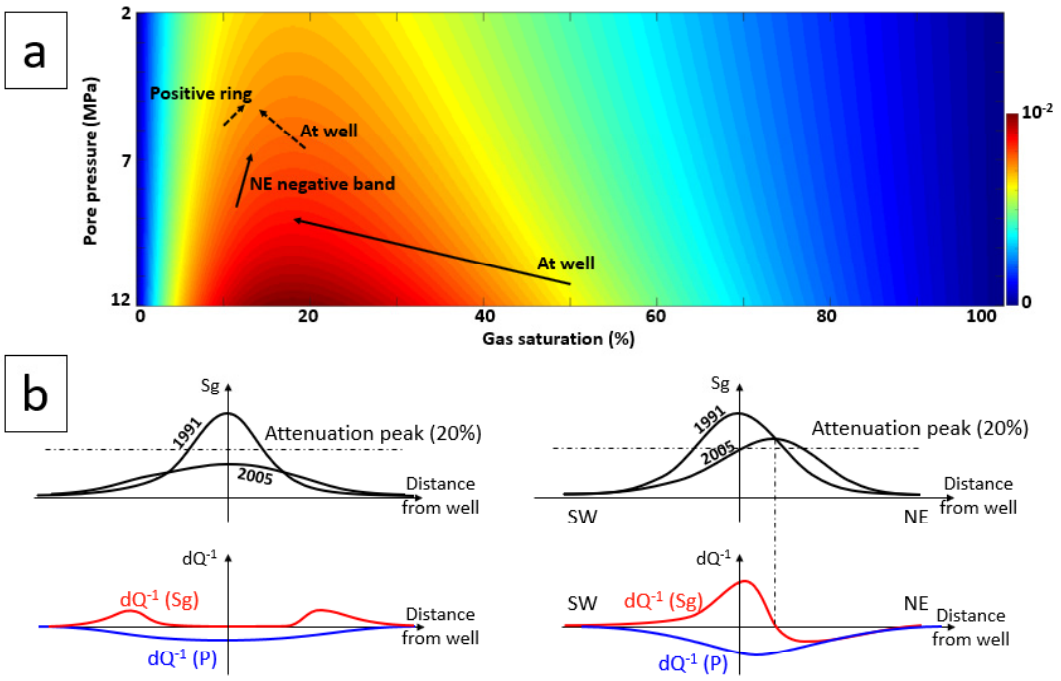

Figure 5.7: a) Pressure changes between 1991–2005 estimated from attenuation vs. pressure and saturation plot, edited from Dinh et al. (2015). Pressure reduction and saturation increase at the shallow sandstone (dotted arrows) cause the positive ring anomaly (Figure 5.2 a) and at the deep sandstone (solid arrows) cause the Northeast negative band anomaly (Figure 5.2b). b) A sketch of effects of changes in pressure (blue curves) and gas saturation (red curves) on the effective attenuation changes, edited from Dinh et al. (2015). Attenuation reduces with pore pressure. However, gas spreading in the shallow sandstone causes the positive attenuation ring, whereas gas spreading to the Northeast in the deep sandstone causes the negative attenuation band.

(2009).

The remaining inputs for the Darcy velocity equations are the changes in effective pressure dP, whereas effective pressure P is made up from the capillary resistance P_C, the buoyancy pressure P_B and the pore pressure P_P (Equation 5.6). When calculating the capillary pressure (Equation 5.3), I assume perfect water-wet condition for the contact angle, $\theta = 0^0$, a typical gas-water contact for the interfacial tension, $\sigma = 70$ dynes/cm (Rushing et al., 2008), and a typical radius of pore throat, $r = 20\ \mu m$, of sandstone (Nelson, 2009). With the buoyancy pressure in the deep sandstone (Equation 5.7), I assume the density contrast, $\Delta\rho = 1.0$ g/cc, between typical methane and water, fully charging over the whole sandstone thickness $h = 87$ m; the vertical gas mi-

gration, $dZ = 23$ m, and the dipping angle, $\alpha = 1^0$, are calculated from the structural interpretation of this sandstone (Figure 5.8). All these parameters can be easily found in Table 5.1.

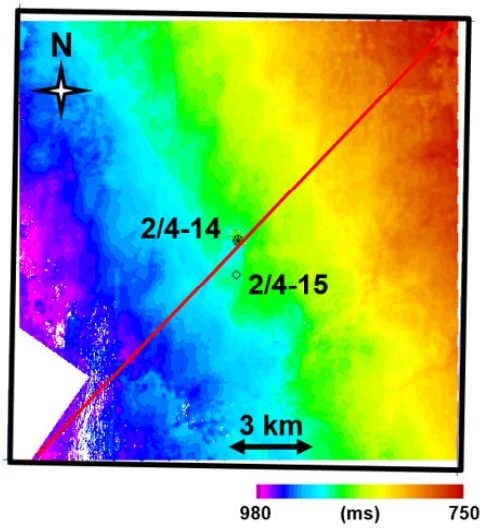

Figure 5.8: The dipping angle α in the deep sandstone is calculated as: $\alpha = \sin^{-1}(\frac{L}{Z})$, where L is the length measured along the diagonal direction (red line) from the seismic geometry, and Z is the depth difference converted from this time map assuming the average velocity of 2,000 m/s as Landrø (2011). The vertical gas migration distance dZ is therefore calculated as $dZ = dL \sin\alpha$ where dL is estimated from Figure 5.2. Edited from Dinh et al. (2017b)

The last term pore pressure P_P is taken from my inversion results (see also Chapter 4) and the simulation results by Langseth (2011). As mentioned previously in the estimation of gas migration distances dL (Figure 5.6), the gas front locations in 1991 and 2005 are the edges of the negative attenuation band (deep sandstone) and the positive attenuation ring (shallow sandstone). In the lower sandstone layer, the corresponding pressures at the positions of these edges are found from the inverted pressure results in Chapter 4 (Figure 5.9 left, black arrow). Because pore pressure is not inverted in the upper sandstone layer from 1991 to 2005, I use the simulation results by Langseth (2011). Using these results is reasonable because the model assumed the sandstone was flat, which is compatible with the real structure of this shallow sandstone. Similar to the interpolation approach presented in Chapter 4 (Initial conditioning of the Real example), I use the simulated pressures in 1989, 1990 and 1996 to predict pressures in 1991 and 2005 along the horizontal axis (Figure 5.9 right, purple

and green curves, respectively). Then, the pressure differences are estimated between two edges of the positive attenuation ring (Figure 5.9 right, black arrow).

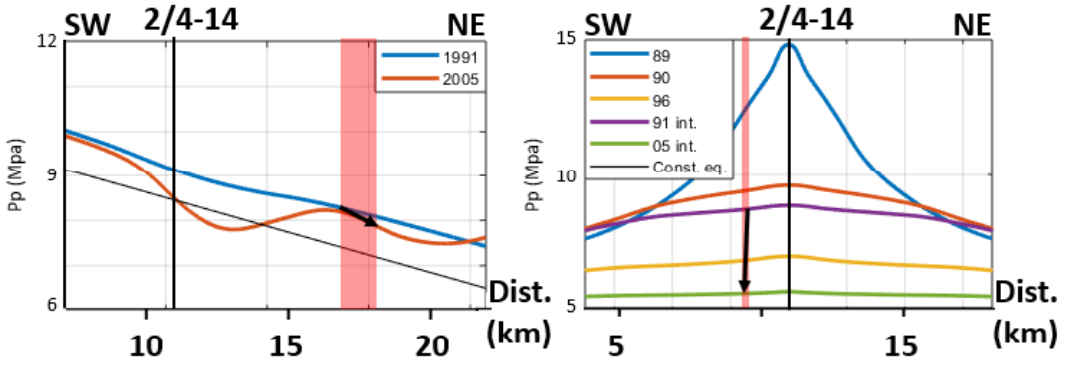

Figure 5.9: Pore pressure differences between 1991–2005 at the gas fronts estimated for the deep sandstone (left, edited from Chapter 4, Figure 4.15) and interpolated in the shallow sandstone from pressures in 1989, 1990 and 1996 (right, edited from Langseth, 2011). Black arrows indicate pressure changes from 1991 to 2005 at the gas fronts: the horizontal length of these arrows (red areas) matches the lateral gas expansion (the width of the positive ring at the shallow sandstone and the negative band at the deep sandstone) determined from Figure 5.6.

Between 1989 and 1990, I do not have comparative pressure information from the same source (maps of attenuation changes like Dinh et al., 2017b) that matches the time frame used when estimating gas migration distances dL (Figure 5.6). Therefore, I are only able to calculate the linear velocities v_{lin}. To have a relative comparison in the later time frame 1991–2005, besides the Darcy velocities v_{Dar}, I also calculate the linear velocities v_{lin}.

In our calculations, I convert all parameters from SI units to field units (Table 5.1). This step helps to avoid complex unit conversions because the units of the predefined parameters and those used in Darcy's Equations (5.4 and 5.8) are already in field units. The migration velocity results (in field units) are later converted back to SI units and presented in the next section.

Term	Value	Source
κ	1,000 mD	from reservoir simulation
η	0.011 cp	referenced methane
$\Delta\rho$	1 g/cc	referenced methane vs. water
α	1 degree	case study geometry
h	87 m	case study geometry
dZ	23 m	case study geometry
r	20 μm	typical sandstone
σ	70 dynes/cm	typical gas-water contact
θ	0 degree	perfect water-wet contact

Table 5.1: Final parameterization.

5.4 Results

Equations 5.3 and 5.7 in combination with the parameters in Table 5.1 suggest a capillary pressure of 12 kPa in both sandstones and a buoyancy pressure of 1.2 kPa in the deep sandstone. These calculations indicate pore pressure is the main force that governs gas movement, followed by capillary pressure in particular for the shallow sandstone.

From Figure 5.6 right, I interpret that the gas front moves approximately 1.3 km towards the Northeast between 1991 and 2005 in the deep sandstone layer (the width of the negative anomaly band). The corresponding pressure over time at the edges of this band is found to reduce by 0.5 MPa (Figure 5.9 left). This yields a gas movement rate of $v_{Dar} = 3.9$ m/year (Table 5.2), using Equation 5.4. This is substantially smaller than the linear rate prediction of $v_{lin} = 93$ m/year assuming constant spreading (Equation 5.1). On the other hand, the observed gas extensions of 1.6 km and 3.6 km after respectively 2 and 10 months (Lie and Larsen, 1991) suggests rates of $v_{lin} = 9.8$ km/year and 3.0 km/year in the deep sandstone (Table 5.2).

Similarly for the shallower layer, the 200 m radial extension from 1991 to 2005 (Figure 5.6 left) suggests a pressure reduction by 3.1 MPa between the gas fronts (Figure 5.9 right). These estimations indicate a movement of $v_{Dar} = 8.5$ m/year or $v_{lin} = 14$ m/year (Table 5.2). Conversely, at the start of the blowout, the gas front has extended 242 m and 1 km respectively within periods of 4 months and 12 months in 1989 and 1990 (Figure 5.1a and 5.6 left). This yields corresponding migration rates v_{lin} of 1.14 km/year and 726 m/year

Period	dP_p	dL	v_{Lin}	v_{Dar}
Deep sandstone				
May 1989–Jul 1989	N/A	1.6 km	9.8 km/year	
Jul 1989–Mar 1990	N/A	3.6 km	3.0 km/year	
1991–2005	0.5 MPa	1.3 km	93 m/year	3.9 m/year
Shallow sandstone				
May 1989–Sep 1989	N/A	242 m	726 m/year	
Sep 1989–May 1990	N/A	1 km	1.14 km/year	
1991–2005	3.1 MPa	200 m	14 m/year	8.5 m/year

Table 5.2: Inferred observations for pore pressure change dP_P, lateral migration length dL and estimated migration rates v_{lin}, v_{Dar} using Equations 5.1, 5.4 and 5.8, respectively.

in the shallow sandstone layer (Table 5.2).

Figure 5.10 shows that, for the deep sandstone, the computed linear rate v_{lin} (blue circles) is higher than the Darcy prediction v_{Dar} (orange circle). Given that Darcy rate v_{Dar} (type B) is likely an overestimation of the real gas migration rate (type C), this observation suggests even smaller gas movement over time (Figure 5.10 top, dashed circle). On the other hand, in the shallow sandstone, rates v_{lin} and v_{Dar} from 1991 to 2005 are similar. This suggests that pressure has decreased linearly in this time frame (Figure 5.10 bottom, dashed circle) and that the migration velocity is nearly zero by 2005.

After 16 years, gas migration has slowed down by two orders of magnitude with migration rate as high as 9.8 km/y in 1989 versus an average rate of 93 m/y between 1991 and 2005 for the deeper layer. The rate of 3.0 km/y between July 1989 and March 1990 suggests that the migration rate decays exponentially with time in this recipient sandstone (red curves in Figure 5.10).

5.5 Discussion

5.5.1 Case study results

From the calculated rates, I conclude that the largest volume of gas charged into the deep sandstone between 1989 and 1990 instead of the shallow sandstone because the highest expansion rate is observed in the deeper one (Figure 5.10 top).

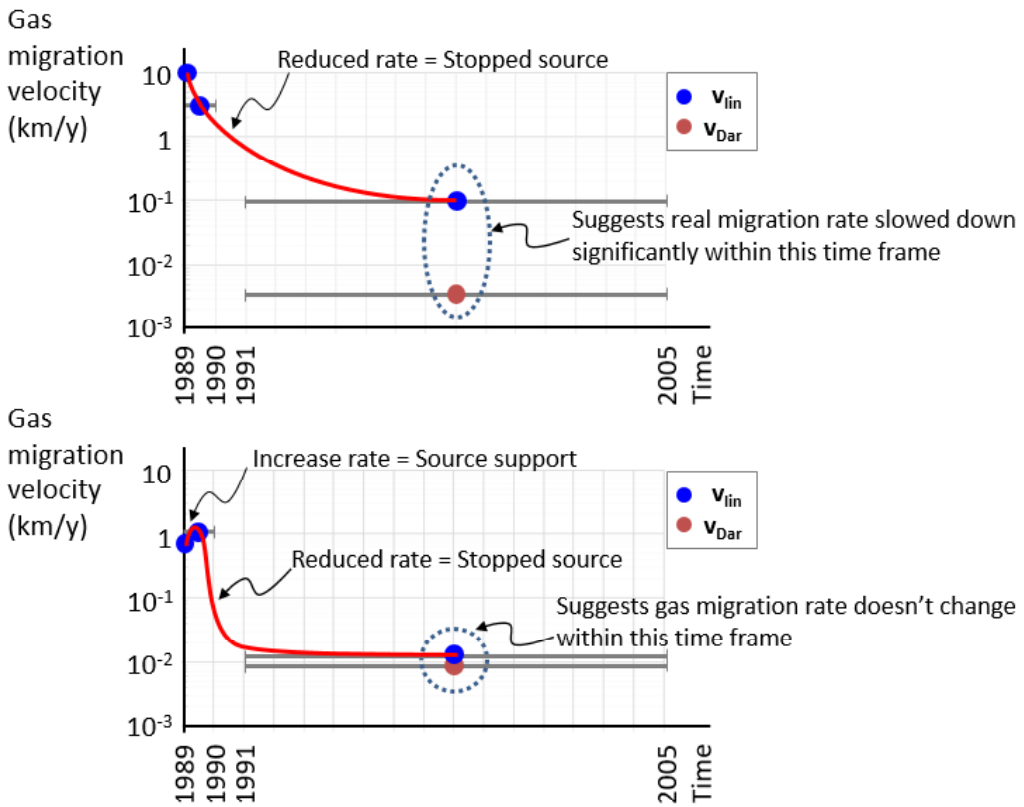

Figure 5.10: Gas migration velocities in the deep (top) and shallow (bottom) sandstone layers. Blue and orange circles represent v_{lin} and v_{Dar}, respectively. Red curves indicate an exponential decay in gas migration rates. Horizontal gray bars indicate periods of measurement for which migration velocities are calculated. Different migration behaviors in the early stages (1989–1990) of the two sandstone layers indicate no gas charging into the deep sandstone but more gas continued to leak into the shallow sandstone. In the later stage from 1991–2005, similar values of v_{lin} and v_{Dar} at the shallow sandstone suggest linear pressure decreasing and the values are close to the actual migration rate. On the other hand, the difference between v_{lin} and v_{Dar} at the deep sandstone suggests a slower actual gas migration.

It is possible that the volume of gas charging into the shallower layer increased in 1990 because of the rate acceleration between 1989 and 1990 (increased rate in Figure 5.10, bottom). This might indicate a change in the gas migration path from the source along the well bore. Indeed, other studies show evidence for later gas leakage into the shallow sandstone. Lie and Larsen (1991) found the first amplitude anomaly in this sandstone in September 1989, two months after the first deep sandstone detection. Langseth and Landrø (2012) found the first significant amplitude difference in the shallow sandstone in August 1990, 12 months after gas charging into the deep sandstone. Interestingly, similar possible changes in vertical flow path migration have also been suggested by Landrø (2011) when observing shallower amplitude difference anomalies close to the blowout well in the periods 1988–1990 and 1990–2009.

Furthermore, the slow gas movements in the last 14 years suggest that the original blowout source at depth is no longer active, eliminating gas supply from below the deep sandstone (Figure 5.10, the time interval from 1991–2005). I also eliminate the scenario that gas may leak from the deeper layer into the shallower one because the estimated pressure decreases in both sandstone layers except in the early time (1989–1990). In other words, gas continues to move within the two layers but no new gas charges into the formations. This is also supported by other studies. For example, Lie and Larsen (1991) stated that vertical gas migration had terminated in October 1990 and Landrø (2011) concluded that between 1991 and 2009, the sandstones contain the same amount of gas.

5.5.2 Case study parameterization

In this case study where pore pressure plays a dominant role, parameters r, σ, θ which determines the capillary resistance (Equation 5.3 and Table 5.1) do not have a significant impact on the Darcy rate v_{Dar}. Likewise, the used value for the viscosity of natural gas η is reasonable because of its small variations, even when temperatures are slightly different in these two sandstone layers. The factors that strongly influence our calculations are the permeability κ, the lateral path length dL, and the pore pressure change dP_P. Due to the

counteracting effects on attenuation between pressure and saturation, points of no changes in attenuation may still represent areas of changed gas saturation. This would change distance dL. For a more accurate estimation of dL and dP, I suggest using a proper rock physics model to get a better knowledge of both gas saturation and pore pressure (Dinh and van der Baan, 2017). In this case study, a doubling (or halving) of path length dL and pressure change dP_P only doubles (or halves) the estimated Darcy velocity v_{Dar}. Conversely, permeability can change by many orders of magnitude with typical values for non-tight sandstones ranging between 0.01–1000 mD. Indeed using a permeability of 0.1 D instead of 1 D for the deep sandstone leads to comparable estimates for the linear v_{lin} and Darcy v_{Dar} velocities.

During the calculation, I assume that gas is evenly distributed over the whole thickness of the homogeneous 828 m sandstone ($h = 78$ m, Table 5.1). However, due to limited data availability, the anisotropy of this layer is unknown and may vary both vertically and laterally. Gas may only accumulate at the top of the sandstone and actual estimations of this parameter may change accordingly. Nevertheless, this assumption only affect the buoyancy pressure which is relatively small compared to the main pore pressure component.

5.5.3 Case study theoretical assumptions

This example uses Darcy's law as the governing mechanism with a few assumptions that my over simplified model does not fully meet. They include:

- Incompressible fluids: Incompressibility guarantees the pressure gradient is distributed evenly along the fluid body and the migration velocity is linearly dependent on pressure gradient. In this case study, because gas is compressible, the application of Darcy's law may overestimate the migration velocity (Dake, 1983). This implies that the actual real gas migration rate from this blowout could be even slower than calculated. For justification, an adaptive Darcy's law with nonlinear parabolic relationship (the pressure difference is replaced by the difference of the squares of pressure) should be used to model the gas movement (Muskat and Botset, 1931; Basu and Singh, 1994).

- Linear-laminar flow (this assumption leads to piston-like fluid replace-

ment): However, in this case study, because of the viscosity differences between gas and brine, viscous fingering of the gas may occur through the brine phase. Also, lighter gas tends to accumulate and migrate along the ceiling of the sandstone layer (evidence for this can be seen in Figure 3.8 c,d). As the result, the flow may not be steady and Darcy's law no longer represents realistic gas migration behavior.

- 100% saturation of a single phase: However, I have a mixed fluid of gas and water with different viscosities. Plus, the pore pressures used in this model are derived from the inversion with a mixed phase fluid (Chapter 4). Assigning the effective pore pressure of the mixed fluid to the gas phase only may overestimate the pressure values and hence the migration velocity.

- No reaction between fluid and rock: This assumption is likely to hold in this case study because sandstone is good for hydrocarbon gas bearing. However, in cases of CO_2 sequestration (next section) there will likely be a reaction between the CO_2 and the rock.

Beside the assumptions mentioned above, it is known that the Darcy's law is valid to describe flow in porous media and fractures at low flow rates where the migration velocity and the pressure gradient have a linear relationship (Dake, 1983). This law assumes that viscous forces (Darcy component) dominate over inertial forces (non-Darcy component) in porous media. In this thesis, I assume the inertial resistance coefficient has reduced to a negligible magnitude after gas moved along the well and other formations before leaked into the sandstones. In the case when velocity and pressure gradient is not linearly dependent (for example, CO_2 sequestration), the Darcy velocity must be corrected for this non-Darcy component.

In the later time frame (1991–2005), because the pressure gradient is not likely to be constant over time and represents a type C source (Figure 2.8), the predicted Darcy's velocity (type B) is possibly an overestimation of the real migration rate. A more precise method can be done by dividing the interesting times into smaller intervals and assuming linear pressure changes in each of them. Nevertheless, this approach requires more measurements of pressure differences for every time intervals.

5.6 Implication for CO_2 sequestration

In CO_2 sequestration, this blowout case study is a useful example for project management to evaluate leakage risk because the supercritical carbon dioxide has gas-like properties. Similar to this blowout gas migration, when CO_2 enters a storage formation, its movement behavior can as a first order approximation be simply modeled by Darcy's law with the following assumptions: (1) no reaction between fluid and rock, and (2) slow CO_2 movement as a single fluid phase.

If I assume that the blowout gas is carbon dioxide and that the lower 828 m sandstone is an escape route to the sea floor. According to the structural geometry of this sandstone, the lateral distance to the leaking point is 42 km Northeast from the blowout well (as illustrated in Figure 5.11). Assuming the calculated migration rate of 3.9 m/year is maintained over time, I can anticipate that in the next 20 years, CO_2 would migrate updip for a lateral distance of 78 m and it would take approximately 10,800 years to reach the sea floor.

However, CO_2 may never reach the ocean bottom because of several reasons. Firstly, my velocity estimation ($v_{Dar} \ll v_{lin}$) suggests a slower actual migration rate and a type C source in which pressure reduces exponentially over time (see also Chapter 5). Plus, when migrating updip, the shallower fluid pressures are less. Therefore, gas migration rate is expected to be much smaller than 3.9 m/year. If the migration rate were not maintained, gas migration rates might slow down exponentially or even become zero.

Secondly, the estimated duration of 10,800 years is long enough for other sequestration mechanisms to take place. Using a numerical diffusion transport model, Balashov et al. (2013) have shown that in saline sandstone reservoirs, solubility trapping (the dissolution of CO_2 into brine) is dominant for the first 20 years. From 20 to 200 years after sequestration, both solubility and mineral trapping (the chemical reaction between CO_2 and sandstone mineral) are important. From 200 to 1,000 years and beyond, mineral trapping governs the sequestration mechanism. In another simulation, Zhang et al. (2009) have shown that capillary trapping only regulates the sequestration mechanism in a short period: after the first 20 years, rock pores trap about 3/4 of the total injected CO_2 (the remaining 1/4 amount of CO_2 is dissolved). After 800 years,

the CO_2 is held 10% by pores, 75% by dissolution, and 15% by mineral trapping. Although the initiation and intensity of geochemical reactions depend on the mineral composition of the rock, 10,800 years seem to be more than enough for them to occur. In this case, I conclude CO_2 would be absorbed and trapped for periods of time more closely related to geological timescales than human timescales.

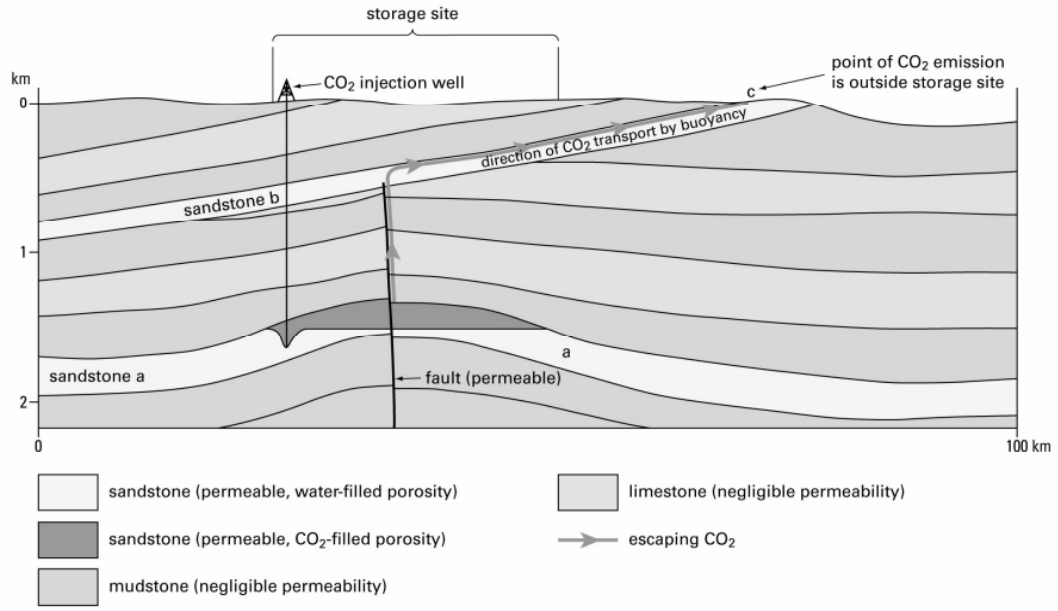

Figure 5.11: An illustration of the potential for leakage of CO_2 from a geological storage reservoir to occur outside the storage site, taken from Holloway et al. (2006).

5.7 Conclusions

In this chapter, I have shown that the Darcy's law can be adapted to estimate the blowout gas migration rate in the two shallow sandstone layers in different geological structures. Regarding the movement mechanism, my calculations indicate that the pore pressure gradient has more effect than the capillary and buoyancy pressure gradients in this case study. It is shown that in the first year after the blowout, gas has charged into the lower sandstone and moved vertically to the upper sandstone. In the next 14 years, there is no sign of supporting

influx from the deep source, and gas expansion in both sandstones is found to reduce exponentially with velocities less than 10 m/year. For underground CO_2 storage, the approach could be used to estimate how fast carbon dioxide moves and to evaluate the sequestration mechanism.

Chapter 6

Integrated interpretation

In this thesis, I have introduced the 1989 underground blowout in the North Sea area where gas has leaked into two recipient sandstone layers at 828 m and 495 m depths. Different studies had been conducted to understand the blowout development and to find out what gas migration had happened over time. However, due to the low repeatability of available data, the blowout still remains as a challenge with unanswered questions and disagreements between authors. As identified in Chapter 2, the main discussion topics for this case study are:

- the 4D feasibility of this project including the repeatability of the available data and the reliability of previous 4D signals observed around and near the well
- the vertical gas migration including communication between these shallow sandstones and the continuation of the blowout source
- the lateral gas migration including gas extension and pressure / fluid changes in the main recipients

In the previous chapters, I have presented my works to find the answers to these questions. In this chapter, I gather and integrate the results and contribute to better understand the blowout development.

6.1 Reprocessed data quality

It must be noted that the 4D signals are significantly improved with the proposed processing strategy (Chapter 3).

In the 2D surveys, the reprocessed outputs have better quality in terms of multiple removal and increased repeatability compared to the original data used by all previous works (Landrø, 2011; Langseth, 2011; Langseth and Landrø, 2012 and Bhakta and Landrø, 2014). This helps to eliminate some uncertainties and time-lapse noises observed on the old original surveys and is proven to improve later seismic-based analyses.

Particularly, at the shallow 495 m sandstone, the reprocessed 2D time-lapse image (Figure 3.4d) has answered some concerns when studying the original raw data used by Landrø (2011) (Figure 2.10). First of all, the absence of anomalies close to the well from the reprocessed data indicates that these anomalies observed by Landrø (Figure 2.10b) are artifacts in the raw-stack processing instead of the cement in the well (it was cemented all the way after the killing operation) because the cement would cause similar 4D effects even after reprocessing. As discussed by Landrø (2011), ship noise is prominent close to the well. This can be worsened by non-seismic activity on the rig and create 4D uncertainties around the well. In this thesis, other previously detected anomalies (at 610 ms, 670 ms) are now confirmed to be multiples and are attenuated after reprocessing.

Secondly, because the lateral extension of the 520 ms anomaly is less than that of the observed 650 ms anomaly in Landrø's image (Figure 2.10a), it cannot cause the wider 4D shadow effect on the lower 650 ms event. Therefore, I conclude that the 650 ms anomaly represents the gas migration within the 605 m sandstone from 1990–2009. I also believe that by 1990, gas has not moved within the 605 m sandstone or has moved very slowly that can only be detected effectively in a long enough time interval (for example, from 1990 to 2009 like Landro's image). This conclusion is based on the fact that gas was present in this sandstone before the blowout (Remen, 1991) and that my results do not show any significant 4D differences except for the 495 m sandstone between 1988–1990 (Figures 3.4d and 3.6).

The 4D image between 1988–1990 does not indicate a clear signal of gas ac-

cumulation in the deep sandstone (Figure 3.4d), which was previously addressed as the main challenge in other studies such as Landrø (2011) and Langseth (2011). The reason may come from the processing aspect that was unable to resolve the deep signal (Dinh et al., 2017b). In this thesis, I found that analyzing amplitude differences and time shifts is not the best practice to investigate this sandstone. Instead, examination of acoustic impedance seems to be a better approach as the gas presence is highlighted in this domain as shown in Figure 3.8. However, since this is just a single snapshot of the sandstone, its limitation is the inability to indicate gas movement over time. Under my evaluation, the gas migration in this sandstone in the early stage of the blowout is best studied by the works of Lie and Larsen (1991) and Remen (1991) (Table 2.1, Figure 2.7) in which more multiple 2D surveys were analyzed than in this thesis.

In the 3D dataset, although each individual survey was processed carefully, the poor 4D repeatability caused by unmatched processing routines is irreversible. My efforts to increase 4D matching have produced more meaningful time-lapse signals and attributes than before. For example, the map of seismic variance in the shallower part (Figure 3.11) has clearly indicated high noise contents affecting the image at the deep sandstone. This finding is consistent with the shallow tunnel valley system found by Haavik and Landrø (2014).

Now, understanding the deep signals are shadowed by strong footprints from the shallow features and the inline acquisition, the lower 828 m sandstone is a challenging sandstone as emphasized previously by Langseth (2011) and Langseth and Landrø (2012). Nevertheless, the newly calculated attributes (time shifts and attenuation changes in Figures 3.10 and 3.13) have enabled me to interpret the vertical and lateral migrations.

6.2 Vertical migration / Source influx

In this thesis, the vertical flow path remains unresolved. The only proposal for this mechanism is fractures around the wellbore caused by local build up pressure as suggested by Remen (1991). With this hypothesis, information about vertical migration and the source continuation can be clarified using the

estimated gas migration rates (Chapter 5).

Assuming the gas migration rate increases with pressure, Figure 5.10 shows that in the early stage (before 1991), after building up rapidly, the pressure in the deep sandstone has simply reduced (Figure 5.10). These long-term changes are found to agree with the pressure simulation from Remen (1991) (Figure 2.8). On the other hand, pressure increased first in the shallow sandstone before starting to reduce since 1991.

The first finding from these observations is the highest pressure found between 1989–1990 in the 828 m sandstone, which implies that vertical gas migration from the deep sandstone to the shallower one would have happened in this time period. However, exactly when is undetermined. Secondly, if the vertical migration mechanism is true, a new path is not created when pressure reduces. This implies that vertical migration to even shallower strata (shallower than 495 m) can happen only before 1991 when the pressure in the 495 m sandstone is highest. However, there is no other 4D signal observed in the 1988–1990 data (Figure 3.4d), not even at the nearest sandstone at 5 m above the 495 m sandstone (the 45 m thick sandstone at 445 m depth mentioned by Landrø (2011) and Langseth (2011)). Also, my time-shift image (Figure 3.4c) does not show significant anomalies shallower than the 495 m sandstone at 520 ms. Because I have pointed out earlier that the shallow 4D signals in Landro's image (Figure 2.10b) are probably raw-stack artifacts caused by the ship noise and the rig activities, these clean time-lapse observations on the reprocessed data and the migration rates suggest no gas leakage into shallow sandstones above 495 m. This opinion agrees with a similar conclusion from time-shift analysis by Landrø (2011).

From the interpretation above, I conclude that the vertical gas migration is less likely to occur above the 495 m sandstone. Therefore, the dimmed seismic amplitudes observed by Langseth (Figure 2.12) and by myself (Figure 3.9b) can be explained by major lateral gas movement in the strata, away from the well. The vertical migration, if it happened, was only a minor movement.

This mechanism also suggests that there is no continuous influx of gas from a deeper source. If there were gas support, the pressure in the deep sandstone would have maintained high, and between 1989–1990, both vertical and lateral

migration happened in the deep sandstone. The reduction of pressure in this sandstone would have started in a later time period which is not observed in Figure 5.10. Instead, I have found pressure reduced from early times on in the deep sandstone (1989–1990), coincident with the increasing pressure in the shallow sandstone. I interpret this as an exceeding local pressure in the deep sandstone which pushed gas up to the shallow sandstone. With reducing pressure, only lateral spreading along the strata is dominant because of higher horizontal than vertical permeability.

From 1991, I believe the vertical migration, from the 828 m sandstone to the 495 m sandstone and to the shallower ones if there is any, has stopped. This is observed in the reduction migration rates in both sandstones (Figure 5.10). I believe the termination of this vertical movement would be expected when the pressure in both sandstones started to reduce in May 1990 (Table 5.2), which is approximately around the same time proposed by Remen (1991) and is five months earlier than Lie and Larsen (1991).

According to the inversion results, the deep sandstone was slightly overpressurized in 2005 (Figure 4.15). I also believe that the pressure in the upper sandstone in the later time period (1991–2005) would have been even less overpressured, if not at the equilibrium hydrostatic state, because of two reasons (Figure 5.10). Firstly, the linear velocity and Darcy velocity are similar in the shallow sandstone between 1991–2005. This suggests that pressure difference is close to zero. Secondly, the build up pressure in the 495 m sandstone is at a much smaller magnitude than the 828 m one. Mild overpressure means that pressures in both sandstones are not high enough to cause further fractures to leak gas to upper layers. Instead, gas is trapped and slowly expanded laterally in the two strata. This is also supported by the observed expanding gas saturation over time (next section).

6.3 Lateral gas migration / Pressure vs. saturation results

The observed 4D signals (Figures 3.10b, 3.13), inversion results (Figure 4.15) and the lateral expansion rates (Figure 5.10) indicate that gas spreading was happening between 1991–2005 in both sandstone layers. Therefore I conclude that the lateral gas expansion has not stopped by October 1990 as suggested by Lie and Larsen (1991) and Langseth and Landrø (2012). The lateral gas migration in each sandstone is interpreted in detail below.

6.3.1 Shallow sandstone

After processing, gas charging into the 495 m sandstone is represented by the amplitude difference anomalies on the 2D line in Figure 3.4d. My results indicate gas extending 1.2 km around the blowout well. This matches with what has been found before by Lie and Larsen (1991), Landrø (2011) and Langseth (2011). My inverted reservoir conditions (Figure 4.13) are also similar to the reservoir simulation results by Langseth (2011) (Figure 2.13) and are in good agreement with the inversion results by Bhakta and Landrø (2014) (Figure 2.14). Despite different methods and initial conditions, my predictions show expected high gas accumulation (an increase of 25% at the well location in 1990) and pore pressure increase after the blowout. When integrating with other studies, my results clarify the challenges when Landrø (2011) tried to interpret time-lapse anomalies in this sandstone.

From the 3D surveys between 1991–2005, the circular amplitude anomaly extent increases by 200 m in radius. A similar anomaly is also observed in the calculated attenuation changes attribute (Figure 3.13). This suggests that gas has spread out laterally along the horizontal sandstone. These observations also agree with an independent interpretation of the same 3D volumes by Landrø (2014, personal communication). My estimation of migration velocity in this time frame is 8.5 m/year, significantly slower than the early stage of the blowout at 1.14 km/year (Table 5.2, Figure 5.10). The integration of all these findings indicates that in 14 years from 1991 to 2005, gas in the 495 m sandstone kept

spreading laterally slowly.

Regarding the termination of lateral migration in the 495 m sandstone by October 1990 suggested by Lie and Larsen (1991), other reservoir simulations and 3D amplitude analysis (Remen, 1991; Langseth, 2011; Langseth and Landrø, 2012) also left an open answer for this question because of the lack of information and evidence from the field data. In this thesis, my calculated migration rate is small (between 14–8.5 m/year) after May 1990 (Table 5.2, Figure 5.10). Therefore, unless the time-lapse interval is long enough (in this case, 16 years), lateral gas migration is likely not detectable in a short amount of time (5 months after May 1990 according to Remen (1991), Table 2.1). Therefore, I conclude that the lateral migration is still going on after October 1990, but with a very slow rate.

6.3.2 Deep sandstone

From the 2D data, I have noticed the presence of gas in the 828 m sandstone only from the AVO attributes in 1990. The deep signal from these data appears to be still difficult to analyze as found previously by Landrø (2011), Langseth (2011) and Langseth and Landrø (2012). However, from the 3D data, my thesis has brought the first interpretable images for this challenging sandstone. The two consistent attributes in Figures 3.10b and 3.13b (i.e., time shifts and time-lapse attenuation) have clearly indicated gas movement effects on the seismic responses.

Quantitatively, the inversion results of gas saturation and pore pressure have provided more interesting details and information when compared with previous reservoir simulation results by Langseth (2011) and Langseth and Landrø (2012). Although Langseth's simulation model was relatively simple in terms of the structure of the sandstone (which led to inaccurate pressure profiles that need to be dip corrected), it is a good start for my inversion conditioning. My inversion results indicate an expanding accumulation of gas between 1991 and 2005 (Figure 4.15), which is found to be highly compatible with the initial lateral extent estimated by Lie and Larsen (1991) (Figure 2.7). The main gas movement pattern is updip migration in the North–East direction, in good

agreement with previous structural interpretation.

Indeed, my lateral gas extent can be combined with that of Lie and Larsen (1991) (Figure 2.7) to give a reasonable extension rate shown in Table 5.2. Although the 1991–2005 gas extent distance is remarkable (more than 1.3 km to the Northeast), the migration velocity in this time interval is slow at 3.9 m/year, compared to 9.8 km/year at two months after the blowout (Figure 5.10). The movement, despite being slow, suggests that lateral migration is still continuous in the deep sandstone after 14 years. This opposes the anticipated termination after four months after well re-entering in May 1990 proposed by Lie and Larsen (1991). Since their study was carried out by analyzing seismic amplitudes from 2D repeated surveys (9 surveys roughly on a monthly basis in 1.5 years), I believe their conclusion results from the gas expansion (3.9 m/year) being smaller than the seismic resolution, combined with too short a time separation between these legacy surveys to detect gas migration reliably.

My inversion results have also provided the first image of pore pressure distribution in this sandstone between 1991–2005 (Figure 4.15). First of all, after dip correction, gas is found to move updip toward the Northeast, with maximum pressure reduction around the well. The pressure around this peak is reaching hydrostatic pressure, but still slightly overpressurized elsewhere. The maximum overpressure is 1 MPa at the Southwest, which is higher than Remen (1991)'s but lower than Langseth (2011)'s prediction.

The pressure reduction around the well (Figure 4.15) is also in good agreement with the image of attenuation changes (Figure 3.13b) and could indicate either lateral or vertical gas migration or both, away from the well. However, with the corresponding pressure reduction in the shallow sandstone in the same time interval (Figure 5.10 and Table 5.2), I interpret this pressure fade-out effect as evidence for the lateral gas migration only. Although possible vertical migration in the later time (after 1990) was raised by both Landrø (2011) (that vertical migration is less than lateral migration but not terminated) and Langseth and Landrø (2012), my integrated interpretation confirms the more preferable horizontal migration.

Chapter 7

Conclusions and suggested future research

7.1 Conclusions

At the beginning of this thesis, I have introduced the importance of time-lapse monitoring in reservoir management and the idea how it works via a simple subtraction analogy in the "Spot the differences" game for kids. Although the concept of subtraction is simple, there are yet many challenges in a time-lapse analysis. The first key point that needs to be focused is repeatability in acquisition and processing. It has been shown that repeatability determines the feasibility of a time-lapse project and should be planned carefully prior to data acquisition. Different derived time-lapse attributes and analysis methods have also been mentioned for meaningful interpretation. Besides the conventional time shifts and differences in amplitude, impedance, Vp/Vs ratio, I have given the less popular attribute of attenuation changes more attention as it theoretically contains useful information and has been successfully used before. To bring these attributes into play, qualitative and quantitative inversion methods have been developed to invert for changes in reservoir fluid saturation and pore pressure.

The goal of this thesis is to establish an adaptive workflow in analyzing legacy time-lapse data. It is shown that 4D reprocessing for repeatability im-

provement is crucial as the initial part prior to any time-lapse analysis. With the raw 2D seismic lines, I have found that the main problems are multiples and feathering effects. In-depth processing tests have concluded the best practice of combining SRME demultiple with predictive deconvolution and re-binning can resolve the issue. Attributes estimated from the reprocessed data are at a much higher quality and are promising for serious interpretation. With the more challenging processed 3D surveys, my only solution is to apply data re-binning. The inevitable shallow noise and acquisition footprints have limited time-lapse signals, but more careful tuning techniques can significantly improve the estimated attributes.

I have introduced a new yet simple inversion scheme to obtain changes in fluid saturation and pore pressure from time-lapse seismic attributes. The method involves setting up a thorough rock physics model and forward modeling workflow. I have extended the Pore space stiffness model and combined it with different models, namely the Random patchy saturation, the Batzle-Wang and Reuss's equations to establish a link between changes in pressure and saturation to changes in seismic attribute responses. The modeled attributes are displayed in 2D maps with respect to the two main variables: water saturation and pore pressure. The inversion solution is found by simply matching the measured attributes to the predicted ones.

I have applied this inversion scheme to the two recipient sandstone layers in the blowout case study and found reasonable distributions of pressure and gas saturation. Particularly, in the upper 495 m sandstone, local gas accumulation (increased by 25%) and build up pressure (increased by 5 MPa) are detected around the well in the early stage of the blowout (1988–1990). The uniform expansions of gas and pressure are between 1–1.2 km and in good agreement with the structure of this flat sandstone. These findings are compatible with previous studies. In the lower 828 m sandstone, my results indicate a reduction in both gas saturation and pore pressure from 1991 to 2005. I have found that gas has migrated towards the Northeast direction, following the updip structure of the sandstone. The new maximum gas concentration has reduced from 65% to 25% by 2005 and moved updip approximately 1 km away from the well where the pressure is found to be around the equilibrium hydrostatic state.

Beyond that location, the entire sandstone is remained slightly overpressurized by 2005. Regarding long-term monitoring, these new findings in the 828 m sandstone appear to be a reasonable extension to earlier studies.

This inversion approach has high flexibility in employing other rock physics models and time-lapse attributes. It also enables the user to visualize the solution space for uncertainty evaluation. This thesis has found that time-lapse attenuation is a very important attribute to be used in the analysis. This attribute conveys important independent information compared to conventional attributes (e.g., time shifts, amplitude changes) that help to stabilize the inversion performance.

With more available information about pore pressure, I have estimated the gas migration velocities in each sandstone layer using Darcy's law. My calculations show that one year after the blowout occurred, the gas spreading has slowed down significantly by two orders of magnitude within both sandstone layers. In the time frame between 1991 and 2005, gas has migrated as slowly as 9 m/year in the upper sandstone and 4 m/year in the lower sandstone. My in-depth interpretation from these observations suggests that the blowout has stopped and no longer charges more gas into the sandstones. Regarding the gas migration mechanism, both vertical and lateral migration are found to occur during the early stage of the blowout (before 1991). However, the lateral migration is more dominant in the later stage. In contrast to previous studies which suggested the termination of gas migration in 1990, my study has shown evidence of the continued lateral gas movement but with a exponentially decaying rate from 1991 to 2005.

7.2 Suggested future research

Despite the success in reprocessing and analyzing the legacy data, there is room for potential improvement in this legacy project.

Processing

As demonstrated in Chapter 3, time-lapse repeatability is the initial and crucial requirement for a successful time-lapse analysis. The following suggestions

are recommended to apply in a prestack parallel processing approach (Lumley et al., 2003) depending on the data availability. The purpose is to enhance 4D repeatability as well as to maintain seismic image signals.

- With the current existing 2D data, imaging the deep sandstone is the most difficult challenge. To address this target, seismic migration can be applied to improve the signals from this sandstone. Better preserved signals does not only improve 4D differenced amplitudes but also promises more information from seismic attributes.

- With the 3D data used in this study (acquired in 1991 and 2005), I strongly recommend to obtain the raw 3D volumes. Since the re-binning and 4D matching techniques help to improve the repeatability, it is strongly desirable to maximize time-lapse analysis by reprocessing the data. Similar to the 2D data (Chapter 3), shallow water demultiple algorithms must be applied. A quick, low-cost test on τ–p deconvolution is suggested. 3D surface related multiple elimination (SRME) can also be tested as a reasonable extension of the seabed multiple removal. However, because SRME may not work well in shallow water, its feasibility on the 3D data needs to be investigated (independently from the 2D test). When the performance of 3D SRME is limited, I suggest using shallow water demultiple methods (SWD) (Hung et al., 2014) or a combination of SWD and SRME (Wang et al., 2012). In order to tackle the possible overburden effects from the shallow tunnel valley system, I suggest improving the velocity model for better migration results at the deep sandstone. This can be obtained by using full-waveform inversion (FWI) or tomographic full-waveform inversion (TFWI) (Biondi and Almomim, 2013).

- In order to obtain more detailed monitoring, reprocessing other 2D surveys (for example, line 602 in 2009, and other surveys of line 804) is recommended. The availability of these data is confirmed by Lie and Larsen (1991), Remen (1991) and Landrø (2011). Analyzing line 804 data (perpendicular to line 602) in similar time frames will introduce more angles to the study, while using data at other time intervals will bring more

understanding to the blowout development. With these data, a similar approach that I have used to line 602 (Chapter 3) can be applied.

4D attributes and inversion

Most of my recommendations in 4D attributes and inversion for this case study involve the extension of time-lapse attributes and inversion techniques. The main goal is to independently compare the results from different approaches to reduce the uncertainty when evaluating the condition changes in the two recipient sandstone layers.

- I suggest performing 4D AVO analysis if prestack seismic data are available. Because the seismic responses at non-zero offsets contain S-wave information, a 4D AVO study can reveal the fluid changes without a full time-lapse inversion. Moreover, prestack data provide more attributes that can be used as the input for different inversion methods.

- In case that multicomponent seismic data are available, I suggest a separate 4D inversion, for example, using PP-PS data (Landrø et al., 2003) or P- and S-wave time shifts (Trani et al., 2011). Using the shear component, which is recorded directly from the field instead of being calculated during prestack PP inversion, would increase the input quality for the later time-lapse inversion.

- When the AVO attributes are available (mentioned above), various existing time-lapse inversion approaches can be performed. Different inputs can be used, for example, using changes in Intercept and Gradient (Landrø, 2001), P- and S-impedances (Tura and Lumley, 1999), Vp/Vs ratio and P-impedances (Andersen et al., 2009). These attributes can also be inverted using my grid-search inversion method with a proper rock physics model.

- When there is no further data for this case study, my proposed inversion method is applicable in other hydrocarbon fields where more petrophysical data are available. With more information on reservoir conditions, the inversion uncertainties are lessened.

CO_2 sequestration

- The method to calculated gas migration in Chapter 5 is simple and is encouraged to be applied in other case studies. The Frio project (Hovorka et al., 2003) — a pilot CO_2 sequestration experiment in Texas (U.S.A.) — could be a good candidate. The main storage sandstone has similar settings to the 828 m sandstone: high porosity (35%), high permeability (2 D), a thickness of 23 m and a typical dip of 17^0 south. However, the actual injection configurations are different in depth, temperature, pressure, duration and rate. Therefore, CO_2 plume migration must be computed carefully.

- In this study, if CO_2 actually moves within the two sandstone layers as slowly as computed in Chapter 5, both sandstones can be turned into carbon dioxide storage. The abandoned blowout well can be reused in a CO_2 sequestration project. It can be reentered, side tracked and perforated during monitoring, at a lower cost than drilling new wells. However, because it may act as a direct pathway to the sea floor, the filled cement should be investigated to avoid leakage. In addition, the spatial distribution of reservoir properties (realistic temperature, pressure, porosity, viscosity, permeability) should be obtained before predicting the actual CO_2 migration rate.

Bibliography

Andersen, C. F., V. Grosfeld, A. V. Wijngaarden, and A. N. Haaland, 2009, Interactive interpretation of 4d prestack inversion data using rock physics templates, dual classification, and real-time visualization: The Leading Edge, **28**, 898–906.

Bakken, B., 1991, Casing materials and an alternative casing design: Technical Report 134-140, 2/4-14 Experience Transfer Seminar, Saga Petroleum A.S.

Balashov, V. N., G. D. Guthrie, J. A. Hakala, C. L. Lopano, and J. D. Rimstidt, 2013, Predictive modeling of co2 sequestration in deep saline sandstone reservoirs: Impacts of geochemical kinetics: Applied Geochemistry, 41–56.

Barkved, O. I., 2012, Seismic surveillance for reservoir delivery: From a practitioner's point of view: EAGE Publication B.V., Education tour series 6.

Barton, N., 2007, Rock quality, seismic velocity, attenuation and anisotropy: Taylor & Francis /Balkema.

Basu, A., and R. N. Singh, 1994, Comparison of darcy's law and fick's law of diffusion to determine the field parameters related to methane gas drainage in coal seams: International Mine Water Association Proceedings 1994, 59–70.

Batzle, M., and Z. Wang, 1992, Seismic properties of pore fluids: Geophysics, **57**, 196–1408.

Beaumont, E. A., and N. H. Foster, 2000, Handbook of petroleum geology: Exploring for oil and gas traps: AAPG Treatise of Petroleum geology.

Bekara, M., and M. van der Baan, 2010, High-amplitude noise detection by the expectation-maximization algorithm with application to swell-noise attenuation: Geophysics, **75**, V39–V49.

Bhakta, T., and M. Landrø, 2014, Estimation of pressure-saturation changes for unconsolidated reservoir rocks with high vp/vs ratio: Geophysics, **79**,

M35–M54.

Biondi, B., and A. Almomim, 2013, Tomographic full-waveform inversion (tfwi) by combining fwi and wave-equation migration velocity analysis: The Leading Edge, **32**, 1074–1080.

Biot, M. A., 1956, Theory of propogation of elastic waves in a fluid-saturated porous solid – i. low-frequency range: The Journal of the acoustical society of America, **28(2)**, 168–179.

Blanchard, T. D., 2011, Time-lapse seismic attenuation as a tool for monitoring hydrocarbons and CO_2 in geological materials: PhD thesis, The University of Leeds.

———, 2014, Robust observations of changes in time-lapse attenuation: measurement and possible application: SEG Technical Program Expanded Abstracts 2014, 4950–4954.

Blanchard, T. D., R. Clark, and B. Kurmashov, 2010a, P-wave attenuation as an additional tool for monitoring CO_2 injection sites: SEG Technical Program Expanded Abstracts 2010, 4252–4256.

Blanchard, T. D., R. Clark, and M. van der Baan, 2010b, Separating pressure and saturation changes using seismic attenuation: SEG Technical Program Expanded Abstracts 2010, 4242–4246.

Blanchard, T. D., and P. Thore, 2013, Introducing prior information to pressure and saturation inversion: the key for success?: SEG Technical Program Expanded Abstracts 2013, 4971–4975.

Bysveen, J., 1991, Top intervention snubbing operations speccial equipment fishing lessons: Technical Report 141-159, 2/4-14 Experience Transfer Seminar, Saga Petroleum A.S.

Calvert, R., 2005, Insights and methods for 4d reservoir monitoring and characterization: Distinguished instructor short course series 8: SEG and EAGE.

Castagna, J. P., M. L. Batzle, and R. L. Eastwood, 1985, Relationships between compressional-wave and shear-wave velocities in clastic silicate rocks: Geophysics, **50**, 571–581.

Castagna, J. P., and S. W. Smith, 1994, Comparison of avo indicators: A modeling study: Geophysics, **59**, 1849–1855.

Chen, Q., and S. Sydney, 1997, Seismic attributes technology for reservoir

forecasting and monitoring: The Leading Edge, **16**, 445–448.

Ciz, R., and S. A. Shapiro, 2007, Generalization of gassmann equations for porous media saturated with a solid material: Geophysics, **72(6)**, A75–A79.

Cole, S., D. Lumley, M. Meadows, and A. Tura, 2002, Pressure and saturation inversion of 4d seismic data by rock physics forward modeling: SEG Technical Program Expanded Abstracts 2015, 2475–2478.

Crane, 2009, Flow of fluids through valves, fittings, and pipe: Technical paper no. 410: Technical report, Crane Company.

Dake, L. P., 1983, Developments in petroleum science: Volume 8: Fundamental of reservoir engineering: Elsevier B.V.

Darcy, H., 1856, Les fontaines publiques de la ville de dijon: Victor Dalmont.

Dasgupta, R., and R. A. Clark, 1998, Estimation of q from surface seismic reflection data: Geophysics, **63**, 2120–2128.

Davis, J. S., I. Belien, X. Liu, and S. Dougherty, 2011, Modelling gas migration, distribution, and saturation in a structurally and petrologically evolving tight gas reservoir: International petroleum technology conference, 14621.

Dinh, N. H., and M. van der Baan, 2017, A grid-search approach for 4d pressure-saturation discrimination: Geoconvention 2017.

Dinh, N. H., M. van der Baan, and M. Landrø, 2015, Integrated time-lapse analysis of shallow gas movement: SEG Technical Program Expanded Abstracts 2015, 5503–5507.

———, 2017a, Estimation of shallow gas-migration rates after a subsurface blowout using time-lapse attributes: SEG Technical Program Expanded Abstracts 2017, 1882–1886.

———, 2017b, Processing and quality-control strategies for consistent time-lapse seismic attributes: A case history on an internal blowout using vintage data: Geophysics, **82**, B135–B146.

Dinh, N. H., M. van der Baan, and B. H. Russell, 2016, Pore space stiffness approach for a pressure-dependent rock physics model: SEG Technical Program Expanded Abstracts 2016, 3226–3230.

Dragoset, B., E. Verschuur, I. Moore, and R. Bisley, 2010, A perspective on 3d surface-related multiple elimination: Geophysics, **75**, 75A245–75A261.

Duffault, K., and M. Landrø, 2007, Vp/vs ratio versus differential stress and

rock consolidation: A comparison between rock models and time-lapse avo data: Geophysics, **72**, C81C94.

Dvorkin, J., G. Mavko, and A. Nur, 1995, Squirt flow in fully saturated rocks: Geophysics, **60**, 97–107.

Dvorkin, J., and A. Nur, 1996, Elasticity of high-porosity sandstones: Theory for two north sea data sets: Geophysics, **61(5)**, 1363–1370.

Eiken, O., G. U. Haugen, M. Schonewille, and A. Duijndam, 2003, A proven method for acquiring highly repeatable towed streamer seismic data: Geophysics, **68**, 1303–1309.

Elboth, T., H. Qaisrani, and T. Hertweck, 2008, De-noising seismic data in the time-frequency domain: SEG Technical Program Expanded Abstracts 2008, 2622–2626.

Floricich, M., C. MacBeth, J. Stammeijer, R. Staples, A. Evans, and C. Dijksman, 2006, A new technique for pressure - saturation separation from time-lapse seismic—schiehallion case study: 76th EAGE Conference and Exhibition, Extended abstract, E017.

Floricich, M., C. MacBeth, and R. Staples, 2005, An engineeringdriven approach for separating pressure and saturation using 4d seismic: application to a jurassic reservoir in the uk north sea: SEG Technical Program Expanded Abstracts 2005, 2464–2467.

Gassmann, F., 1951, Über die elastizitat poroser medien: Vier. der Natur. Gesellschaft Zurich, **96**, 1–23.

Gurevich, B., D. Makrarynska, O. Bastos de Paula, and M. Pervukhina, 2010, A simple model for squirt-flow dispersion and attenuation in fluid-saturated granular rocks: Geophysics, **75(6)**, N109–N120.

Haavik, K. E., and M. Landrø, 2014, Iceberg ploughmarks illuminated by shallow gas in the central north sea: Quaternary Science Reviews, **103**, 34–50.

Hampson, D. P., B. H. Russell, and B. Bankhead, 2005, Simultaneous inversion of prestack seismic data: SEG Technical Program Expanded Abstracts 2005, 1633–1637.

Han, D., 1986, Effects of porosity and clay content on acoustic properties of sandstones and unconsolidated sediments: PhD thesis, Stanford University.

Han, D., A. Nur, and D. Morgan, 1986, Effects of porosity and clay content on

wave velocities in sandstones: Geophysics, **51**, 2093–2017.

Holloway, S., A. Karimjee, M. Akai, R. Pipatti, and K. Rypdal, 2006, Ipcc guidelines for national greenhouse gas inventories. vol. 2, energy, chapter 5, carbon dioxide transport, injection and geological storage: Institute for Global Environmental Strategies.

Hovorka, S. D., M. H. Holtz, S. Sakurai, P. R. Knox, D. Collins, P. Papadeas, and D. Stehli, 2003, Frio pilot in co2 sequestration in brine-bearing sandstones: Technical Report 03-04, Gulf Coast Carbon Center.

Hugonnet, P., and P. Lecocq, 2003, Srme variations partial srme and hybrid srme-radon: 65th EAGE Conference and Exhibition, Extended abstract, P191.

Hung, B., M. Wang, K. Yang, and X. Wu, 2014, Enhanced internal multiple attenuation in shallow water environment: SEG Technical Program Expanded Abstracts 2014, 4147–4151.

Jack, I., 1998, Time-lapse seismic in reservoir management: Distinguished instructor short course series 1: SEG.

Johnston, D. H., 2013, Practical applications of time-lapse seismic data: SEG Distinguished Instructor Series No. 16.

Judd, A. G., and R. H. Sim, 1998, Shallow gas migration mechanisms in deep water sediments, offshore site investigation and foundation behavior "new frontiers": The Society for Underwater technology conference, 22–24.

Kang, I. B., and G. A. McMechan, 1994, Separation of intrinsic and scattering q based on frequency-dependent amplitude ratios of transmitted waves: Journal of Geophysical Research, **99(B12)**, 23875–23885.

Kasahara, J., and Y. Hasada, 2017, Time lapse approach to monitoring oil, gas and c02 storage by seismic methods: Elsevier.

Klimentos, T., and C. McCann, 1990, Relationships among compressional wave attenuation, porosity, clay content, and permeability in sandstones: Geophysics, **55**, 998–1014.

Koesoemadinata, A. P., and G. A. McMechan, 2001, Empirical estimation of viscoelastic seismic parameters from petrophysical properties of sandstone: Geophysics, **66**, 1457–1470.

Kragh, E., and P. Christie, 2002, Seismic repeatability, normalized rms and

predictability: The Leading Edge, **21**, 640–647.

Landrø, M., 1999, Repeatability issues of 3-d vsp data: Geophysics, **64**, 1673–1679.

———, 2001, Discrimination between pressure and fluid saturation changes from time-lapse seismic data: Geophysics, **66**, 869–844.

———, 2010, 4d seismic, *in* Petroleum Geosciences: From Sedimentary Environments to Rock Physics, Bjørlykke, K. ed.: Springer-Verlag Berlin Heidelberg.

———, 2011, Seismic monitoring of an old underground blowout 20 years later: First Break, **29**, 39–48.

Landrø, M., and J. Stammeijer, 2004, Quantitative estimation of compaction and velocity changes using 4d impedance and traveltime changes: Geophysics, **69**, 949–957.

Landrø, M., H. H. Veire, K. Duffaut, and N. Najjar, 2003, Discrimination between pressure and fluid saturation changes from marine multicomponent time-lapse seismic data: Geophysics, **68**, 1592–1599.

Langseth, E., 2011, 4d interpretation of gas migration in shallow sand layers - compared to reservoir simulation: Master's thesis, Norwegian University of Science and Technology.

Langseth, E., and M. Landrø, 2012, Time-lapse 2d interpretation of gas migration in shallow sand layers - compared to reservoir simulation: International Journal of Greenhouse Gas Control, **10**, 389–396.

Lie, A., and D. O. Larsen, 1991, Monitoring of an underground flow in well 2/4-14 by shallow seismic data: Technical Report 45-63, 2/4-14 Experience Transfer Seminar, Saga Petroleum A.S.

Lumley, D., D. C. Adams, M. Meadows, S. Cole, and R. Wright, 2003, 4d seismic data processing issues and examples: SEG Technical Program Expanded Abstracts 2003, 1394–1397.

MacBeth, C., J. Soldo, and M. Floricich, 2004, Going quantitative with 4d seismic: SEG Technical Program Expanded Abstracts 2004, 2283–2286.

Mavko, G., and D. Jizba, 1991, Estimating grain scale fluid effects on velocity dispersion in rocks: Geophysics, **56**, 1940–1949.

Mavko, G., and T. Mukerji, 1995, Seismic pore space compressibility and gassmann's relation: Geophysics, **60**, 1743–1749.

Mavko, G., T. Mukerji, and J. Dvorkin, 2009, The rock physics handbook, 2nd ed.: Cambridge University Press.

Mindlin, R. D., 1949, Compliance of elastic bodies in contact: Journal of Applied Mechanics, **16**, 259–268.

Mjelde, Ø., and P. Bakøy, 1991, Geology, pressure prognosis and status of knowledge, rock mechanics: Technical Report 5-19, 2/4-14 Experience Transfer Seminar, Saga Petroleum A.S.

Moraes, F., and C. MacBeth, 2005, Saturation and pressure inference from velocity and density: 9th International Congress of the Brazilian Geophysical Society & EXPOGEF, 1297–1300.

Müller, T. M., and B. Gurevich, 2004, One-dimensional random patchy saturation model for velocity and attenuation in porous rocks: Geophysics, **69**, 1166–1172.

Müller, T. M., B. Gurevich, and M. M. Lebvedev, 2010, Seismic wave attenuation and dispersion resulting from wave induced flow in porous rocks: Geophysics, **75(5)**, 75A147–75A164.

Müller, T. M., and S. A. Shapiro, 2001, Seismic scatterinig attenuation estimates from the german ktb area derived from well-log statistics: Geophysical Research Letter, **28**, 3761–3764.

Murphy, W. F., 1982, Effects of microstructure and pore fluids on acoustic properties of granular sedimentary materials: PhD thesis, Stanford University.

Murphy, W. F., A. Reischer, and K. Hsu, 1993, Modulus decomposition of compressional and shear velocities in sand bodies: Geophysics, **58**, 227–239.

Muskat, M., 1949, Calculation of initial fluid distributions in oil reservoirs: SPE, **949119-G**.

Muskat, M., and H. G. Botset, 1931, Flow of gas through porous materials: Journal of Applied Physics, **27**, 27–47.

Nelson, P. H., 2009, Pore-throat sizes in sandstones, tight sandstones, and shales: AAPG bulletin, **93**, 329–340.

Ødegaard, E., and P. Avseth, 2003, Interpretation of elastic inversion results using rock physics templates: 65th EAGE Conference and Exhibition, Extended abstract, E17.

Pride, S., J. Berryman, and J. Harris, 2004, Seismic attenuation due to wave induced flow: Journal of Geophysical Research, **109**, 1–19.

Reine, C., R. Clark, and M. van der Baan, 2012a, Robust prestack q-determination using surface seismic data: Part 1 - 3d case study: Geophysics, **77**, B1–B10.

———, 2012b, Robust prestack q-determination using surface seismic data: Part 1 - method and synthetic examples: Geophysics, **77**, R45–R56.

Reine, C., M. van der Baan, and R. Clark, 2009, The robustness of seismic attenuation measurements using fixed- and variable-window time-frequency transforms: Geophysics, **74**, WA123–WA135.

Remen, A., 1991, Flow paths and shallow gas migration: Technical Report 64-82, 2/4-14 Experience Transfer Seminar, Saga Petroleum A.S.

Reuss, A., 1929, Berechnung der fliessgrenzen von mischkristallen auf grund der plastizitätsbedingung für einkristalle: Zeitschrift für Angewandte Mathethamik und Mechanik, **9**, 49–58.

Ross, C. P., G. B. Cunningham, and D. P. Weber, 1996, Interactive interpretation of 4d prestack inversion data using rock physics templates, dual classification, and real-time visualization: The Leading Edge, **15**, 1233–1249.

Rushing, J. A., K. E. Newsham, K. C. Van Fraassen, S. A. Mehta, and G. R. Moore, 2008, Laboratory measurements of gaswater interfacial tension at hp/ht conditions: SPE, **114516**.

Russell, B. H., 2013, A gassmann-consistent rock physics template: Technical report, CSEG Recorder.

———, 2014, Prestack seismic amplitude analysis: An integrated overview: Interpretation, **2**, SC19–SC36.

Russell, B. H., and T. Smith, 2007, The relationship between dry rock bulk modulus and porosity – an empirical study: Technical Report 19, CREWES Research Report.

Selmer, J., 1991, Safety analysis, techniques, practices and results during operations: Technical Report 119-133, 2/4-14 Experience Transfer Seminar, Saga Petroleum A.S.

Slungaard, C., 1991, Noise and temperature logging to determine underground flowpaths. scaling and chemistry: Technical Report 20-37, 2/4-14 Experience

Transfer Seminar, Saga Petroleum A.S.

Smith, G. C., and P. M. Gidlow, 1987, Weighted stacking for rock property estimation and detection of gas: Geophysical Prospecting, **25**, 993–1014.

Takhanov, D., 2011, Forchheimer model for non-darcy flow in porous media and fractures: Master's thesis, Imperial College London.

Tary, J.-B., R. H. Herrera, J. Han, and M. van der Baan, 2014, Spectral estimation - what is new? what is next?: Reviews of Geophysics, **52**, 723–749.

Toksöz, M. N., D. H. Johnston, and A. Timur, 1979, Attenuation of seismic waves in dry and saturated rocks: laboratory measurements: Geophysics, **44**, 681–690.

Tonn, R., 1991, The determination of the seismic quality factor q from vsp data: A comparison of different computational methods: Geophysical Prospecting, **39**, 1–27.

Trani, M., R. Arts, O. Leeuwenburgh, and J. Brouwer, 2011, Estimation of changes in saturation and pressure from 4d seismic avo and time-shift analysis: Geophysics, **76**, C1–C17.

Tura, A., and D. E. Lumley, 1999, Estimating pressure and saturation changes from time-lapse avo: SEG Technical Program Expanded Abstracts 1999, 1655–1658.

Van der Baan, M., 2001, Acoustic wave propagation in one-dimensional random media: The wave localization approach: Geophysical Journal International, **145**, 631–646.

———, 2002, Constant Q and a fractal, stratified earth: Pure and Applied Geophysics, **159**, 1707–1718.

Verschuur, D. J., 2006, Seismic multiple removal techniques: Past, present and future: EAGE Publication BV.

Wang, H., Y. Sun, S. Boyer, G. Yu, J. Stein, and S. Van Reenen, 2012, Enhanced shallow water demultiple technology: SEG Technical Program Expanded Abstracts 2017, 1–5.

White, B., P. Sheng, and B. Nair, 1990, Localization and backscattering spectrum of seismic waves in stratified lithology: Geophysics, **55**, 1158–1165.

Winkler, K., and A. Nur, 1979, Pore fluids and seismic attenuation in rocks: Geophysical Research Letters, **6**, 1–4.

Winkler, K. W., 1983, Frequency dependent ultrasonic properties of high-porosity sandstones: Journal of Geophysical Research, **88**, 9493–9499.

Witsker, S. O. S., M. Landrø, and P. Avseth, 2014, Using a pseuso-steady-state flow equation and 4d seismic traveltime shifts for estimation of pressure and saturation changes: Geophysics, **79**, M11–M24.

Yilmaz, O., 2001, Seismic data analysis: Processing, inversion and interpretation of seismic data, volume 1 (second edition): SEG.

Zhang, W., Y. Li, T. Xu, H. Cheng, Y. Zheng, and P. Xiong, 2009, Long-term variations of co2 trapped in different mechanisms in deep saline formations: a case study of the songliao basin, china: International Journal of Greenhouse Gas Control, **3**, 161–180.